EXPERIMENTAL INVESTIGATION AND CORRELATION OF LEADING EDGE JET IMPINGEMENT WITH RACETRACK SHAPED JETS FOR GAS TURBINE APPLICATIONS

A Thesis

by

RITWIK VIJAYKUMAR KULKARNI

Submitted to the Graduate and Professional School of
Texas A&M University
in partial fulfillment of the requirements for the degree of

MASTERS OF SCIENCE

Chair of Committee,	Lesley M. Wright
Committee Members,	Je Chin Han
	Yassin A. Hassan
Head of Department,	Andreas A. Polycarpou

August 2021

Major Subject: Mechanical Engineering

ABSTRACT

Heat transfer and discharge coefficients are investigated for leading edge jet impingement using racetrack shaped jets of aspect ratio 2:1. Very few studies discuss heat transfer results for the racetrack shaped jets and less information is available for the pressure losses. The experiment was conducted for varying parametric levels of flow rate (Reynolds number from 10,000 to 100,000), jet-to-jet spacing (s/d = 2 - 8), jet-to-target surface spacing (z/d = 2, 4), surface curvature (D/d = 2.665, 5.33), jet nozzle length (jet plate thickness) (l/d = 1.33 – 4) and fillet radius on the jet orifice (r/l = 0-0.5). For heat transfer, a steady state technique was used to obtain regional heat transfer coefficients, which were reduced to stagnation Nusselt numbers. For discharge coefficients, the total and static pressures were obtained at the supply inlet and jet exit, respectively. The results followed established trends for Reynolds number, jet-to-jet spacing and jet-to-target surface spacing. For jet nozzle length (jet plate thickness), the heat transfer depended on the length of reattachment (based on Reynolds number) due to the vena contracta effect. After a certain length, jet plate thickness becomes irrelevant to either improving heat transfer or improving discharge coefficients, due to higher pressure losses across greater lengths. The addition of fillets helps to improve discharge coefficients at the cost of heat transfer, with minimal difference in the degree of filleting. Existing design correlations were developed over a narrow range of flow parameters for round holes, so their use is limited. To expand the domain, new heat transfer correlations were developed over 95 test cases which provide 10% deviation with 90% confidence. These correlations have been compared with existing literature to further validate their use. Literature does not contain equations for pressure losses and hence, correlations are developed for discharge coefficients, which produce 10% deviation with 88% confidence. These correlations

provide gas turbine blade designers with a convenient tool to quickly and accurately estimate heat transfer and pressure loss for leading edge jet impingement with racetrack shaped jets.

DEDICATION

To my parents for their belief, unconditional love and support over 8000 miles and two years of graduate studies.

ACKNOWLEDGEMENTS

As I complete writing my thesis, words fall short to describe the journey. The years of 2020 and 2021 were filled with highs and lows due to the pandemic, creating a new "normal" in every aspect of life. Initially things seemed bleak as all the plans and preparations for experimentation were pushed away for months. Times were unprecedented and it was necessary for each one of us to adapt to this "new" normal. I couldn't have done it all alone without the tremendous support from each of the stakeholders.

First, I would like to thank my advisor Dr. Wright for guiding me throughout the entire program. Being an international student, it was comforting to find your advisor taking keen interest in ensuring your well-being in academics, research and other aspects of life. I could never have imagined Professor working together in the lab either for finding components, bringing needed materials, making sure the old Scanivalve is working and to every small detail pertaining to the experiments. I admire Dr. Wright's enthusiasm for research and engaging with students to ensure the process becomes smooth. I also appreciate Dr. Wright's importance for maintaining communication through weekly meetings, which helped to take small steps and achieve the goals. I once again thank Dr. Wright for accepting the request to being my advisor at the very beginning of Fall 2019 and providing perceptions whenever I was stuck with days of bad experiments.

I would like to extend my deepest appreciation to Dr. Je Chin Han and Dr. Yassin A. Hassan for serving on my thesis committee. I would also like to thank Professor Michael Golla for being a mentor in my assistantship position and a professional colleague to whom I can reach out to in

tricky situations. The encouragement and support from Professors and staff in the Mechanical Engineering department have been instrumental to make the journey seamless. Studying in Texas A&M University has provided me the opportunity to work with some of the greatest people and have streams of great memories. Finally, I thank all the students in the Turbine Heat Laboratory – Izzet, Izhar, Sulaiman, Luke, Matthew, Hanlin and everyone who have helped directly and indirectly in these two years. Right from selecting the courses, getting familiarized with the lab, navigating compressor key management in pandemic and permitting me to use some of the spare parts for experiments, thank you.

Amongst my peers, I would like to thank Yash Parikh for being a mentor in the journey. Our long discussions and casual meetups helped me to navigate through tough times. It would be injustice if I don't mention the three musketeers who have been my support system in the United States - Haard Naik, Smit Mehta and Pavan Kulkarni. Right from moving in together, exploring the campus and sharing our joys and sorrows, thank you for making these memories cherishing!

Finally, I would like to thank my parents, Vijay Kulkarni and Vaishali Kulkarni for their never-ending support, love and inculcating in the me the values of hard work, resilience and persistence. I could have never imagined not meeting you both for these two pandemic-struck years. I am grateful for having you both in my life and believing in my decisions throughout this journey. To all, thank you.

CONTRIBUTORS AND FUNDING SOURCES

Contributors

This work was supervised by a dissertation committee consisting of Dr. Wright and Dr. Han of the Department of Mechanical Engineering and Dr. Hassan of the Department of Nuclear Engineering.

All other work conducted for the thesis was completed by the student independently.

Funding Sources

Graduate study was supported by a graduate teaching assistantship under Professor Michael Golla in the Mechanical and Manufacturing Engineering Technology Department for the tenures of Spring 2020, Fall 2020 and Spring 2021.

This work was also made possible by two successive scholarships from the American Society of Indian Engineers and Architects (ASIE) in 2019 and 2020.

NOMENCLATURE

a_i	Coefficients in newer correlations
A	Leading coefficient in power equation
A_c	Cross sectional area of the jet (m^2)
$A_{Surface,i}$	Surface area of the i^{th} curved plate (m^2)
Bi	Biot number
d	Jet hydraulic diameter (cm)
D	Target surface curvature diameter (cm)
$D_{orifice}$	Orifice plate diameter (inches)
G	Specific gravity of air
h	Heat transfer coefficient (W/m^2-K)
k	Thermal conductivity (W/m-k)
K	Discharge coefficient (for orifice plate calculations)
l	Jet nozzle length (jet plate thickness) (cm)
L_c	Characteristic length (m)
m	Correlation exponent in power equation
$\dot{m}$	Mass flow rate (kg/s)
N	Total number of jets
$Nu_{stagnation}$	Stagnation Nusselt number
P_1	Absolute upstream static pressure (inches of mercury)
P_{jet}	Perimeter of the jet orifice (m)
ΔP	Pressure drop across orifice plate (inches of mercury)
$\dot{Q}$	Heat transfer (W)

$\dot{Q}_{Input}$	Input power (W)
$\dot{Q}_{High}$	Input power in the high-temperature test (W)
$\dot{Q}_{Loss}$	Actual heat loss for the experiment condition (W)
$\dot{Q}_{Low}$	Input power in the low-temperature test (W)
$\dot{Q}_{Net,i}$	Net power input after accounting heat loss for i^{th} plate (W)
r	Radius of fillet at orifice edge (cm)
Re	Reynolds number
s	Jet-to-jet distance (cm)
T_1	Inlet temperature at the orifice (°R)
T_c	Coolant temperature (K)
$T_{Center\ jet}$	Temperature of the center jet (K)
T_{film}	Film temperature (K)
T_{High}	Wall temperature for the high-temperature test (K)
T_{Low}	Wall temperature in the low-temperature test (K)
T_{Room}	Room temperature for the experiment condition (K)
$T_{Room,Low}$	Room temperature in the low-temperature test (K)
$T_{Room,High}$	Room temperature in the high-temperature test
T_w	Wall temperature (K)
v_{jet}, V_{jet}	Jet velocity (m/s)
V_{ideal}	Ideal jet velocity (m/s)
y	Compressibility factor
z	Jet-to-target surface distance (cm)

β	Ratio of jet diameter to diameter of the supply pipe
μ	Dynamic viscosity (kg/m-s)
ρ	Density of air (kg/m^3)

TABLE OF CONTENTS

LIST OF FIGURES

LIST OF TABLES

CHAPTER I

INTRODUCTION

Jet Impingement is a phenomenon where a stream of fluid strikes a surface, which promotes heat transfer between the fluid and surface. Due to its aggressive nature and immense potential to remove heat load, it lends itself as a cooling technique in gas turbine industries, aircraft propulsion systems, high dense electronic chip systems, annealing of metals, textile and paper drying, and aircraft wing deicing. In the recent 15 years, it has gained application in the automotive industries to cool high power battery systems in electric vehicles. With the extensive applications, it is essential to become familiarized with the fundamentals of jet impingement.

A jet can be characterized by high velocity fluid ejecting from a hole into a surrounding medium. The types of jets are free flow jet, isothermal jets, non-isothermal jets and impinging jets. Free jets can be defined as a pressure driven unrestricted flow of a fluid into a quiescent ambience, where the wall ceiling or obstruction does not influence the jet. As the jet exits the orifice, there is gradual entrainment of ambient fluid into the jet stream. This is due to the difference in the jet pressures across the boundaries, driving the phenomenon and forming shear layers across the boundaries [1]. As a result, the area averaged velocity across the jet decreases. This region where some portion of the exit axial velocity remain preserved, is called the potential core, which is observed four to six diameters from the exit [2]. The flow profile beyond this region can be characterized by mixing of the ambient fluid with the jet stream and flow instabilities. It is similar to the developing region in turbulent flows and is observed six to twenty diameters from the exit. With the development of a boundary amidst the instabilities, the flow profile stabilizes and

becomes independent of the downstream distance, thus becoming a developed flow. The zones and characteristics are listed in table 1.1 and the flow profiles can be observed in figure 1.1.

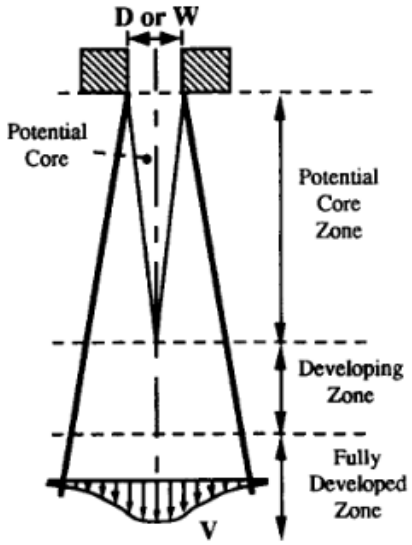

Figure 1.1: Flow profile of a free jet (Reprinted from [2])

Table 1.1: Characteristics of different zones of free jet (Adapted from [2])

Name of region	**Zone (in terms of z/d)**	**Characteristics**
Potential Core	4 to 6	Centerline velocity equal to nozzle outlet velocity
Developing	6 to 20	Centerline velocity decays and interaction region between shear layers from both sides merge
Developed	After 20	Transverse velocity profiles are similar at different values of z/d

With jet impingement, a coolant jet impinges on a heated surface (or vice versa). A jet impinging on a flat plate is divided into three regions: the free jet region, the stagnation, or impinging region, and the wall jet region. The flow profile is presented in figure 1.2. The free jet region is the zone where the effects of the stagnation region are felt and is similar to the unconfined free jets. Beltaos et al. [3, 4] noticed that the potential core of the impinging jet is less than four diameters. With the increasing distance, there is a growing effect of pressure difference between

the jet and ambient fluid, leading to a development of shear layer across the boundary. This permits entrainment of ambient fluid and increases the radial spread of the jet. The mixing effect propagates with distance and vortices formation take place due to Kelvin Helmholtz instabilities [1, 5].

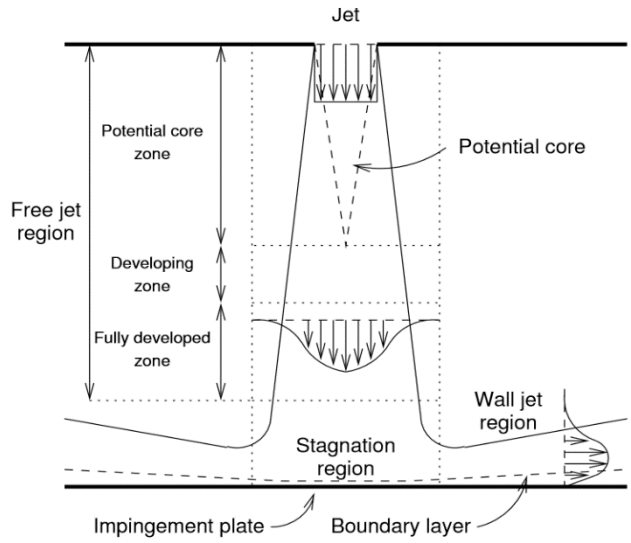

Figure 1.2: Flow profile of an impinging jet (Reprinted from [6])

The jet impinges on the flat plate and the region is identified as the stagnation region. At this point the static pressure is higher than the ambient pressure, resulting in a favorable pressure gradient that turns the flow to a direction parallel to the target surface, forming the wall jet region. The jet adheres to the surface as it flows over the plate [7]. Due to the sudden acceleration and change in flow direction, there are very thin boundary layers – both hydrodynamic and thermal - present in this region. This leads to very high heat transfer and skin friction. Based on the non-dimensional distance of the jet from the target surface, the heat transfer trends can be slightly different. If the distance is greater than the potential core length, the Nusselt number (nondimensional heat transfer parameter) has a peak and a Gaussian-shape bell curve.

However, for the distance smaller than the potential core, there are two peaks observed – one due to the impingement and the second due to the transition of flow from laminar to turbulent. This can be observed in the plots presented in figure 1.3, where the creation of secondary peaks can be seen as the jet-to-target surface spacing decreases.

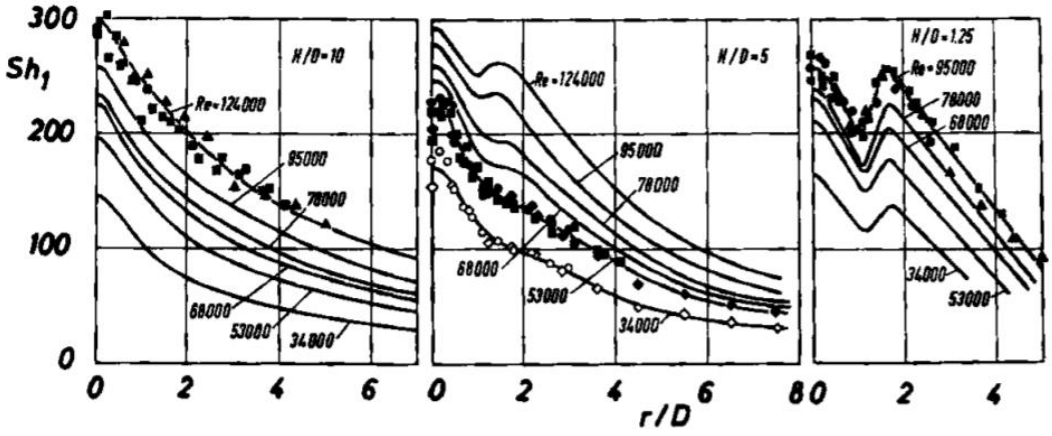

Figure 1.3: Variation of Sherwood number with distance from impingement location with different jet Reynolds number for (a) (left) z/d = 10 (b) (center) z/d = 5 and (c) (right) z/d = 1.25 (Reprinted from [8])

With the increasing distance in the wall jet region, the velocity decreases and the thermal boundary layer thickens, which leads to decreasing heat transfer. Due to the smaller areas with enhanced heat transfer, multiple jets are employed to extend the capability across the system. Based on the jet-to-jet distance, the mixing and interaction leads to regions of peaks and valleys [9]. However, accumulation of the air inside the impingement chamber affects the heat transfer trends, necessitating the need to remove the spent air efficiently. Having developed a clear understanding of the jet impingement phenomenon, the next section discusses its application for the gas turbine blade cooling.

Gas Turbines Cooling Technology

Gas turbines play an essential role in the industrial world – with applications to land-based power generation and aircraft propulsion. Also, some versions of gas turbines exist on naval ships, helicopters and are often coupled with a generator for industrial, academic and residential necessities. This prime mover has been ubiquitously deployed due its relatively high efficiency. It operates on a Brayton Cycle and consists of three major components – compressor, combustor and turbine. A simple diagram is shown in the figure 1.4.

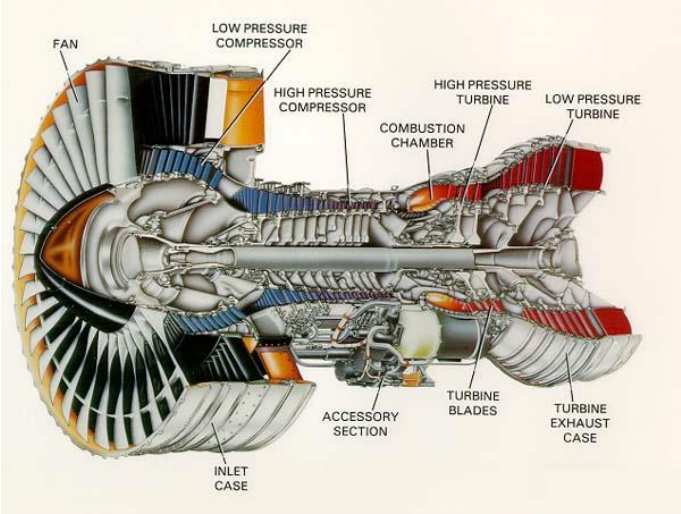

Figure 1.4: Cutaway of Gas Turbine Engine (Reprinted from [10])

The inlet air passes through the compressor, which increases the pressure and subsequently the temperature. This high-enthalpy air ignites the fuel in the combustor, causing it to expand rapidly. This air exits the combustor and impinges on the turbine stator and rotor stages, where the kinetic energy is extracted. This happens to a greater extent for power-generation, while for the propulsion, some of the energy is left for necessary thrust. From the empirical studies and thermodynamic calculations, the gas turbine power output and efficiency improve with the increase in the turbine rotor inlet temperature (RIT). Figure 1.5 presents the increasing power

capacity with the inlet temperatures. The figure also conveys the feasible metal temperature range and extended range with the help of cooling, where advanced gas turbines operate at high temperatures (1370 – 1430 C). This often exceeds the blade melting temperatures and can cause thermal wear. The thermal loads on a stator vane and rotor vane are described in figure 1.6.

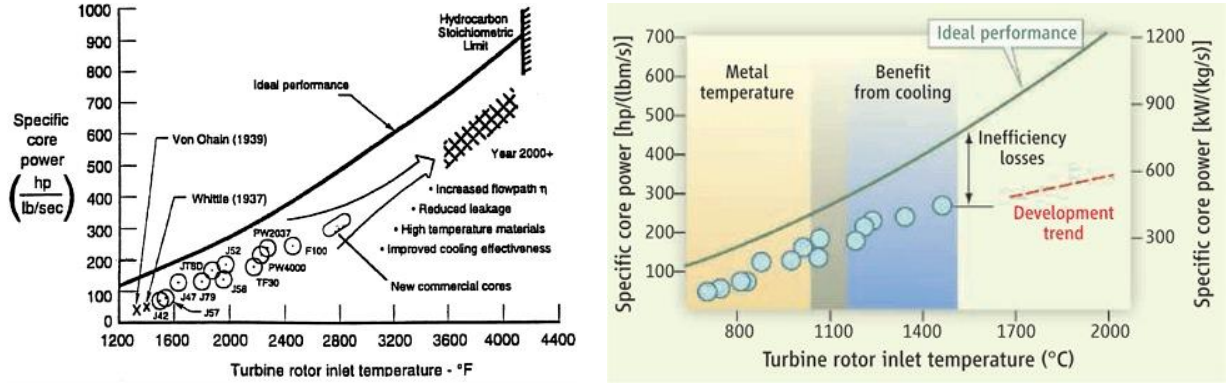

Figure 1.5: (a) (left) Cycle power improvement with increasing turbine inlet temperature (Reprinted from [11]) (right) Feasible metal temperature and extended range due to cooling (Reprinted from [12])

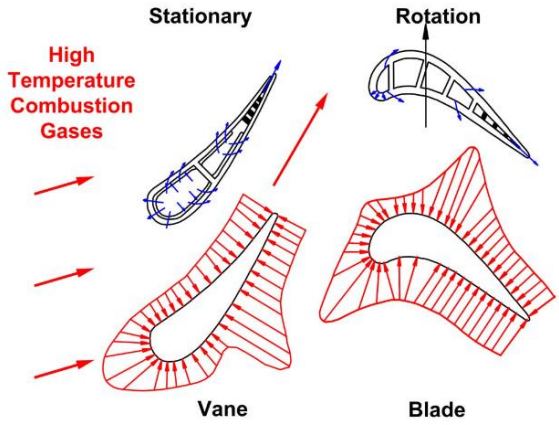

Figure 1.6: Schematic of gas turbine thermal loads (Reprinted from [13])

To maintain the high efficiency and achieve reasonable durability goals, cooling techniques have been employed to keep the blade temperatures in check. The cooling is carried out by extracting the air from the compressor, thereby imposing a limitation to the thermal efficiency of the process. To balance the trade-off, it is essential to have optimized cooling techniques and efficient coolant distribution. Gas turbine vanes (stator) and blades (rotor) are cooled externally and internally using the extracted air. A schematic of the present cooling techniques is shown in figure 1.7. The coolant passes through various serpentine channels to cool the blade internally and is ejected out to protect the blade externally from the mainstream gas. The air forms a blanket to shield from the hot combustion gas, which is called film cooling. Cooling reduces the temperature difference between the surface and the adjacent fluid which reduces the heat transfer. Another mode of protection involves using the thermal barrier coating (TBC) which increases the thermal resistance to reduce overall heat transfer.

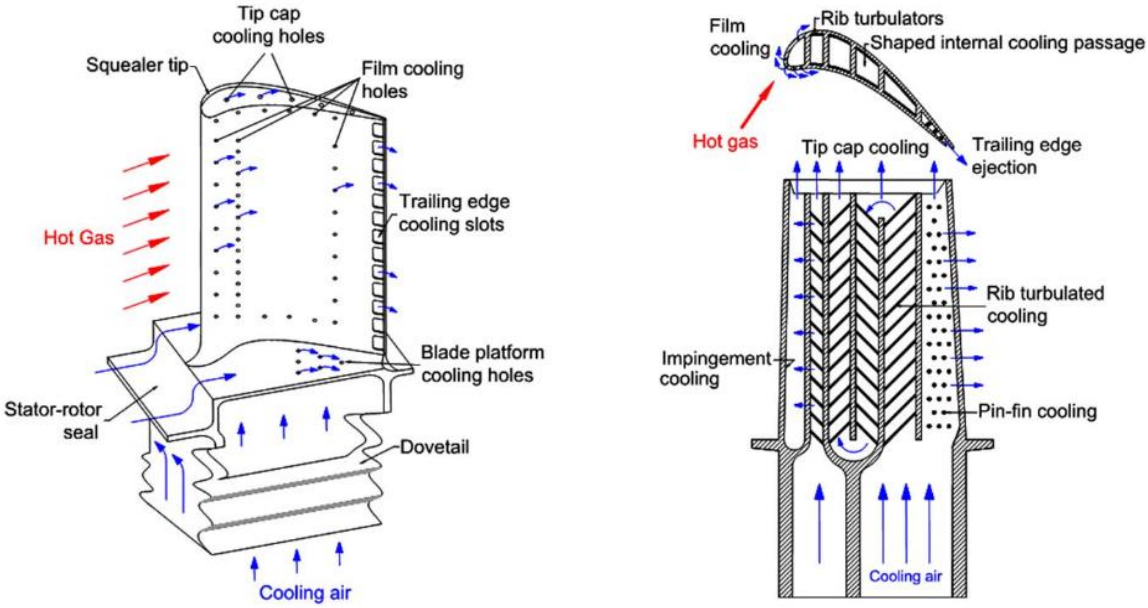

Figure 1.7: (left) External cooling (right) Internal cooling (Reprinted from [13])

The internal cooling techniques are localized for specific blade regions based on the nature and intensity of heat load. At the trailing edge, pin-fins are used as they increase the area of dissipation and increase the turbulent mixing to enhance heat transfer. Given the material constraint and concentrated hotspots, it is an effective mode of cooling. At the midchord section, rib turbulators and dimples are present. They help to trip the boundary layer in spaced intervals, which help to maintain thin boundary layers and high heat transfer. In stators, the midchord section uses jet impingement for cooling. At the leading edge, heat loads are present in great intensity and present over a larger area (shown in figure 1.6). Hence, jet impingement is deployed as it is an aggressive form of cooling. Coolant air is supplied from the impingement chamber, where it passes through orifices and impinges on the surface. After impingement, the coolant either exits through the film cooling holes (rotor) or from crossflows to other sections of the blade. A fraction of total air from the compressor is supplied as coolant, where excess use of coolant reduces the efficiency, and insufficiency leads to reduction in turbine blade life. Thus, there is a need to effectively utilize the coolant distribution amongst all techniques.

Problem Statement

Industries face a persisting problem of efficient coolant distribution and require accurate estimates to ensure the heat transfer design model is robust. The data is gathered from a vast majority of literature that have completed heat transfer and pressure loss estimation experiments for various jet geometries, configurations and flow conditions. However, the data is often sparse, deviating from realistic scenarios, and limited in experimentation capacity. Moreover, industries deploy complex jet geometries and run at higher flow parameters, while the greater part of literature is based on round jets and limited research of complex geometries at higher Reynolds numbers. Besides, the current jet geometries are not representative of the conditions present in modern turbine blade design. Due to initial manufacturing limitations and with usage, the jet edges often have fillets present and this affects the heat transfer and pressure losses across the system. Studies have been carried out to investigate the effects at lower flow parameters and require extension to higher flow rates. Moreover, there are no discharge coefficient correlations in literatures for racetrack jets, which are essential to estimate the coolant pressure head needed for internal and external cooling. Understanding the pressure loss behavior and quantifying their trends would help to further aid the heat transfer investigations.

Aims and Objectives

The outcome of this research aims to produce heat transfer and discharge coefficient correlation for varying jet geometries and flow conditions for racetrack shaped impingement jets. With some of the test parameters resembling industrial operating conditions, this correlation aims to assist the designers for estimation of heat transfer across the leading-edge region of the gas turbine blade. Employing the correlation helps to save time over searching various sources to obtain credible data, benchmarked over previous literature. Also, the thesis aims to study the effects of jet edge conditions on the heat transfer trends at higher Reynolds numbers, which is closer to the realistic scenario for gas turbine impingement. In addition, the study also investigates the heat transfer and discharge coefficient trends for jet-to-jet spacings, jet-to-target surface spacings, jet plate thickness and curvature effects.

CHAPTER II

LITERATURE REVIEW

Modern cooling technologies are continuously evolving, with efficient modes of heat extraction being developed, and it is essential for the engine designers to remain updated with current research in the gas turbine community. Han et al. [14] provides a comprehensive view of the heat removal techniques in the external and internal regions of gas turbine blades. Various cooling strategies are deployed for different sections of the blade, with each of them adapted to the existing realities of the region. For this study, the focus is on the leading edge section of the turbine blade, which faces a tremendous heat load, as discussed in the previous section. Due to the requirement of managing high heat loads, the jet array impingement technique is used. Ekkad et al. [15] present a review of the contemporary developments in the jet impingement, with effects of materials, jet shapes, target wall roughness, nozzle contouring, and impingement channel modifications on cooling performance. Researchers model the leading edge section as curved surface impingement. Due to the complexity in heat transfer and pressure loss trends for curved surface impingement, it is convenient to first understand them in flat plate impingement and further develop them. To understand the trends, each parameter is addressed individually: flow rate (Re), jet-to-jet spacing (s/d), jet-to-target surface spacing (z/d), curvature-to-jet size (D/d), jet nozzle length (l/d) (jet plate thickness) and jet edge condition (r/l). Detailed studies of individual parametric effects on heat transfer and pressure loss are included.

Flat Plate Impingement

Flat plate impingement is approximated for areas where the surface curvature is very large. In gas turbines, hot gases exiting the combustion chamber encounter the nozzle guide vane (NGV) and imparts a tremendous heat load across the entire blade (schematic in figure 1.6). Typically, two cooling techniques are used – jet impingement across the midchord region and pin-fin cooling at the trailing edge. The arrangement is presented in figure 2.1. The midchord is a region with large surface curvature and is treated as a flat surface for impingement studies.

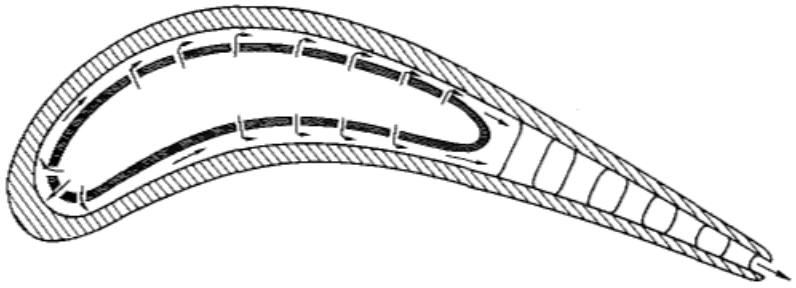

Figure 2.1: Impingement arrangement in a nozzle guide vane (NGV) (Reprinted from [16])

Due to the vast expanse of area in the midchord, multiple jet rows are present to maintain the average heat transfer across the surface. The rows can be arranged in two forms – inline and staggered configurations (presented in figure 2.2).

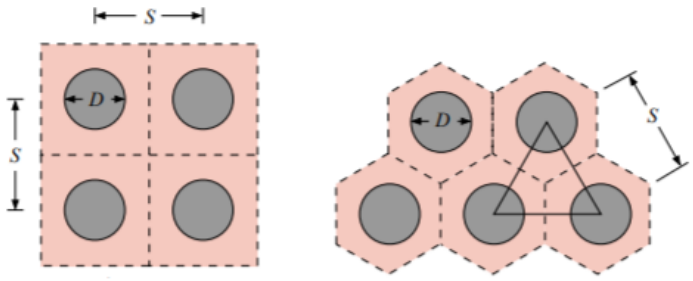

Figure 2.2: Jet array configurations: Inline (left) and Staggered (right) (Reprinted from [17])

The inline arrangement resembles an ordered structure with the same spacing in the streamwise and spanwise directions. The staggered arrangement looks like a honeycomb structure with one row of jets stacked in the empty spaces of the other row at a certain distance. Each arrangement presents its contribution to heat transfer differently in terms of peak Nusselt number, average Nusselt number, and ability to overcome crossflow effects (discussed later in this section). The Nusselt number trends for multiple row impingement depend on flow parameters like jet Reynolds number and geometric parameters like jet-to-jet spacing, jet-to-target surface spacing, and crossflow. Due to varying experimental setups, results are often presented in the non-dimensional form. The Nusselt number is a non-dimensional parameter for heat transfer, Reynolds number being for flow parameter. For geometric parameters, the length value is typically normalized with the jet hydraulic diameter.

Detailed analyses have been carried out and presented in literature [18-20]. The Nusselt number generally increases with the increase in jet Reynolds number, attributed to more significant turbulence in the flows. In multiple jet impingement, the streamwise heat transfer distribution yields cyclic patterns of peaks and valleys. The peaks are primarily due to the presence of jets and the valleys appear between the jets. Concerning the jet-to-target surface spacing, for the inline arrangement, the Nusselt number increases as the distance decreases up to 6 diameters, which is

where the potential core begins. Brevet et al. [18] identified that the Nusselt number increases with decreasing z/d from 10 to 3 and decreases beyond z/d = 3.

For the jet-to-jet spacing in the inline arrangement, the average Nusselt number increases with decreasing distance. From Brevet et al. [18], the average Nusselt number increases as the spacing decreases from 10 to 2. Reducing the distance ensures equal heat transfer across larger areas but does not necessarily increase the peak Nusselt numbers. Huang et al. [20] presented the results for varying jet-to-jet spacing for staggered rows. Interestingly, the Nusselt number increases with increasing spacing from 4 to 8. With the fountain effect and jet interactions in s/d = 4, there is a second peak at one diameter from the jet location in the streamwise direction. However, this is not present for s/d = 8 due to the ease of spent air removal. In addition, the heat transfer increases until s/d = 12 and decreases further.

In systems with multiple jet rows, it is often found that the spent air in the impingement chamber flows perpendicular to the jet flow, which is called crossflow. With the accumulation of spent air downstream of jets, the air deflects the jet direction, thus reducing the heat transfer. The crossflow effect can be dominant and affect the heat transfer performance based on the jet configuration, the number of jets, and jet-to-jet spacing. Figure 2.3 depicts the jet deflection from the crossflow of spent air. Several methods have been presented to reduce this effect, with the one involving extraction of spent air to film cooling and showerheads on the outside of the blade. These help to reduce the intensity of crossflow and minimize jet deflection. Another strategy is to change the jet impingement angle to counter the jet deflection (Huang et al. [21]).

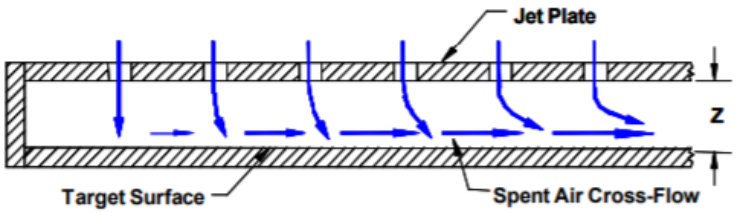

Figure 2.3: Jet deflection due to crossflow (Reprinted from [22])

Curved Surface Impingement

The leading edge of the gas turbine blade has a relatively small radius of curvature and the studies of curved surface differ from the flat plate. Having understood the heat transfer trends with parametric variation on a flat plate, the studies on the curved surface provide a realistic view of the heat transfer variations in the leading edge. In addition, the leading edge typically employs a single row of jets and the crossflow effect is minimum. Studies of Chupp et al. [23] pioneered the parametric correlation development of heat transfer trends in leading edge jet impingement. The correlation presented dependence of Nusselt number on flow parameters like jet Reynolds number and geometric parameters like jet-to-jet spacing (s/d), jet-to-target surface spacing (z/d), and curvature-to-jet size (D/d). Steady state heat transfer experiments were carried out over a single row of circular jets impinging on the half-cylinder surface, and regional Nusselt numbers were obtained with the help of platinum heater strips. A schematic of the impingement setup is presented in figure 2.4.

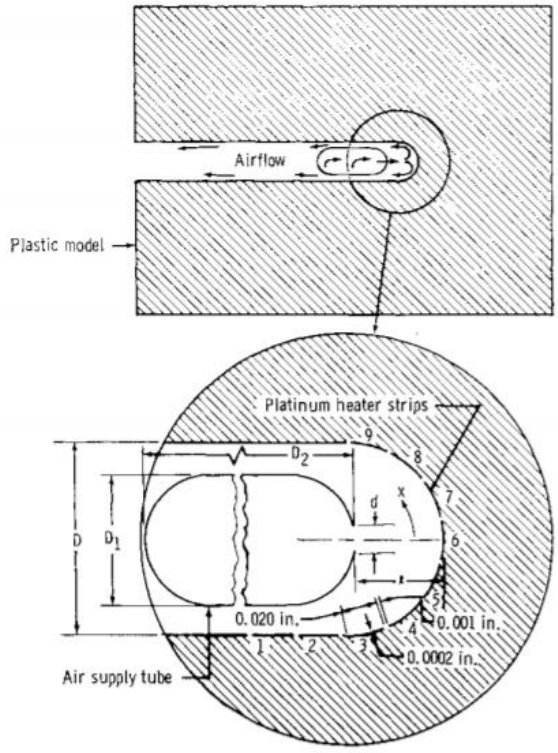

Figure 2.4: Schematic of leading edge impingement setup used by Chupp et al. [23]

(Reprinted from [23])

The correlation presented by Chupp conveys the increase in Nusselt number with increasing jet Reynolds number, decreasing jet-to-jet spacing, and increasing curvature-to-jet size. Moreover, Chupp et al. [23] used round, square edged, jets for leading edge impingement. The heat transfer correlations were presented over the stagnation region (equation 2.1) and averaged over the surface (equation 2.2). Due to the accuracy of correlations by Chupp et al. [23], industries utilize them for heat transfer estimation across the leading edge. The experiments were carried out the following ranges of parameters:

$3000 \leq Re_{jet} \leq 15000$, $4 \leq s/d \leq 16$, $1 \leq z/d \leq 10$ and $1.5 \leq D/d \leq 16$.

$$Nu_{Stagnation} = 0.44 \cdot Re^{0.7} \cdot \left(\frac{d}{s}\right)^{0.8} \cdot \exp\left[-0.85 \cdot \left(\frac{z}{d}\right) \cdot \left(\frac{d}{s}\right) \cdot \left(\frac{d}{D}\right)^{0.4}\right] \quad \textbf{(2.1)}$$

$$Nu_{Average} = 0.63 \cdot Re^{0.7} \cdot \left(\frac{d}{s}\right)^{0.5} \cdot \left(\frac{d}{D}\right)^{0.6} \cdot \exp\left[-1.27 \cdot \left(\frac{z}{d}\right) \cdot \left(\frac{d}{s}\right)^{0.5} \cdot \left(\frac{d}{D}\right)^{1.2}\right] \quad \textbf{(2.2)}$$

A comprehensive study of leading edge jet impingement was carried out by Metzger et al. [24] and explored the possibilities of varying parameters to improve heat transfer. The following section presents the effects of parameters individually on the leading-edge impingement heat transfer.

Jet Reynolds Number

From traditional heat transfer literature, it is a well-established fact that heat transfer increases with Reynolds number. The behavior is expressed mathematically as the Nusselt number being equal to the Reynolds number raised to a power. From Jordan et al. [25-27], the power is usually 0.7 to 0.8 for turbulent jets and 0.5 for laminar jets. From Chupp et al. [23], the jets are turbulent as the power is 0.7. The value of 0.7-0.8 is present across correlations for the single jet (Lee et al. [28], Gori et al. [29]), a single row of jets (Bond et al. [30]), or multiple rows of jets (Florschuetz et al. [16]). Despite being widely accepted, the power is sometimes conflicting. For oblique jet impingement in the internal surface of a wing leading edge, the power goes to 1.1 (Yu et al. [31], Bu et al. [32]). For flat plate jet impingement on a dimpled surface, the power is 0.6 for the dimpled surface and 0.5 for smooth surface (Kanokjaruvijit et al. [33]). Hrycak et al. [34] addressed the issue for power reducing to 0.63 for 2< z/d< 8. It is attributed to

the less space for the air entrainment in mixing and developing of the wall jet. Metzger et al. [24] carried out studies of laminar jet impingement and reported the effect of Reynolds number to be most pronounced at higher values of z/d, due to rapid decay of the Nusselt number at larger spacings. This study suggests dependence of z/d on the power. Multiple jet impingement correlations from Chang et al. [35] also included the z/d parameter in the power of the Reynolds number. One potential reason for the dependence on z/d is the potential core in the impingement zone. Due to the laminar and inviscid nature of the potential core, if present at the stagnation region, it can yield a power of 0.5. If the potential core has decayed before reaching the plate, the jet becomes turbulent, yielding a power of 0.7-0.8.

Jet-to-Target Surface Spacing (z/d)

The heat transfer trends for the varying jet-to-target surface spacing (z/d) are conflicting in terms of the optimum distance for the maximum Nusselt number. From the correlations of Chupp et al. [23], it is clear that the Nusselt number increases with decreasing spacing. Although it is true for most of the range, the findings seem to be different when the potential core is present. For laminar and near-turbulent jets, Metzger et al. [24] and Fenot et al. [36] reported the optimum values of z/d are in the range of 3-5, which is the onset of potential core. CFD studies of Forster et al. [37] also confirm the increase in heat transfer by reducing spacing from 4 to 2.7. However, Lee et al. [28] showed that the optimum heat transfer lay just at the end of the potential core. Bu et al. [32] concluded that the effect of z/d on heat transfer depended on the flow nature of the jet. For higher Reynolds number jets, the central axial velocity played a crucial role, where smaller distance seemed appropriate. For lower Reynolds number jets, the jet turbulence played a

dominant role in increasing heat transfer, thereby needing sufficient distance to allow shear layer entrainment into the potential core.

Jet-to-Jet Spacing (s/d)

The effect of jet-to-jet spacing on the Nusselt number is generally considered to be inversely proportional. Chupp et al. [23] and Fenot et al. [36] agree that the Nusselt number increases with decreasing s/d. With decreasing spacing, there is a greater mixing between the shear layers of the jets, increasing the turbulence and leading to thin boundary layers. In addition, there are a greater number of jets impinging in the area, thereby having more Nusselt number peaks, but the magnitude of the peaks may not increase.

After impingement, there is a need to remove the spent air from the impingement cavity, otherwise creating jet deflection. There are two effects present in the cavity – mixing between the jet boundary layers that lead to increased heat transfer, and greater chances for spent air to deflect neighboring jets and reduce peak Nusselt numbers. Tabakoff et al. [38] found that decreasing s/d led to degradation of heat transfer at z/d = 1. It can be attributed to limited space for spent air removal with decreasing s/d. This trend was confirmed with the results of Metzger et al. [24]. Martin et al. [39] presented an interesting trend where heat transfer increased from s/d = 8 to 4 and decreased in s/d = 2 for z/d = 8. However, for smaller z/d (= 2), the heat transfer increases with s/d. Facchini et al. [40] experimented with a double row of jets and found that despite an increase in s/d, heat transfer increased at smaller z/d (=4.53). It could be due to greater mixing between the jets and a small tolerable space for spent air removal.

From the results, it is evident that the removal of spent air is necessary. In order to tackle the problem, modern gas turbine blades have extraction holes in place. In essence, the extraction holes are connected to the impingement cavity, such that air after impingement exits through the system. The spent air is used for film cooling in the leading edge section, where the spent air forms a blanket around the external area to prevent direct contact of hot gases with the blade.

Target Surface Curvature-to-Jet Size (D/d)

As moving from a flat surface to a curved surface changes some dynamics of heat transfer, studies explore the possibility of changing curvature-to-jet size ratio to improve performance. Bunker et al. [41] carried out heat transfer tests for different nose radii of the leading edge (schematic presented in figure 2.5). From their results, the larger the radius, the higher the heat transfer coefficients. In addition, the Nusselt number range is vast; therefore additional thermal stress is induced. As the radius decreases and the nose becomes sharper, the heat transfer reduces and becomes uniform across the surface, leading to secondary peaks. However, each of the results had increasing jet-to-target spacing, which also reduces heat transfer. Thus, the effect of standalone surface curvature could not be established.

From the studies of Chupp et al. [23], the heat transfer increases with the surface curvature. It could be due to the increased space for removing the spent air and less opportunity for spent air to affect the impinging jet. These conclusions seem to match with the results of Fenot et al. [36] and Hrycak et al. [34]. The decrease in heat transfer for a sharper nose is attributed to the pockets of coolant near the nose, preventing the jets from stagnating at the nose. Martin et al. [42] computationally investigated the effect of curvature and found that as the curvature-to-jet size

(D/d) decreases, the area with the peak Nusselt number decreases and produces a more uniform spread. From the results of Patil et al. [43], the normalized heat transfer coefficient varies proportionally with the curvature-to-jet size. Based on the studies, it becomes seemingly apparent that the heat transfer increases with increase in surface curvature and leads to higher gradients in the heat transfer distribution.

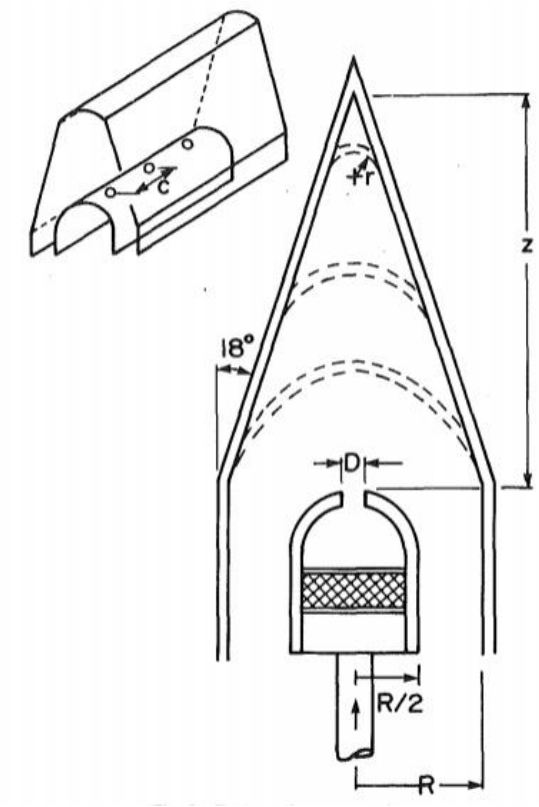

Figure 2.5: Schematic of test setup used by Bunker et al. [41] (Reprinted from [41])

Jet Nozzle Length (l/d) (Jet Plate Thickness)

The jet nozzle length is the length of the jet travels before exiting the orifice, also called jet plate thickness. As the fluid enters the orifice, a flow area reduction causes flow separation. Due to the separation and recirculation along the sides, there is a restricted flow area near the inlet of the orifice. This reduced area increases the jet velocity at the orifice exit for shorter jets. This phenomenon is called the vena contracta effect. It is due to this effect, shorter jets have high heat transfer. However for thicker jet plates, there is sufficient length for the flow to reattach and recover and thus provide a developed flow at the orifice exit. A schematic of the effect is presented in figure 2.6. Harmon et al. [44, 45] concluded that the decrease in jet length improved the stagnation Nusselt number. It is due to the effect of the vena contracta accelerating the flow near the exit for shorter jets. For thicker jet plates, the flow development reduces the local acceleration of the jet. However, Patil et al. [43] presented correlations where jet length ratio (l/d) has different powers for different jet-to-target surface spacings (z/d). For the closer spacings ($0.67 < z/d < 2$), the average Nusselt numbers decreased with jet length ratio, and for larger spacings ($2 < z/d < 8$), the averaged Nusselt numbers increases with jet length ratio. Due to the conflicting results, there is a need to investigate the effect of jet nozzle length (jet plate thickness) on the heat transfer.

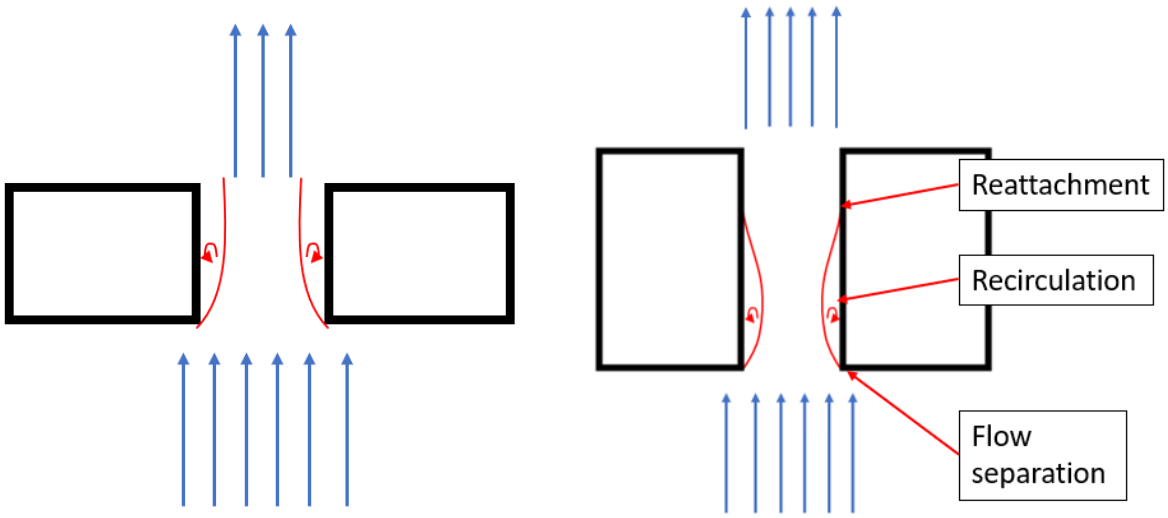

Figure 2.6: Schematic of the vena contracta effect – (left) Increased velocity in shorter jets (right) Flow development in longer jets

Jet Shape

The previous studies presented the heat transfer trends based on discrete jet impingement. Due to the large differences between peaks and valleys in discrete cooling and higher temperature gradients, the average Nusselt number can be relatively low having high peak values. Hence, a more continuous heat transfer distribution was necessary and it gave rise to slot jet impingement. Despite their benefits, slot jets come at the cost of the blade's structural integrity. Both Bunker et al. [41] and Tabakoff et al. [38] showed results of degrading heat transfer for slot jets. In addition, Tabakoff et al. [38] presented a more uniform heat transfer distribution across non-stagnation regions for slot jets over discrete jets. The authors attribute it to the advantage of three-dimensional mixing in discrete jets over two-dimensional mixing in slot jets. In order to match the discrete jets, the slot jets needed more coolant, which could reduce the efficiency of the

coolant distribution system. Several studies confirm this trend (Gau et al. [46], Yang et al. [47] and Choi et al. [48]). Amongst the slot jets, the most narrow slot yielded the highest heat transfer.

Another variation in the jet shape includes using a nozzle, which helps to increase to jet velocity and improve heat transfer. Colucci et al. [49] showed higher heat transfer for a contoured nozzle over an orifice nozzle for smaller jet-to-target spacings. Guan et al. [50, 51] experimented with a chevron shaped nozzle on a conical concave surface. Although the results were presented as heating efficiency, the heat transfer is higher than the conventional nozzle. The studies mentioned have been carried out for single axisymmetric jets. With novel shape designs such as loped jets, synthetic jets, exited jets, and extended jets in literature, the experiments were completed primarily over the flat plate and either single jets or multiple rows of jets. Yang et al. [47] carried out tests with round, rectangular and contoured nozzles. The increase in Nusselt number due to changing jet to nozzle spacing is more significant in rectangular jets than the rest. The authors attribute it to the early development of rectangular jets and a sharp increase in turbulence intensity. For larger jet-to-target surface spacings, round jets outweigh the rest in heat transfer for a range of jet-to-jet spacings from 0-18. For smaller spacings ($z/d = 4$), the rectangular jets provide higher heat transfer upto $s/d = 6$, while round jets dominate beyond $s/d = 6$.

Researchers were looking for potential designs to combine the advantages of obtaining uniform heat transfer in slot jets and the higher peak Nusselt number in discrete jets. One possibility was to expand the round shape to an elliptical shape. Lee et al. [52] experimented with the nozzle aspect ratio for elliptical shaped jets for flat plate impingement. They found an increased turbulence intensity at the jet exit and found increases in heat transfer. In addition, the heat transfer depended on the aspect ratio and jet-to-target surface spacing. With the promising results from elliptical shaped jets, an improved design, called "racetrack" shaped jets was

introduced. Singh et al. [53] tested the racetrack, V-shaped, and round jets in flat plate impingement with maximum crossflow and found that the V-shaped jets performed best. For curved surface impingement, Taslim et al. [54-56] experimented with the racetrack jets over round jets, racetrack jets with a roughened leading edge, and racetrack jets with crossflow. They concluded the racetrack jets outperformed the round jets. Keeping the Reynolds number fixed between racetrack and round jets, the racetracks required more mass flow rate due to greater cross-sectional area. Jordan et al. [25-27] and Harmon et al. [44, 45] too experimented with the racetrack shaped jets to find better heat transfer and more coverage of peak Nusselt numbers.

Jet Orifice Edge Condition

The majority of the previous literature focused on improving the cooling performance, and much work has been carried out over the jet orifice edge conditions. Typically, studies have been using the default square-edged orifice at the inlet and outlet. The square edge produces higher turbulence intensity at the jet exits, providing enhanced heat transfer. The vena contracta effect (discussed in the "Jet Nozzle Length (Jet Plate Thickness) " section) occurs due to the sudden reduction in flow area caused by the square edges. It causes flow detachment, accelerates the flow, and imparts high velocity to the jet at the exit. Thus, it helps to improve heat transfer. Although promising, the realistic scenario for cast holes prevent the orifices from having perfectly square corners. It can be due to manufacturing limitations, material protrusions, and repeated usage that lends them some degree of rounding at the edges. In addition, the vena contracta effect brings more significant pressure losses due to the flow acceleration. Filleting the inlet and outlet provides

a gradual change in the cross-sectional area and helps to reduce the pressure drop—a conceptual view of a square edge and rounded orifice are shown in figure 2.7.

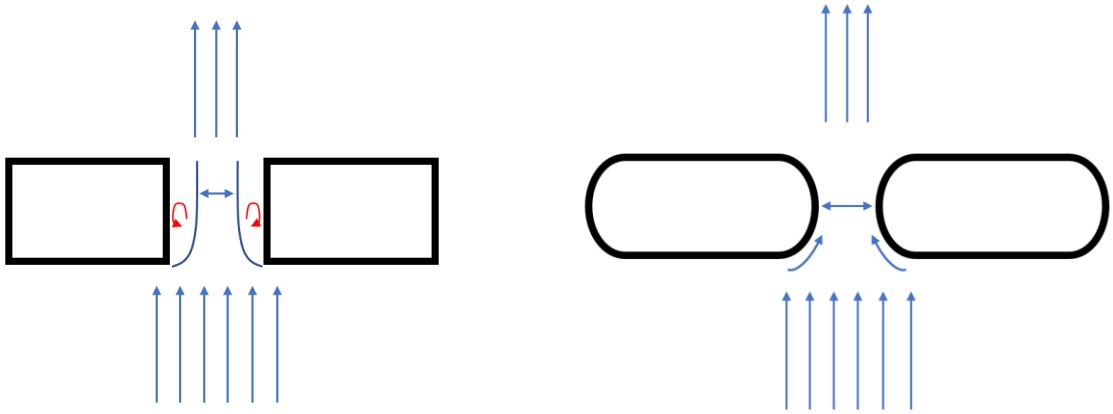

Figure 2.7: Schematic of the vena contracta effect in square-edged (left) and filleted (right) jets. There is a reduced flow area in square-edged jets

Lee et al. [57] carried out tests over the sharp-edged orifice, standard-edged orifice, and square-edged orifice for confined jets and found the sharp-edged to have the highest heat transfer amongst the rest. Brignoni et al. [58] experimented with the inlet chamfering and found that pressure drop decreases without a significant change in the heat transfer coefficient. The performance parameter, which is equal to the heat transfer coefficient divided by the pressure drop, was 30.8% higher than the unchamfered jets. The experiment was carried out for a single round impinging jet over a flat plate. Although not specific for jet impingement, the results from Hay et al. [59] and Dittman et al. [60] too confirm the reduction of pressure drops due to chamfering.

Jordan et al. [25-27] carried out transient liquid crystal (TLC) tests for the effect of jet edge filleting at the inlet and outlet for racetrack-shaped jets. The pressure drop results were presented in terms of discharge coefficients, and higher discharge coefficient values meant lesser pressure

drops. They found discharge coefficients to be higher for filleted jets, but this came at the cost of reduced heat transfer. Harmon et al. [44, 45] used the steady-state heat transfer technique and found the same results. The radial bypass tests conveyed that the filleted jets are more susceptible to axial velocity degradation due to a lack of straight channel to support axial development.

Other Impingement Considerations

In addition to previous studies of varying flow parameters and geometric properties, other factors are explored to understand their effect on heat transfer performance. One is the effect of crossflow on the heat transfer distribution. Previous literature has ensured uniform distribution of flow across the jets; however, there are times where some air is bled from the impingement channel for tip cap cooling. It is modeled as radial bypass flow, and Jordan et al. [25-27] have experimented with various inlet conditions. They have found that large intensities of crossflow can significantly reduce the heat transfer as the amount of supply air can deflect the jets. Harmon et al. [44, 45] varied the inlet and exit filleting radius in crossflow experiments. They found that the square-edged jets counter the crossflow, leading to a minimal reduction in heat transfer. However, the filleted orifices support the deflection of the jet due to the lack of a straight channel to allow jet redirection. Therefore, it leads to degradation of heat transfer in filleted holes with crossflow.

Another group of studies focused on the inlet jet temperatures. Fenot et al. [36] created a significant temperature differential and found no difference in heat transfer. Martin et al. [42] used actual engine data for jet temperatures and found little impact of varying inlet jet temperatures on the Nusselt number.

Pressure Losses

The previous studies focused on the heat transfer performance for different jet configurations. Despite vast amounts of heat transfer information, a significant focus is required on the study of pressure losses. Lower pressure drops are required to ensure sufficient pressure head for external and internal cooling. In addition, study of pressure losses across the jets can provide some inference about the heat transfer trends and make the analysis more comprehensive. The current section presents studies of pressure losses for jet impingement and its dependence over flow and geometric parameters. Studies of Harmon et al. [44, 45] and Jordan et al. [25-27] have been discussed in the previous section, and the following literature adds more details about pressure loss trends. Florschuetz et al. [61] found minimal changes in pressure losses with Reynolds number in flat plate impingement. However, Callaghan et al. [62] observed a slight increase in the discharge coefficients with increased jet Reynolds number. They completed experiments with circular, square, and elliptical orifices and concluded the highest losses are produced by elliptical jets. Patil et al. [43] calculated the loss coefficients for a varying jet to curvature size and jet nozzle length (jet plate thickness). Curvature does not significantly affect the pressure loss, with the greatest curvature having the least loss. A larger nozzle length reduces the pressure loss due to flow development and reattachment in the nozzle. Taslim et al. [63] carried out experiments for pressure losses at the closer jet-to-target surface spacing for flat plate impingement. They found the discharge coefficients to decrease with decreasing spacing. This is due to the limited space for the transition of impingement to channel flow. The quick turn forces the jets to interact with each other and the surfaces, increasing shear stress and flow resistance. Hence, the losses increase, and discharge coefficients decrease. Lee et al. [64] too found

similar dependence for flat plate impingement. Chen et al. [65] experimented with varying jet-to-jet spacing and found that the discharge coefficients increase with spacing. The authors observed reduced cross flow and friction on the target surface as spacing increases.

This thesis aims to correlate Nusselt numbers over various jet geometries, configurations, and flow conditions for the leading edge of a turbine blade. To be specific, the experiment conditions include ranges of the following parameters: the jet-to-jet spacing (s/d) is 2,4,8, jet-to-target surface spacing (z/d) is 2, 4, jet nozzle length (l/d) (jet plate thickness) is 1.33, 2.6, 4, surface curvature-to-jet size (D/d) is 2.665, 5.33 and fillet radius ratio (r/l) is 0, 0.16, 0.18, 0.26 and 0.5 .The existing experiment setup is based on the setup used by Harmon et al. [44, 45]. Initially, the study's objective was to validate the heat transfer results obtained by Harmon et al. [44, 45] and pressure loss results obtained by Jordan et al. [25-27]. Expanding their work, the levels for the following governing factors were increased: Reynolds number, jet-to-jet spacing, jet-to-target surface spacing, jet plate thickness, and jet edge fillet radius (jet edge condition). In addition to heat transfer, pressure loss is carried out for every experiment to assist the experimental investigation.

CHAPTER III

EXPERIMENT FACILITY

Introduction

The experimental setup in this study is the same as used by Harmon et al. [44, 45]. The target surface is instrumented for steady state heat transfer experiments. The test section consists of a square supply duct, an entrance section, and a concave impingement surface to provide a scaled model of the leading edge of gas turbine blades. The flow is conditioned as it enters the entrance section; however, the flow is not yet hydrodynamically developed as it leaves the section. The solid walls of the test section are made from plexiglass. These walls have a thickness of 1.25 cm. Figure 3.1 presents an overview of the experiment setup and figure 3.2 presents a schematic of the overall system with compressed air, mass flow meter and experiment setup.

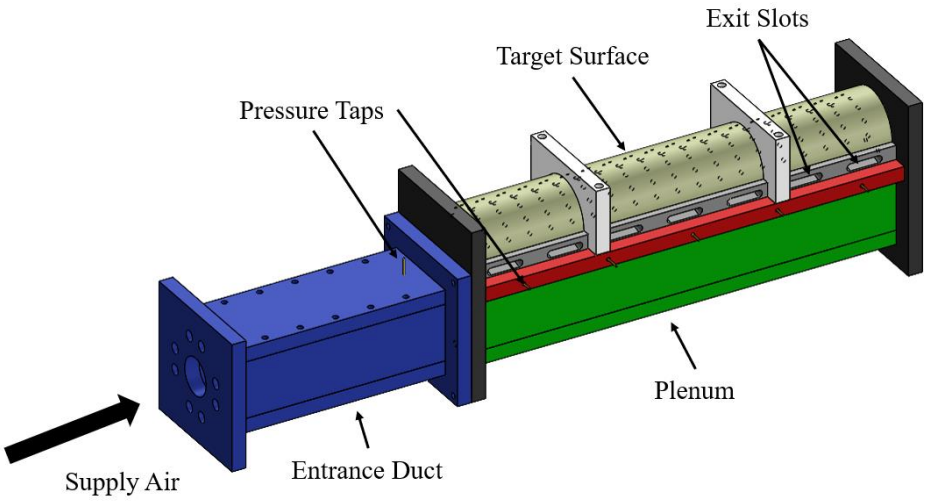

Figure 3.1: Overview of the experiment setup

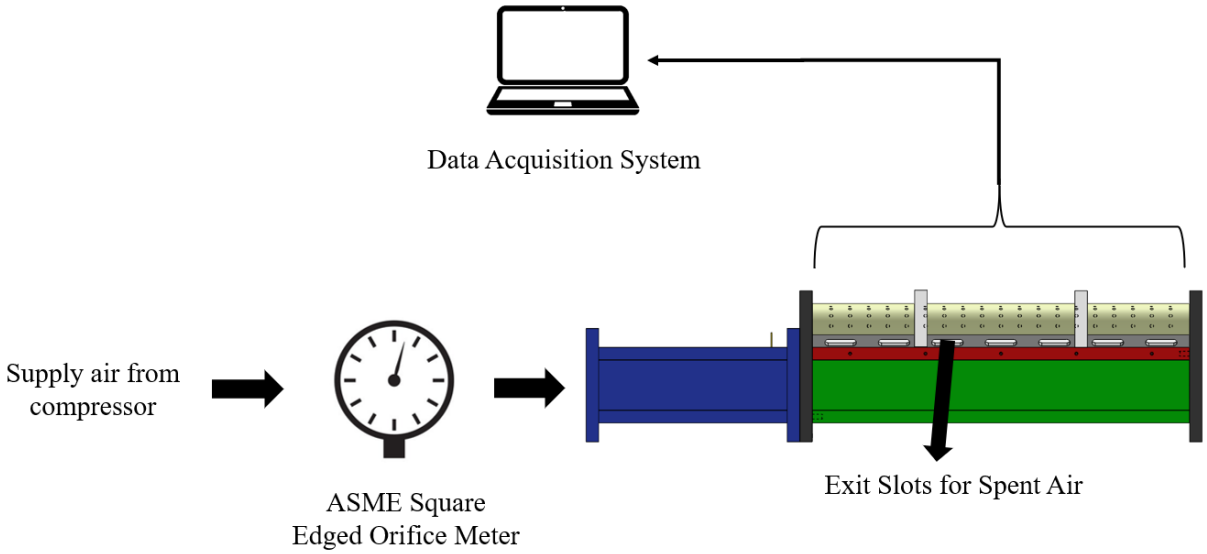

Figure 3.2: Schematic of the test setup

The supply duct is bounded by 3 walls, a blocked exit, and a jet plate at the top. As the air enters the supply duct, it is forced to turn 90 degrees and pass through the orifices on the plate. The plate may have a different number of jets for different orifice shapes and fillet radii. Once the cooling air is used for impingement, it is exhausted to the room with the help of oblong angled slots to remove any potential cross-flow within the impingement cavity. The dimensions of target surface and ejection slots are presented in figure 3.3.

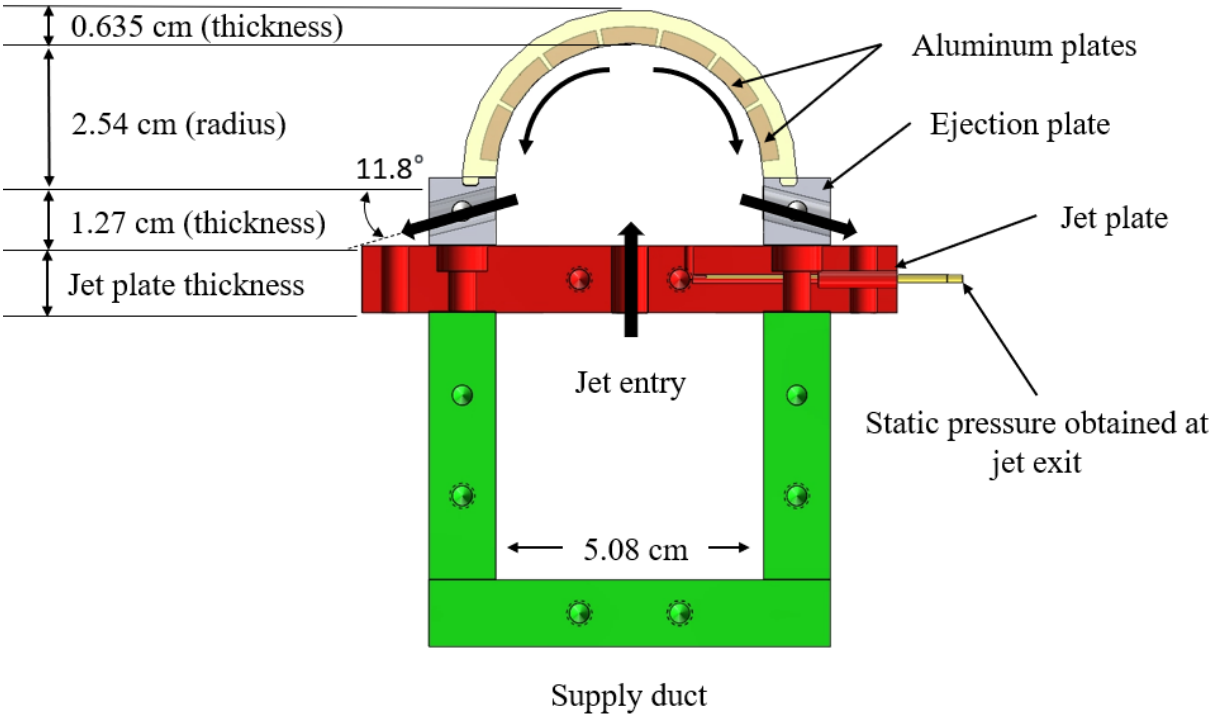

Figure 3.3: Side view of the impingement setup

The curved impingement surface is made of Glass Filled Nylon 12. As shown in figure 3.4, the surface is designed to support nineteen aluminum plates in the streamwise direction, seven aluminum plates around the circumference and heater (not present in the figure). The plates are made from 6061 aluminum with a 2.54 cm inner radius, are 0.3175 cm thick, are 1.75 cm long, and span an arc of 22°. This provides an impingement area of 1.7×10^{-4} square meters. Each aluminum plate is designed to accommodate two T-type thermocouples and a single 6-32 bolt to keep it attached to the surface. A thin film heater is used to heat the backside of the aluminum plates. These plates are separated with a small gap to provide regionally averaged heat transfer coefficients. The heater was custom-manufactured by AllFlex Inc., and it incorporates the pattern of holes as found in the aluminum plates, with 399 through holes. The heater was affixed to the plates with the help of high conductivity (low thermal resistance) paste from Omega

Engineering Inc. In order to provide a smooth target surface, the cured silicone paste is sanded. As mentioned previously, the plates are distributed in the streamwise and circumferential directions. The plates around the circumference are marked by their angular locations, in terms of angle away from the stagnation line. $\theta = 0°$ represent the stagnation line and $\theta = \pm 90°$ indicate the extremes. Schematic of the same is presented in figure 3.4.

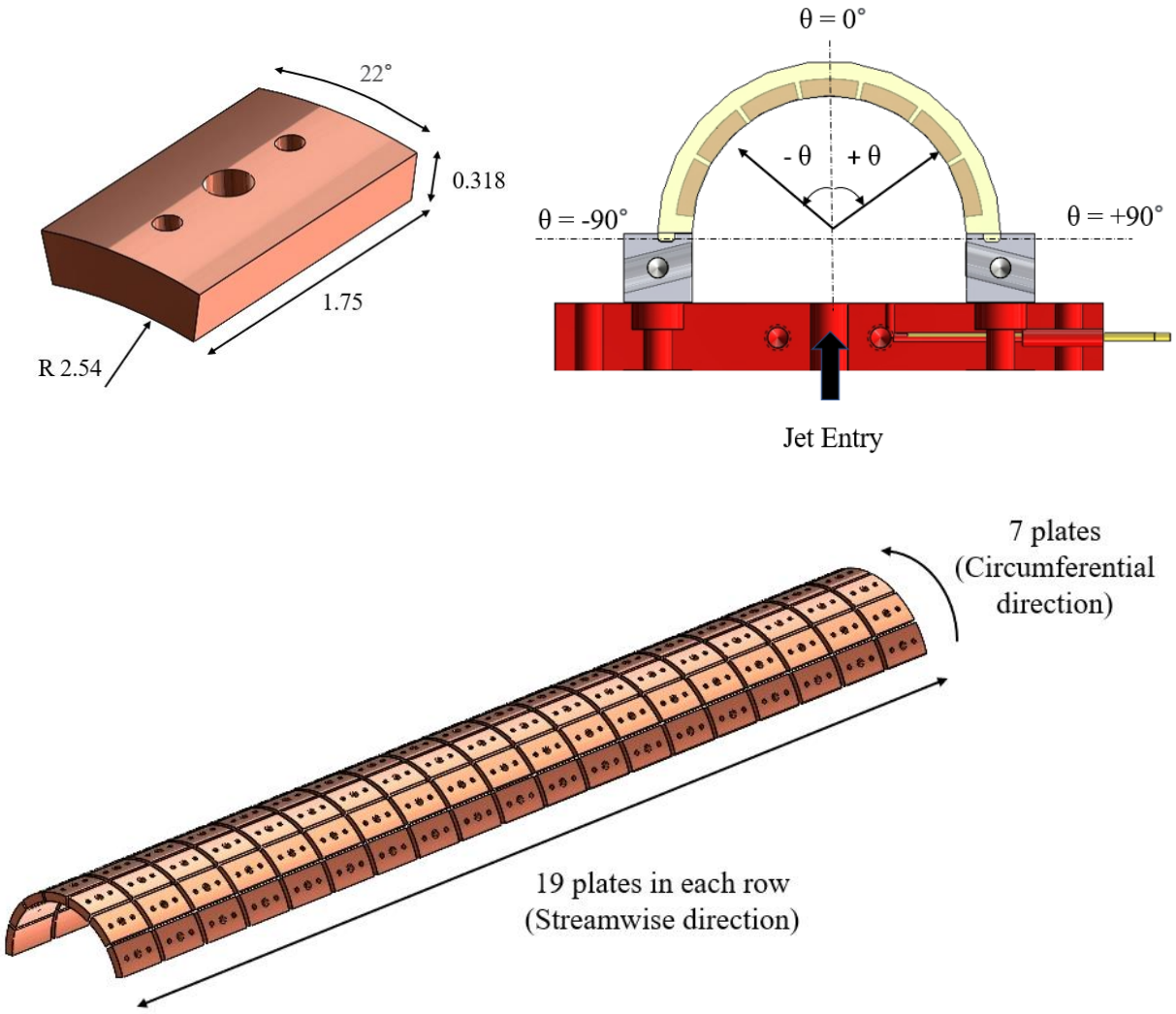

Figure 3.4: (top left) Dimension of the aluminium plate (top right) Plate locations in the circumferential direction (bottom) View of all plates on the target surface

For the experiments, 88 thermocouples were used for measuring the wall temperatures, 5 thermocouples for measuring distinct jet temperatures and one thermocouple for measuring the room temperature. Figure 3.5 presents the active thermocouples for experiments and figure 3.6 present the location of thermocouples for 5 jets. The jet thermocouples are spread across the plate to capture temperature variations and are located at the plate extremes (2), center jet (1) and midway between them (2).

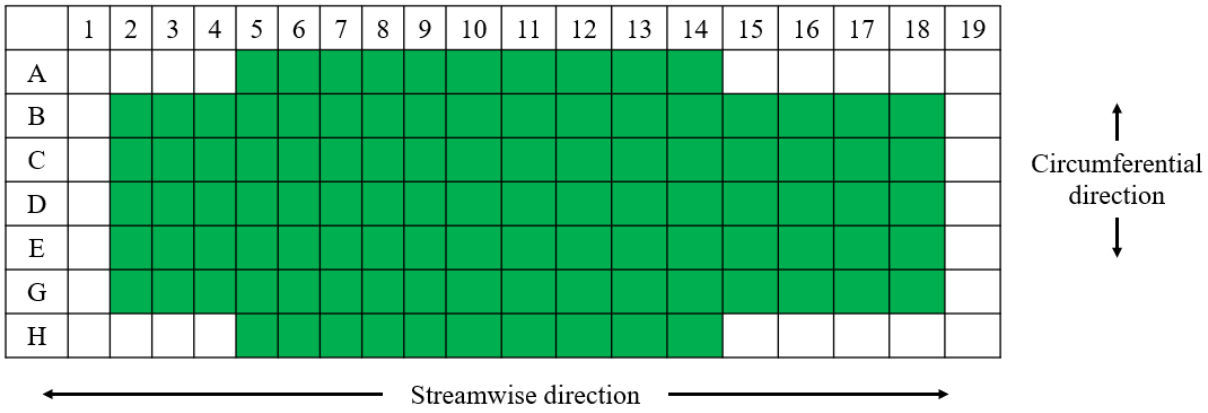

Figure 3.5: Map of active surface thermocouples for the experiments

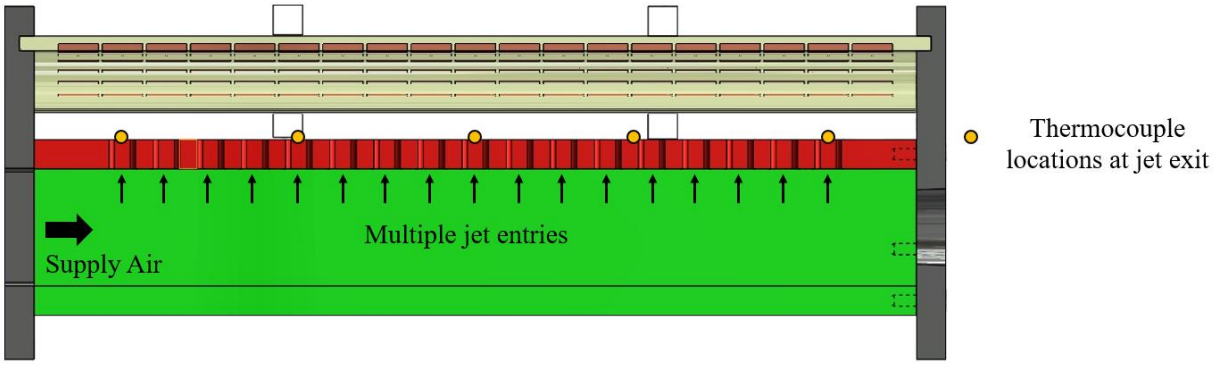

Figure 3.6: View of jet thermocouple locations

The current experimentation involves a minimal temperature gradient across each aluminum plate. Following the lumped capacitance model, and it is necessary to have Biot Number (Bi) less than 0.1. Aluminum, having a relatively high conductivity, is used, and it is necessary to calculate its Biot number, given by:

$$Bi = \frac{h * L_c}{k_{Al}} \quad \textbf{(4.1)}$$

For the range of measured heat transfers coefficients, the Biot number was well under 0.1, indicating that there should be no significant temperature gradient through the aluminum plates. To verify the lumped capacitance model, select aluminum plates were instrumented with two thermocouples (one in each hole), while others used one thermocouple. The select thermocouple locations are highlighted in figure 3.7. The variation between the two adjacent thermocouples is under 0.7% at 323 K (or 50 C).

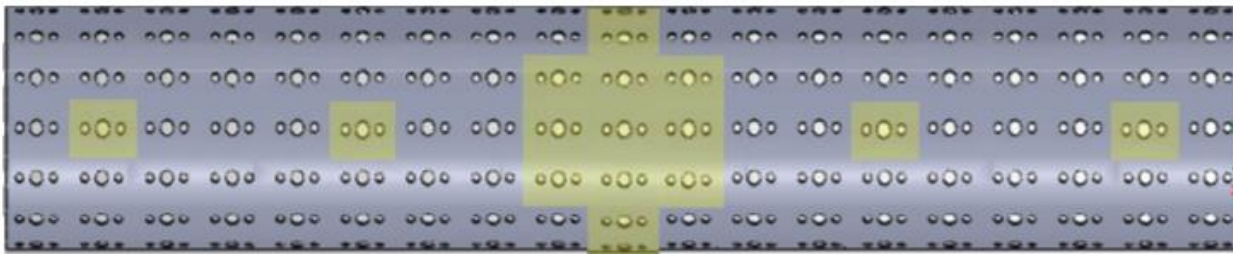

Figure 3.7: Thermocouple locations across the target surface. Shaded thermocouples are used for spot checking

The pressure measurements are essential to calculate the discharge coefficients for the jets. The calculations require total pressure (P_0) and static pressures (Ps) that are recorded from the pressure taps. Figure 3.8 presents the location of the taps, where the total pressure is measured in

the entrance duct and the static pressures are measured for the five jets. The pressures are recorded at the jet exit (as indicated in figure 3.3) with the help of Scanivalve pressure transducer. Calculations pertaining to discharge coefficients are presented in chapter 4 of "Experiment Techniques and Data Reduction".

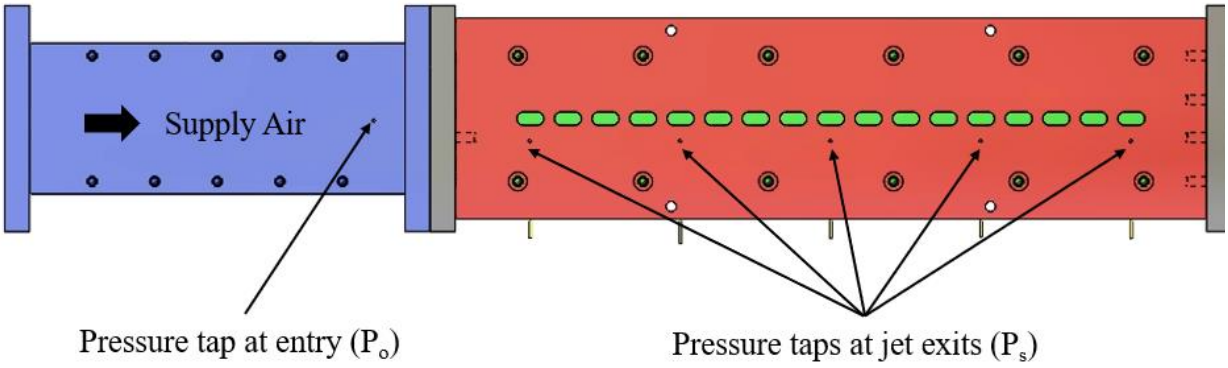

Figure 3.8: Pressure tap locations for measuring total pressure (P_0) and static pressure (Ps) (Top view of the setup)

The test conditions comprise varying flow conditions and jet configurations. The jet Reynolds number is varied from 10,000 to 60,000 (for small jet orifices) and 100,000 (for large jet orifices). The upper limit is to ensure the jet Mach number does not exceed 0.3. Racetrack shaped jets are deployed in all the experiments. The latter is chosen among the choice of either maintaining the same mass flow rates or the same jet Reynolds number across all configurations. This is to ensure reproducibility of the results and maintain consistency for comparison. As data is benchmarked with literature, it is convenient to match Reynolds numbers over the mass flow rates.

Mass Flow Rate Measurements

The ASME square-edged orifice meter is present in the circuit to control the mass flow rates for different experimental conditions. Here, all of the incoming air is used for impingement, then ejected into the room. For calculating the mass flow rates, equation 4.2 from Leary et al. [66] is used:

$$\dot{m} = 0.1145 * D_{orifice}^2 * K * Y * \sqrt{\frac{P_1 * G * y * \Delta P}{T_1}} \quad \textbf{(4.2)}$$

To obtain the pressure upstream of the orifice and pressure drop across the orifice, a pressure differential is used across the flange taps on both sides of the orifice plate. A 10" inclined oil manometer measures the pressure drop across the orifice. This manometer can be operated to a maximum limit of 10 inches with the least count of 0.01 inches for measurements up to one inch and 0.1 inches for measurements beyond one inch.

Before beginning the test, the mass flow rate for the desired jet Reynolds number is calculated using equation 4.2. The jet Reynolds number can be obtained from equation 4.3,

$$Re_{jet} = \frac{\rho * v_{jet} * d}{\mu} \quad \textbf{(4.3)}$$

The hydraulic diameter of the jet orifice can be calculated from equation 4.4,

$$\mathrm{d} = \frac{4 * A_{c,jet}}{P_{jet}} \quad \textbf{(4.4)}$$

Once the jet Reynolds number is obtained, the total mass flow rate needed for each flow condition is calculated using Equation 4.5, which considers the total number of jets.

$$\dot{m}_{Total} = N \cdot \frac{\mu * Re_{jet} * A_c}{d} \quad \textbf{(4.5)}$$

Jet Configurations and Geometries

The focus of the study is towards observing the performance of racetrack jets. These jets have an aspect ratio of 2:1 where the longer axis aligns in the streamwise direction and shorter axis is perpendicular to it. The jet configurations vary jet-to-jet spacing (s/d), jet-to-target surface spacing (z/d), surface-to-jet diameter ratio (D/d), jet nozzle length (l/d) (jet plate thickness) and fillet radius at jet edge (r/l). There are two types of jet sizes used in the test conditions with jet hydraulic diameters being 0.953 cm and 1.906 cm. Jet-to-jet spacings of s/d = 2, 4, and 8 are present for both the jet sizes. The smaller orifice provides z/d of 4 and D/d of 5.33, while the larger orifice provides z/d = 2 and D/d of 2.665. Here d refers to the hydraulic diameter of the jet. For the parameter of jet nozzle length (l/d) (jet plate thickness), the lengths of 1.33d, 2.6d and 4d are present (shown in figure 3.9). For the large diameter, the jet nozzle length (jet plate thickness) becomes 0.665d. Another parameter being investigated is the degree of relative radius (jet orifice fillet radius-to-jet length ratio). This range of the parameter comprises of 0 (for square edged orifice), 0.188 (for smaller fillet), and 0.5 (for larger fillet). Traditionally the impingement studies are concerned with the square-edged orifice plate, which is difficult to manufacture using modern casting techniques. Designers are left with fillets across the jet orifice at the entrance and exit.

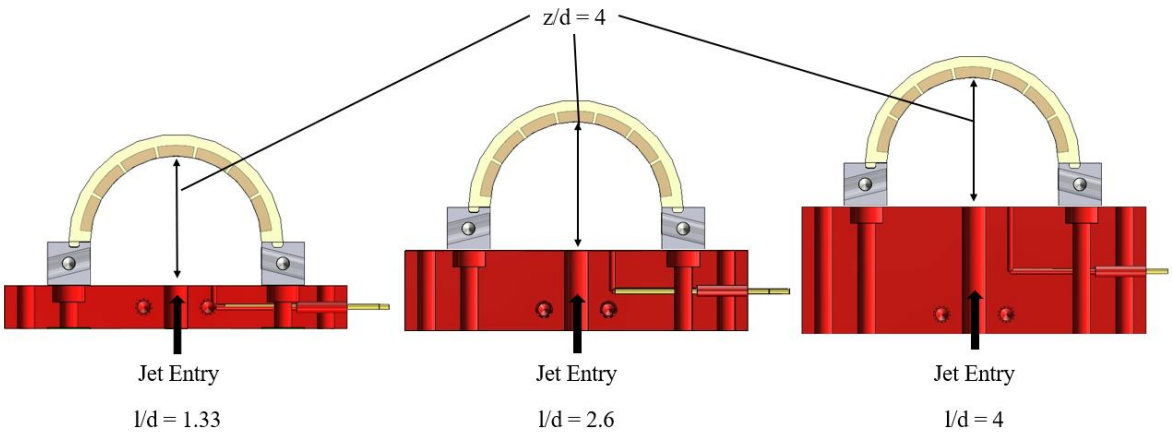

Figure 3.9: Plates representing various jet nozzle lengths (jet plate thickness)

The current test conditions comprise experiments for Reynolds numbers of 10,000 – 40,000 for z/d = 4 and 20,000 – 100,000 for z/d = 2. The upper limit maintains the Mach number less than 0.3 to maintain incompressible flow. In addition to varying flow conditions, the jet geometries such as jet-to-jet distance (s/d), jet-to-target surface distance (z/d), distance upstream of the jets (l/d), curvature-to-jet size effects (D/ d) and jet edge condition (r/d) are varied to investigate their effects on heat transfer and discharge coefficients. The jet plates with possible geometric conditions and edge conditions are presented in figure 3.10 for z/d = 4 and figure 3.11 for z/d = 2. An outline of the tests proposed is presented in Table 3.1 for racetrack jets.

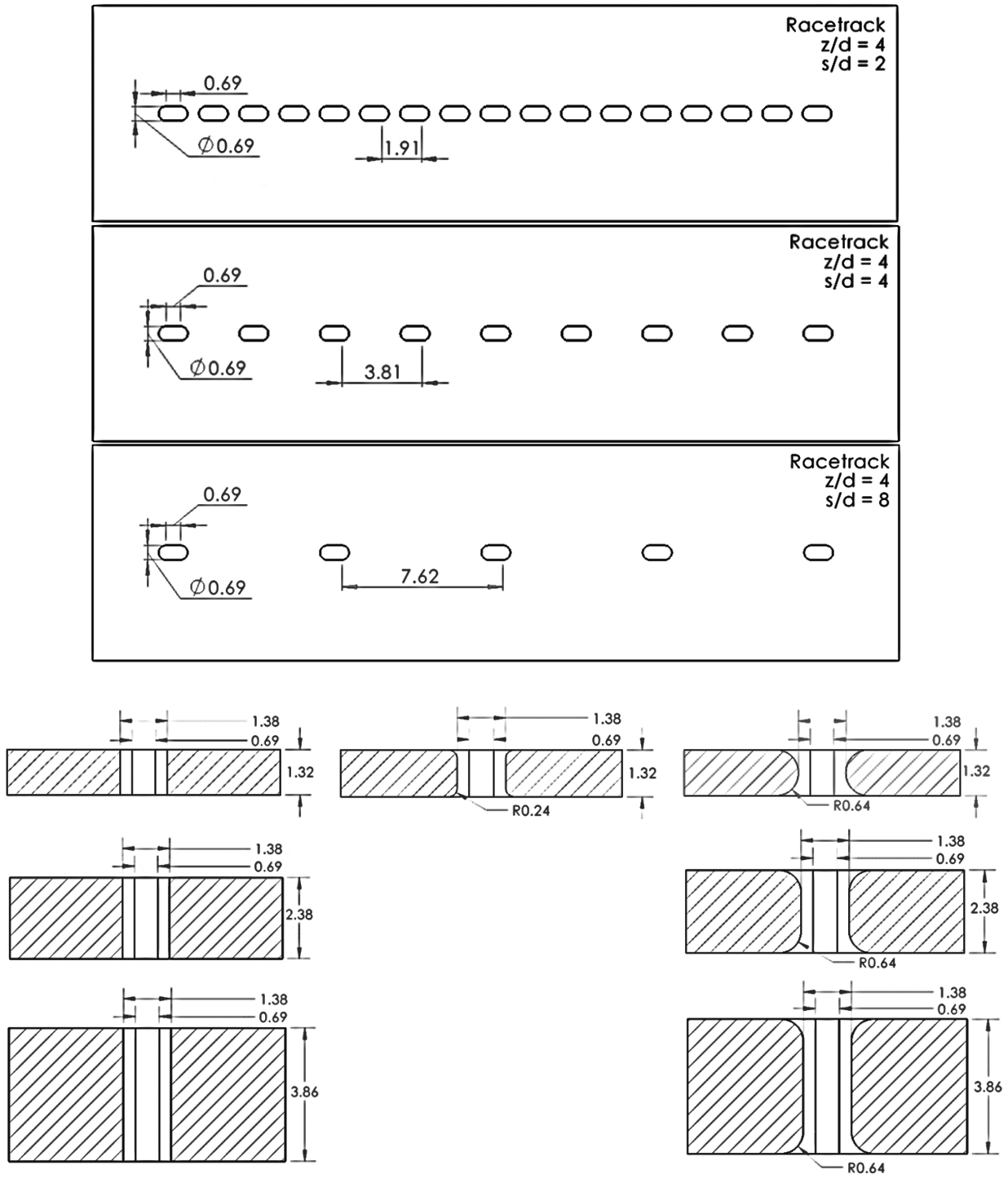

Figure 3.10: Plate Geometries for different jet configurations (for d = 0.953 cm, z/d = 4)

(All dimensions in cm)

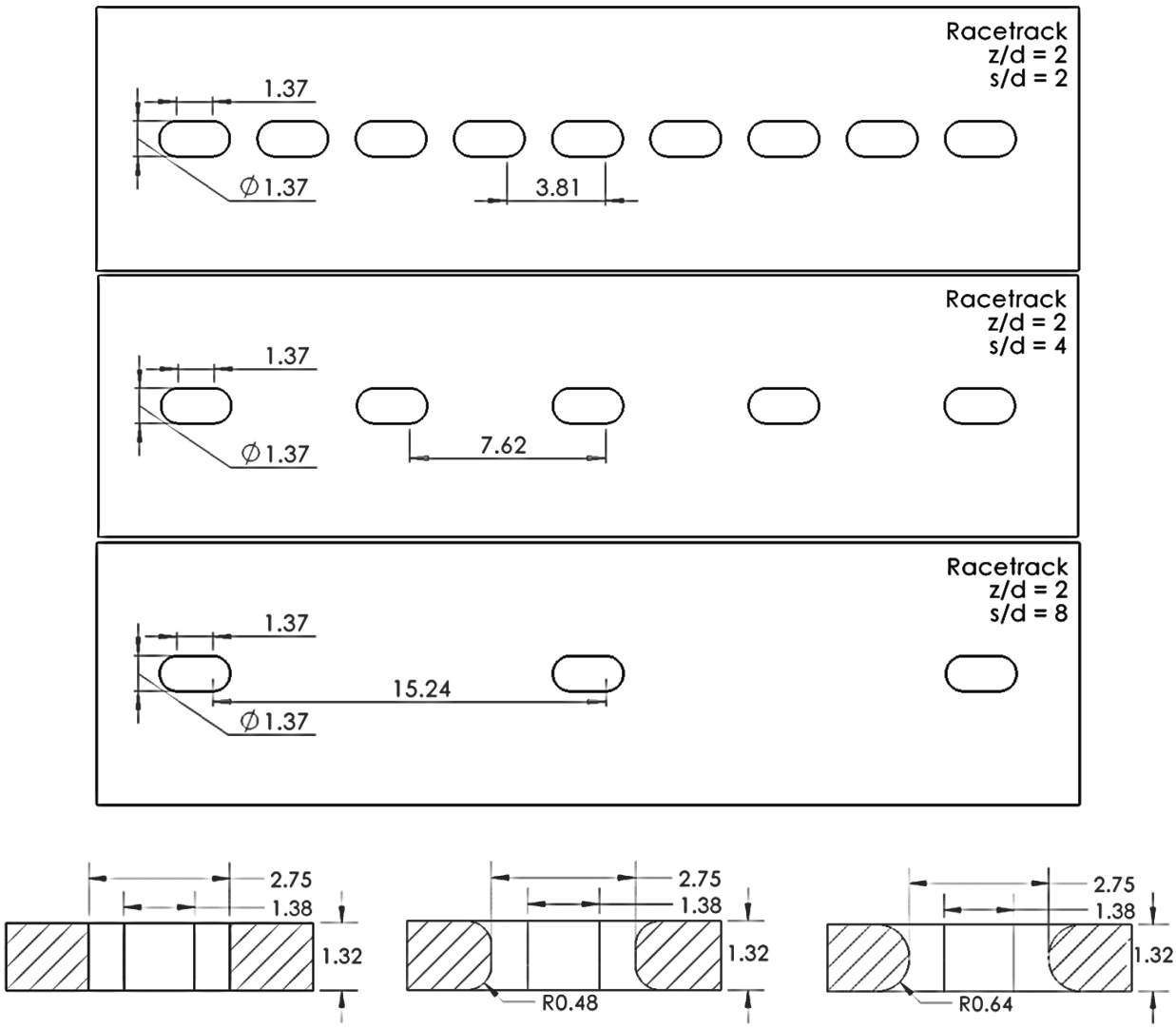

Figure 3.11: Plate Geometries for different jet configurations (for d = 1.906 cm, z/d = 2)

(All dimensions in cm)

Table 3.1: Test cases for jet impingement of racetrack shaped jets

Tests	z/d	D/d	l/d	r/l	s/d	Re
1-24	2	2.665	0.665	0, 0.18	2	10k, 20k, 35k
					4	10k, 20k, 40k, 60k
					8	20k, 40k, 60k, 80k, 100k
25-33	2	2.665	0.665	0.5	4	10k, 20k, 40k, 60k
					8	20k, 40k, 60k, 80k, 100k
34-55	4	5.33	1.33	0, 0.18	2	10k, 20k, 35k
					4, 8	10k, 20k, 40k, 60k
56-63	4	5.33	1.33	0.5	4, 8	10k, 20k, 40k, 60k
64-79	4	5.33	2.6	0, 0.26	4, 8	10k, 20k, 40k, 60k
80-95	4	5.33	4	0, 0.16	4, 8	10k, 20k, 40k, 60k

CHAPTER IV

EXPERIMENT TECHNIQUE AND DATA REDUCTION

Steady State Heat Transfer Technique

The primary objective of the investigation is to measure heat transfer coefficients across the leading edge of the gas turbine blade. In gas turbines, there are high heat loads across different parts of the airfoil. These loads are due to differences in the temperatures of hot gases exiting the combustor and the intrinsic temperatures of the metallic blades. The dominant mode of heat transfer is convection, which is simply the transfer of energy into or out of an object by the movement of nearby fluid. Newton's Law of Cooling directly expresses the internal heat transfer (from Han et al. [67]):

$$\dot{Q} = h \cdot A_s \cdot (T_w - T_c) \tag{3.1}$$

The steady-state heat transfer test is considered to be the most elementary and intuitive to execute. Due to the reproducibility of the test and its credence with time, it is still preferred over more sophisticated methods. Steady state indicates that the heat input, wall temperatures, and fluid temperature are under equilibrium and do not change with time. A test continues until the system achieves steady state. Once this occurs, the temperatures and power inputs are measured, and heat transfer parameters can be established. For the experiments in this thesis, the steady-state copper plate technique is modified to obtain regionally averaged heat transfer coefficients. Due to high cost of copper material and its reduced availability, aluminum, also with a high thermal conductivity, was chosen for the target plates.

In the experiments, steady-state is achieved when temperatures do not change with time. Sufficient time is needed to approach this state and can require one to two hours based on the flow rates and jet configurations. During this time, a fraction of the added heat is dissipated in the ambient environment. In the experiment setup, aluminum plates are connected to the heater and to maintain isolated local heat transfer, small gaps are present between these plates. To ensure smooth target surface, the gaps are filled with low conductivity silicon paste that acts as insulation. However, due to the plates being continuously heated, the temperature difference between the wall temperature and ambient can drive conduction through the insulation material. Essentially this supplied heat is not convected by the coolant and is considered lost and must be taken into account. To evaluate the exact power contributing to convection, a heat loss experiment is completed. In this experiment, the impingement cavity and supply plenum are filled with insulation material, followed by two tests with no airflow in the setup. In the first test, the plates are heated to attain temperatures lower than those in the actual experiments, called the low temperature test. In the second test, the plates are heated to attain temperatures higher than those in the actual experiments, considering the safe upper limit temperatures, called the high temperature test. Voltages (V_{Low} and V_{High}) and resistances (R_{Low} and R_{High}) are recorded for both the tests, and input powers are calculated using the formula:

$$\dot{Q}_{Low} = \frac{{V_{Low}}^2}{R_{Low}} \quad and \quad \dot{Q}_{High} = \frac{{V_{High}}^2}{R_{High}} \tag{3.2}$$

During each of the tests, the room temperature and the wall temperatures are recorded. With the lower limits and upper limits of the two parameters, namely, power and temperatures, a line is plotted. This helps in the linear interpolation of heat loss for a set of experimental conditions.

When the steady-state condition is achieved in the experiment, the voltage, resistance, wall temperature, and room temperature are used to calculate the actual heat loss. This is obtained from the following equation:

$$\dot{Q}_{Loss} = \dot{Q}_{Low} + \frac{\dot{Q}_{High} - \dot{Q}_{Low}}{(T_{High} - T_{Room,High}) - (T_{Low} - T_{room,Low})} \cdot [(T_{Wall} - T_{Room}) - (T_{Low} - T_{Room,Low})] \quad \textbf{(3.3)}$$

Having obtained the heat loss for the experiment condition, it is deducted from the input power to give the net power entering the system:

$$\dot{Q}_{Net} = \dot{Q}_{Input} - \dot{Q}_{Loss} \qquad \text{(or)} \qquad \dot{Q}_{Net} = \left(1 - \frac{\dot{Q}_{Loss}}{\dot{Q}_{Input}}\right) \cdot \dot{Q}_{Input} \quad \textbf{(3.4)}$$

In the current heat transfer calculation, Q_{loss} is divided by Q_{Input} to give the percentage of heat loss for the experiment condition. This percentage is deducted from 100 to give the percentage of net heat input going into the system. The range of heat loss is around 9-10% at Reynolds number of 10,000 and reduces to 2-3% at higher values of 100,000. The net heat is the energy going into the plates and increasing their temperatures, which is cooled by the impinging air jets. Hence, the heat from the plates is conducted to the boundary and is convected by the near-room temperature fluid. The heat transfer coefficient for each plate is calculated by using the equation:

$$h = \frac{\dot{Q}_{Net,i}}{A_{Surface,i} \cdot (T_{Wall,i} - T_{Center\ jet})} \quad \textbf{(3.5)}$$

Where the subscript i refers to the plate number. The surface area used is the area in contact with the fluid, which is the surface facing the jets. As mentioned previously, the coolant (air)

temperatures are obtained by placing five thermocouples and the center jet temperature is chosen for the calculation. These are equidistant from each other and cover the entire region of impinging plates. The wall temperatures are recorded using T-type thermocouples embedded into the backside of these plates. Given the high thermal conductivity of the aluminum plates, it is assumed that there is no temperature gradient in each plate. Spot-checking plates validate this for temperature homogeneity, with the variation being 1-1.5 C and the maximum variation is about 0.7% at the 323 K (or 50 C).

In order to get a non-dimensional value, the Nusselt number is calculated, which includes the local heat transfer coefficient (h_i) for each plate, jet hydraulic diameter (d), and the local thermal conductivity of the fluid (k_{air}). The thermal conductivity is calculated using equation 3.5 from Chowdhury et al. [68], that uses the film temperature, which is obtained as an average of wall temperature and center jet temperature (equation 3.7).

Nusselt number is calculated from the equation 3.8:

$$k\,(T) = -3.225282 \cdot 10^{-15} \cdot T^4 + 1.96488 \cdot 10^{-11} \cdot T^3 - 5.15701 \cdot 10^{-8} \cdot T^2 + 1.0334 \cdot 10^{-4} \cdot T - 6.40447 \cdot 10^{-4} \quad [175\,K < T < 1900\,K] \tag{3.6}$$

$$T_{film} = \frac{T_{wall,i} + T_{Center\ jet}}{2} \tag{3.7}$$

$$Nu = \frac{h_i \cdot d}{k_{air}} \tag{3.8}$$

Pressure Losses

Another objective of the study is to investigate the pressure losses across the jet orifice in the air impingement. These losses are computed as the discharge coefficient, which is given by equation 3.9. The local pressure measurements do not vary significantly across the jets, and for simplicity, the losses are computed for the centreline jet. It is important to mention that the pressure loss tests were carried without heating and were conducted separately from the heat transfer tests. The mass flow rate across the jet is simply the mass flow rate across the supply duct divided by the number of jets.

$$C_D = \frac{V_{jet}}{V_{ideal}} \tag{3.9}$$

V_{jet} can be computed from equation 3.10 using the mass flow rate calculated from the orifice plate and the jets (N). V_{ideal} is the theoretical velocity calculated from equation 3.11, which uses the pressure differential (ΔP) and jet orifice diameter to duct hydraulic diameter (β). For the pressure loss tests, pressure taps are located in the setup – one tap in the entrance duct to measure total pressure (P_o) and five taps in the jet plate to measure static pressures (P_s). The pressure differential is given by the difference between the jet exit static pressure (P_s) and the total pressure of the supply duct (P_o), schematic presented previously in figure 3.8.

The pressures are measured using a pressure transducer from Scanivalve Corporation. The transducer has a range of 20 inches of water ($\simeq$ 5000 Pa) differential

$$V_{jet} = \frac{\dot{m}}{N * \rho_{air} * A_{cross-section,jet}} \quad \textbf{(3.10)}$$

$$V_{ideal} = \sqrt{\frac{2 * (P_o - P_s)}{\rho_{air} * (1 - \beta^4)}} \quad \textbf{(3.11)}$$

Uncertainty Analysis

The uncertainty analysis has been carried out for the discharge coefficients and Nusselt numbers for a sample geometry over the range of Reynolds number. The Kline and McClintock method [69] has been used to calculate the percentage uncertainties for the parameters using the required details and listed in Table 4.1.

Table 4.1: Uncertainty analysis for Nusselt number and discharge coefficients

Jet Reynolds Number	Uncertainties (%)	
	Discharge Coefficient	Nusselt Number
10000	12.5	9.5
20000	11.0	8.2
40000	8.6	7.9
60000	7.1	7.1
80000	6.5	6.9
100000	6.1	6.7

The uncertainties decrease with the increase in jet Reynolds number. At lower Reynolds numbers, the uncertainties are as high as 9.53% due to high heat loss percentage (9-10%). The heat loss decreases with increasing Reynolds number, which is also reflected in the uncertainty trend. For calculation of discharge coefficients, the uncertainties are as high as 12.5% at lower Reynolds number and then decrease further. At lower values, the uncertainties are high

due to lower accuracy of upstream pressure measurements and pressure drop in the inclined manometer. Due to existing low pressure, the effect is multiplied in the density and mass flow rate calculations. However, with increasing Reynolds number, the pressure also increases and the error percentage becomes small.

CHAPTER V

RESULTS

This chapter discusses the results obtained for all experiment conditions. The discussion begins with the validation of experiment setup by comparing the round jet heat transfer to the Nusselt number predicted by an established correlation (Chupp et al. [23]). A brief review is presented for different heat transfer results for racetrack jets over round jets. Once the validation is complete, the individual parametric studies are presented. In order to interpret the heat transfer results, for each parameter, the streamwise and circumferential results are discussed. This provides an idea of the Nusselt number variations and check conformity with the widely accepted trends. The schematic shown in figure 5.1 revisits the nomenclature used such as stagnation line, streamwise direction and circumferential direction. The circumferential plots provide the heat transfer trend of the center jet in the spanwise direction. The variation is presented around the curved surface, with zero degrees corresponding at stagnation point and $\pm$90 degrees nearing the ejecting slots (Figure 3.4 in "Experiment Setup" section). This is followed by studies of stagnation Nusselt number variation with Reynolds numbers for each parameter. In these discussions, trends are observed for the stagnation Nusselt number over varying parameters and flow conditions. Combining all the data, a comprehensive plot is presented that contains the heat transfer results for all the experiment conditions. Concluding in the heat transfer section, the data is used to develop a comprehensive correlation. As a starting point, a baseline condition is identified and used for comparison: Reynolds number = 20,000, jet-to-jet spacing (s/d) = 8, jet-to-target surface spacing (z/d) = 4, jet nozzle length (jet plate thickness) (l/d) = 1.33 and fillet radius (r/l) = 0.

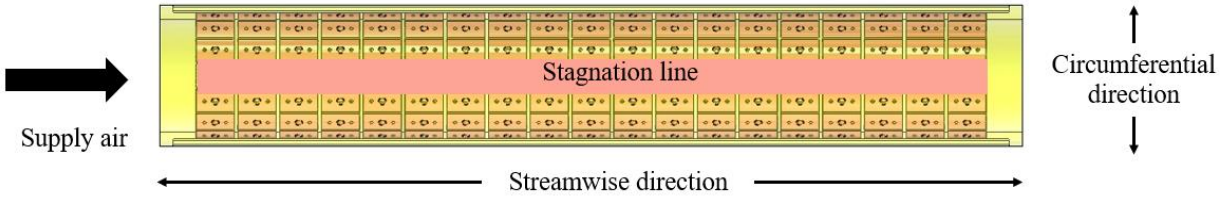

Figure 5.1: Representation of nomenclature used in results

As the heat transfer patterns present cyclic distribution of peaks and valleys, a period across the center jet is chosen for calculating the stagnation average Nusselt number. The Nusselt numbers are averaged across the plates in that period to obtain the stagnation value. Each period is comprised of different number of plates, which is based on the jet size and jet configuration. Figure 5.2 shows all the combinations for varying jet-to-target surface spacings and jet-to-jet configurations.

Figure 5.2: Plates chosen for calculating stagnation average Nusselt number

To make the discussion more comprehensive, a similar pattern of discussion is carried out for discharge coefficients. Discharge coefficients are measured for every experiment condition and investigated for heat transfer performance. However, the pressure losses are measured at room

temperature. The individual, parametric effects are observed and correlations are presented for the active data set. Due to the presence of different levels for many parameters, it becomes difficult to understand the results. In order to make the discussion more focused towards the trends, it is essential to mention the legends of the plots. Figure 5.3 lists out the key for interpreting the plots and is consistent throughout the section.

Parameter	Legend Type	Representation
l/d = 1.33	Dashed	
l/d = 2.6	Dashed dot dot	
l/d = 4	Dotted	
z/d = 2	No fill	
z/d = 4	Fill	
r/l = 0	Circle	
r/l = 0.16	Square	
r/l = 0.18	Delta	
r/l = 0.26	Gradient	
r/l = 0.5	Diamond	
s/d = 2	Red	
s/d = 4	Blue	
s/d = 8	Black	

Figure 5.3: List of representation for various geometric parameter

For example, a plot containing red, dashed lines, with filled circles, represents a jet configuration with jet-to-jet spacing of 8 diameters, jet nozzle length (jet plate thickness) of 1.33 diameters, jet-to-target surface spacing of 4 diameters and fillet radius of 0.

Heat Transfer

Validation of Experimental Setup

For the validation of the experimental setup, six experiments are carried out for Reynolds numbers of 10,000, 15,000, 20,000, 40,000, 50,000 and 60,000 using round jets (d = 0.953 cm). For each of the conditions, the following parameters are held constant: jet nozzle length (jet plate thickness) (l/d = 1.33), jet-to-jet spacing (s/d = 8), jet-to-target surface spacing (z/d = 4), and fillet radius ratio (r/l = 0), representing the square edged orifice. The results are presented in figure 5.4. In addition, the data for the racetrack shaped jets are also presented for the same set of parametric conditions and experimented for Reynolds number of 10,000, 20,000, 40,000 and 60,000.

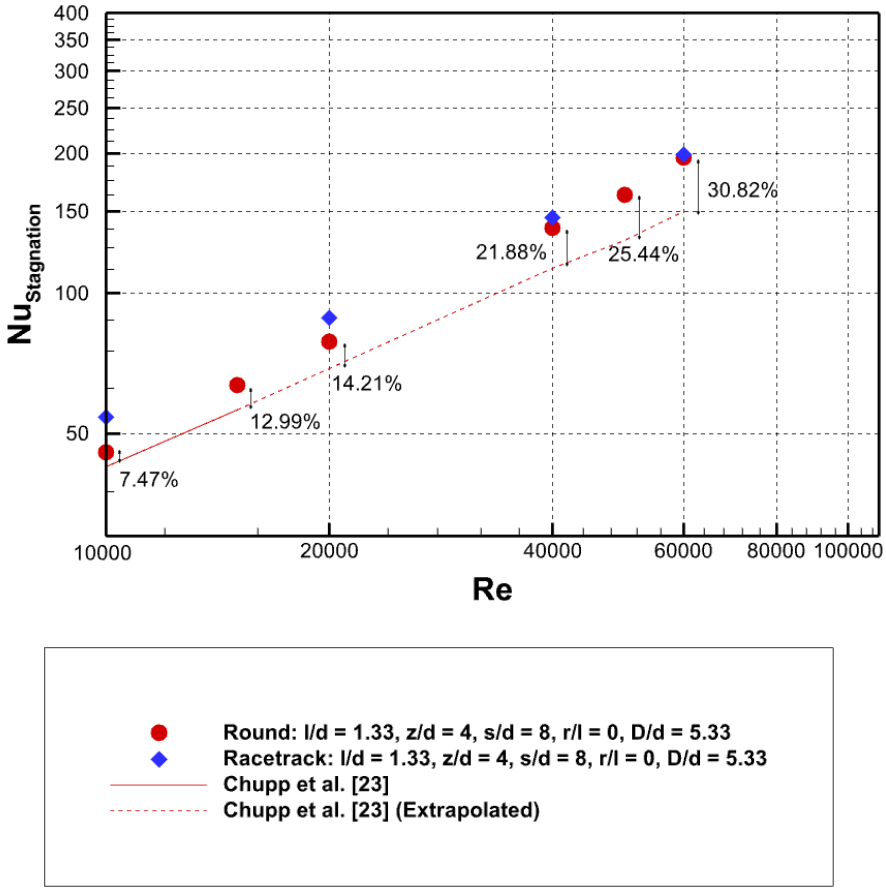

Figure 5.4: Nusselt number variation with Reynolds number for round jets, Chupp et al. [23] correlation and racetrack jets

The stagnation region Nusselt numbers deviate approximately 10% from the correlation at low Reynolds numbers. The established correlation has stated limits for Reynolds number of 3,000-15,000, and error can be introduced if the correlation is extrapolated. Based on the data within the range, the results provide an acceptable comparison. So further conditions can be considered. In addition, the plot presents higher heat transfer for racetrack jets over round jets for the same configuration. This is in accordance with the results in the literature review and is attributed to a larger stagnation area, resulting in increased overall stagnation Nusselt number value. However, due to the greater cross sectional area in racetrack jets, they also utilize more

mass flow, when compared for the same Reynolds numbers. If the mass flow rates were held constant for both, the racetrack would have lower Reynolds numbers than round jets and may lead to lower heat transfer results.

Effect of Reynolds Number

The generally accepted trend has been that the Nusselt number always increases with the Reynolds number. Figure 5.5 presents the streamwise stagnation Nusselt number variation with Reynolds number. Due to the jet-to-jet spacing of 8 diameters, the peaks and valleys are present 8 diameters apart. The supply air enters the plenum from the left. Figure 5.6 presents the circumferential Nusselt number variation with the Reynolds number across different target plates (or circumferential direction). Zero degrees corresponds to the apex (stagnation point) and movement away from the stagnation are presented as positive or negative angles. The heat transfer decreases moving away from the stagnation point. From both figures, it is quite clear that the Nusselt number increases with Reynolds number.

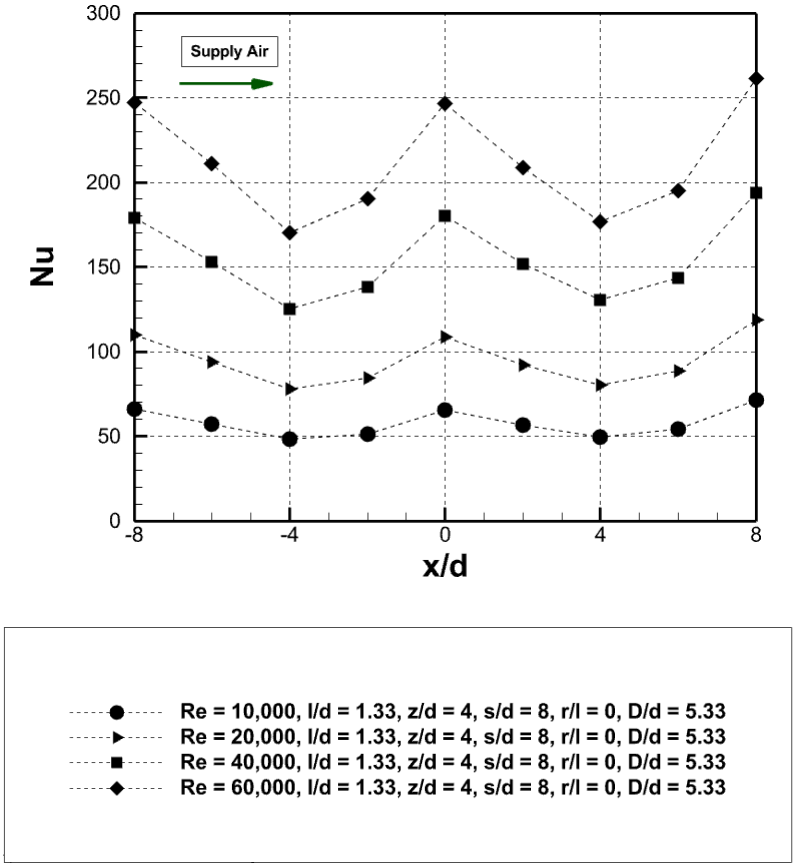

Figure 5.5: Stagnation Nusselt number variation with Reynolds number in streamwise direction

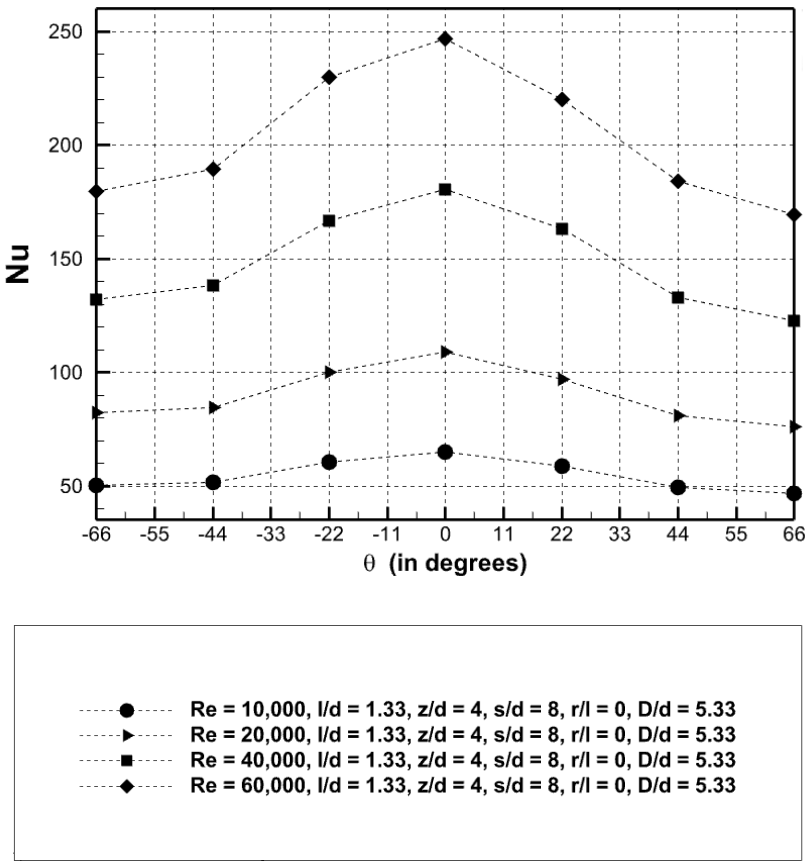

Figure 5.6: Nusselt number variation with Reynolds number in circumferential direction

Effect of Jet-to-Jet Spacing

The jet-to-jet spacing is usually associated with mixing between the jets and increased heat transfer. An inverse relationship between jet spacing and heat transfer has been observed: increasing jet-to-jet spacing led to lower heat transfer. Figure 5.7 presents the Nusselt number variation in the streamwise direction, for a fixed Reynolds number of 20,000. It is important to notice that the different jet configurations provide different numbers of heat transfer peaks. For s/d = 8, the peaks appear 8 diameters apart, for s/d = 4, the peaks appear 4 diameters apart and for s/d = 2, the peaks are continuous with 2 diameters apart. Figure 5.8 presents the Nusselt number variation in the circumferential direction. From the plots, the Nusselt number increases with

decreasing spacing. This can be attributed to greater mixing between the jets at jet-to-target surface spacing of 4 diameters. However, reducing the s/d means stacking more jets in the same impingement area. This means adding four more jets while moving from s/d = 8 to 2. While the mass flow rate is increased by four times, the heat transfer is only increased by 28%. This suggests that enhanced cooling takes place at the cost of increased mass flow rate.

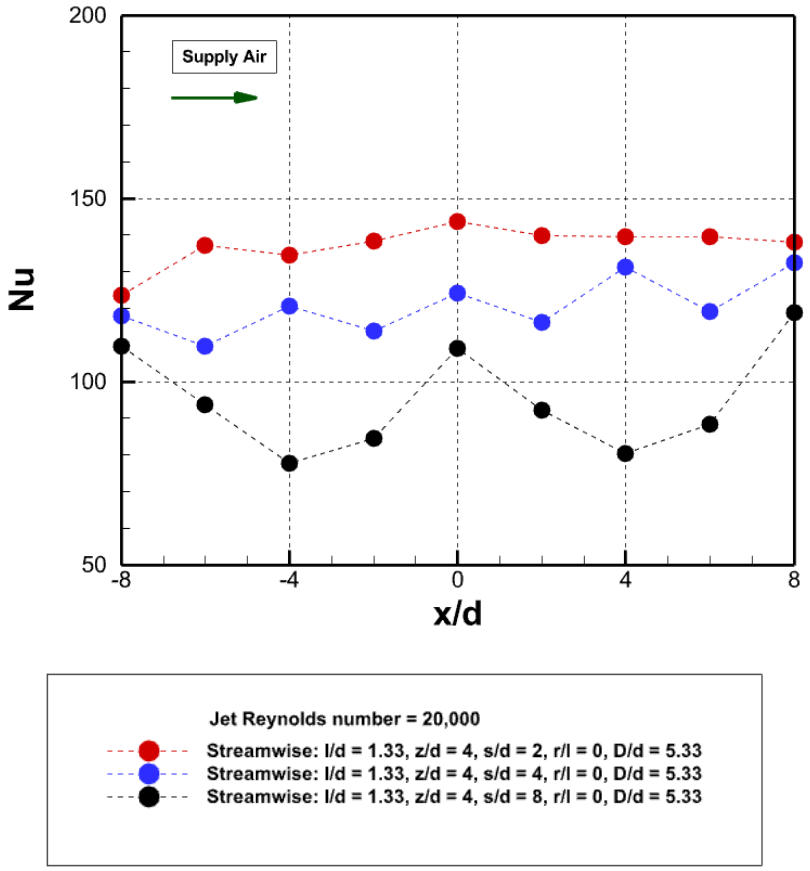

Figure 5.7: Stagnation Nusselt number variation with jet-to-jet spacing in streamwise direction

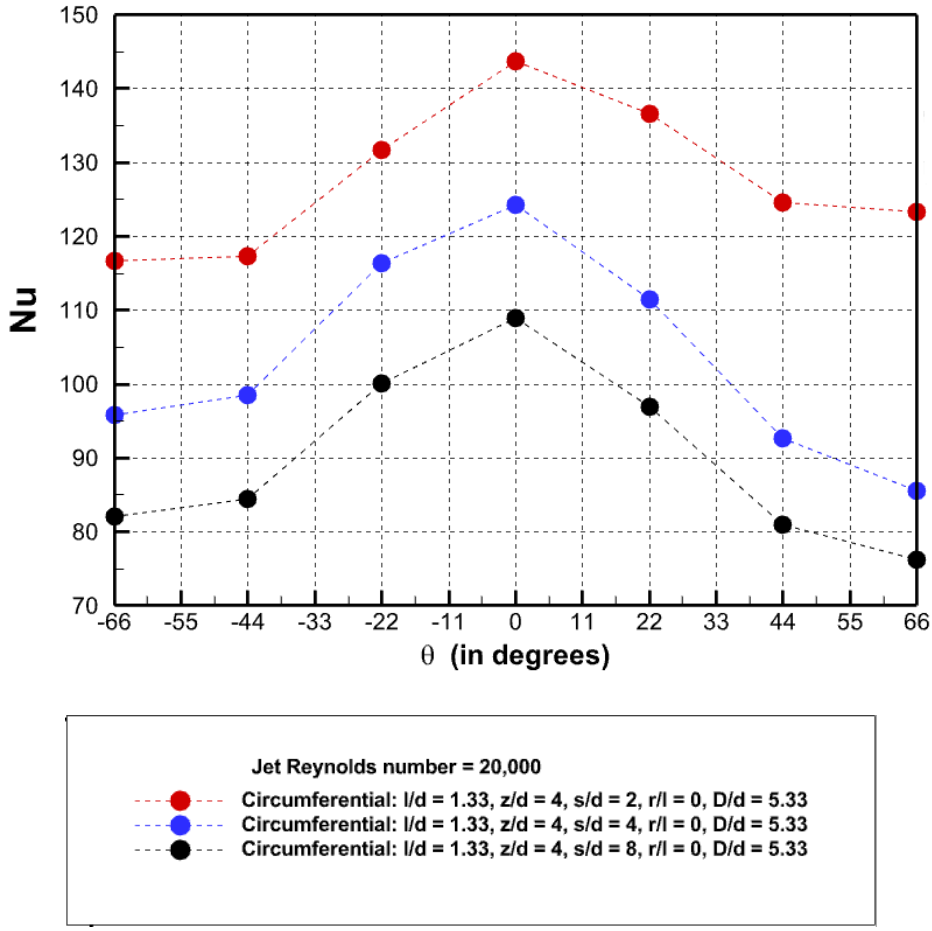

Figure 5.8: Nusselt number variation with jet-to-jet spacing in circumferential direction

The stagnation region, average Nusselt numbers can also be reported. Figure 5.9 shows the combined effects of jet-to-jet spacing and Reynolds number. From the log-log figure, it can be seen decreasing the spacing, increases the heat transfer coefficients. Furthermore, the effect of Reynolds number is also clearly shown. With the three sets of data being nearly parallel, a similar exponent for the Reynolds number in the power law equation is expected.

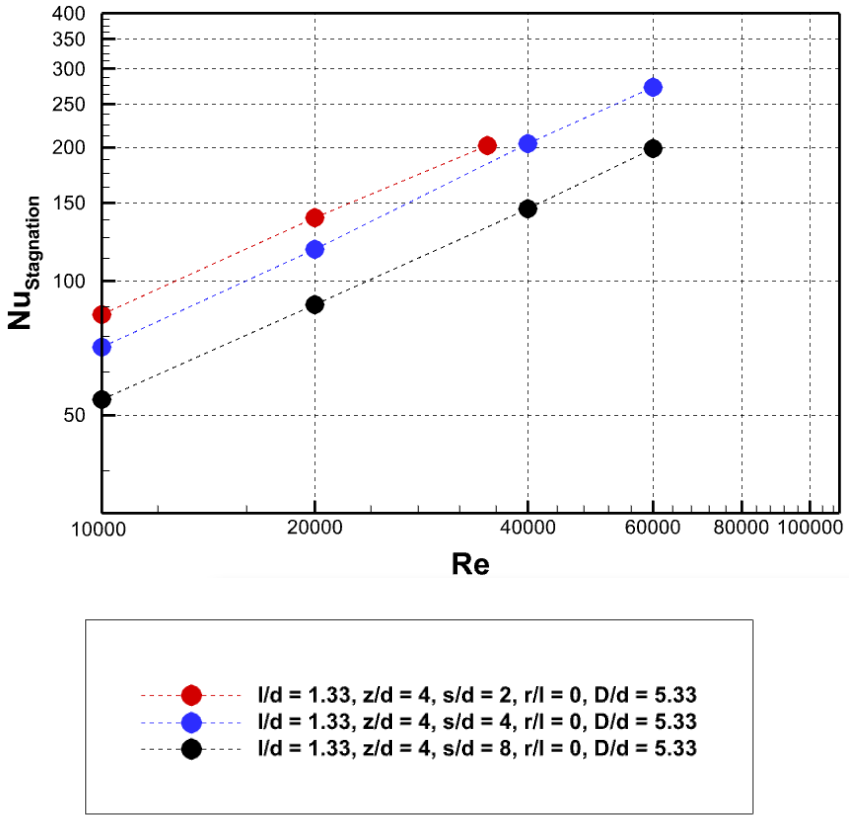

Figure 5.9: Stagnation Nusselt number variation with Reynolds number and jet-to-jet spacing

Effect of Jet-to-Target Surface Spacing

The effect of jet-to-target surface spacing is interesting, and different studies present discrepancies, as discussed in the literature review section. The conflict is between the forever increasing Nusselt number with jet-to-target surface spacing and no effect on heat transfer within the potential core. Figure 5.10 presents the stagnation Nusselt number variation with the spacing in the streamwise direction. From the results, it seems that the decreasing spacing increases the heat transfer. However, due to the geometric plate constraints, there is also a reduction in the jet nozzle length (l/d) (jet plate thickness) from 1.33 diameters to 0.665 diameters and curvature-to-jet size (D/d) from 5.33 diameters to 2.665 diameters. The coupled effect of three changing parameters (z/d, l/d and D/d) produces an increase in the heat transfer. The effect of reduced jet length does not allow recovery of the flow separation due to the vena contracta effect. This promotes a greater jet velocity downstream of the jet and hence has more heat transfer. Due to reduced jet length, there is also associated increased pressure losses (discussed in the "Pressure Losses" section).

Figure 5.11 presents the Nusselt number variation with the spacing in the circumferential direction. From the results, it seems that at a closer spacing, there is little variation in heat transfer around the circumference. This is due to the larger size of the jet orifice and greater coverage of peak Nusselt numbers across the impingement area. The relative sizes of the jets and the impingement area differences are presented in the figure 5.12 for reference. Thus, increasing the jet size helps improve the heat transfer distribution, reducing the gradients and ensure peak Nusselt numbers across larger areas.

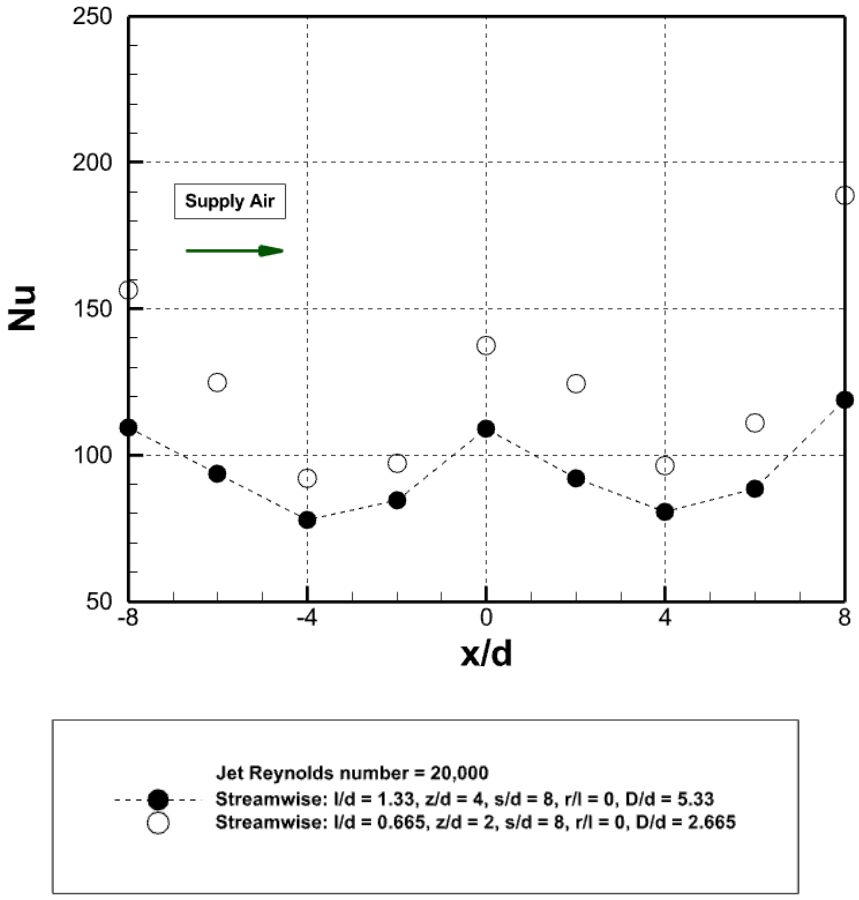

Figure 5.10: Stagnation Nusselt number variation with jet-to-target surface spacing in streamwise direction

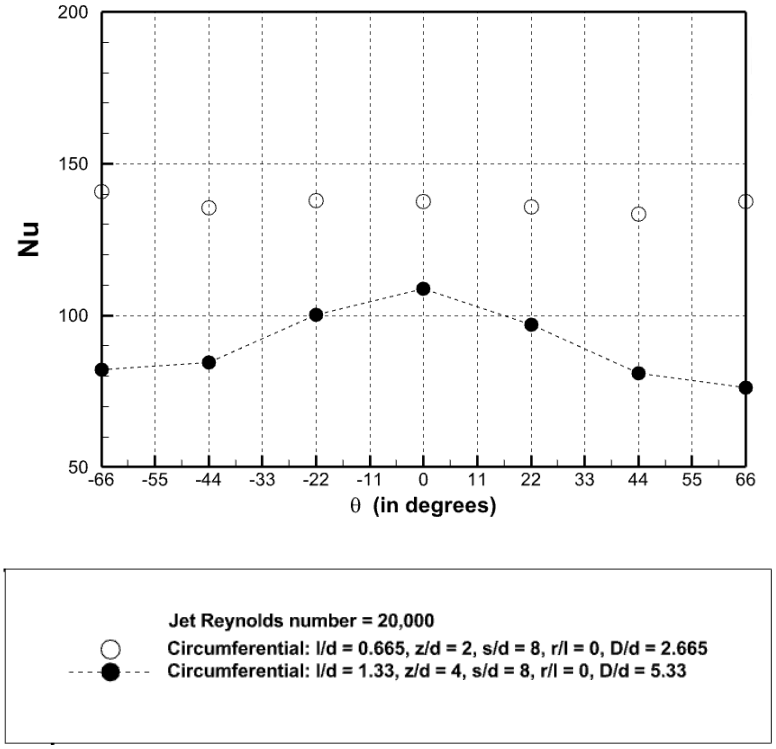

Figure 5.11: Nusselt number variation with jet-to-target surface spacing in circumferential direction

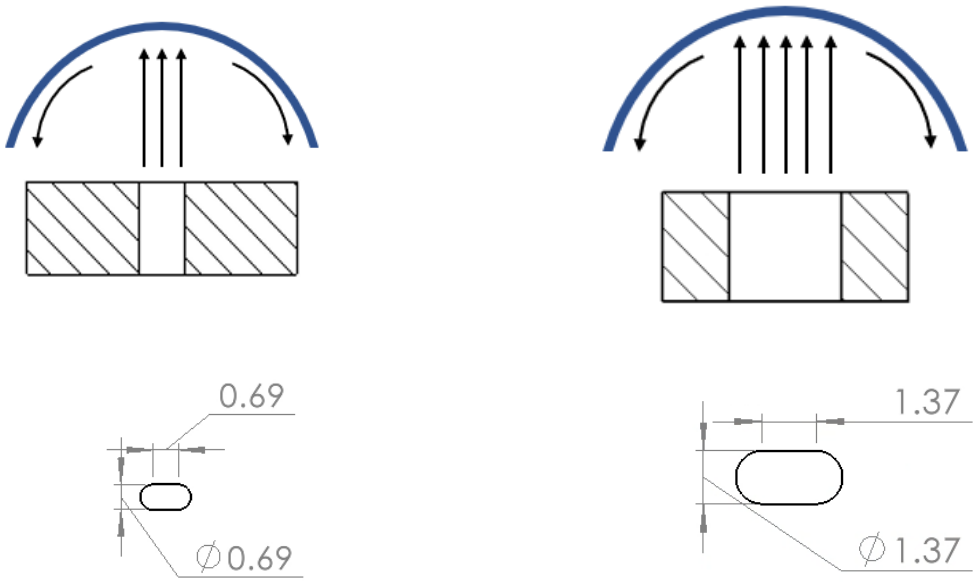

Figure 5.12: Schematic of differences in impingement areas due to different jet sizes

The stagnation strip average, shown in figure 5.13 further depicts this trend: increased heat transfer with reduced jet-to-target surface spacing, reduced jet length and reduced curvature-to-jet size.

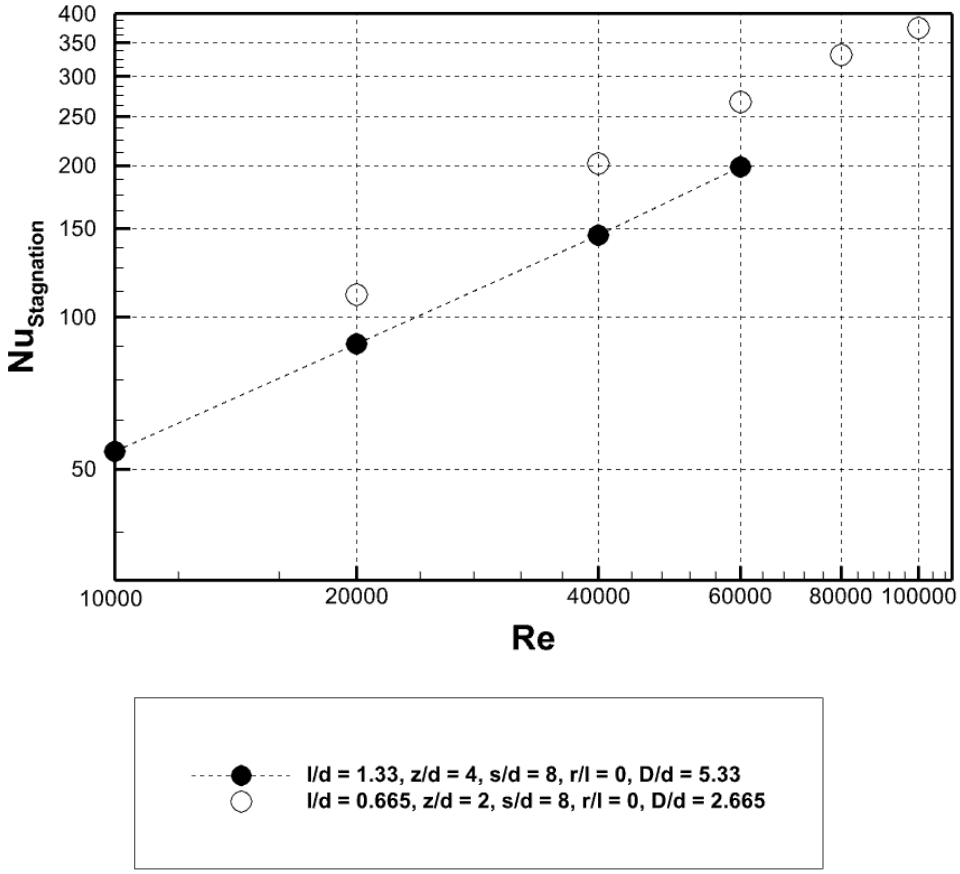

Figure 5.13: Stagnation Nusselt number variation with Reynolds number and jet-to-target surface spacing

Effect of Jet Nozzle Length (Jet Plate Thickness)

Little work has been completed to understand the effect of jet nozzle length (jet plate thickness) on the heat transfer. From the literature, a longer jet length allows the flow to recover after separation and reduce the vena contracta effect. This results in lower jet velocities and lower heat transfer. Figure 5.14 presents the Nusselt number variation along with stagnation strip and figure 5.15 presents the Nusselt number variation in circumferential direction for various jet lengths. The results are interesting as the Nusselt number trend is not monotonic with jet nozzle length (jet plate thickness). For shorter jets (l/d = 1.33), the heat transfer is maximum due to the vena contracta effect, flow separation and increased jet velocity downstream of the orifice exit (as shown in figure 2.6). For longer jets, the heat transfer decreases as they provide recovery from the flow separation and flow development. However, the recovery length is short and once the jet is recovered, the structure of the jet does not change. This can be observed from similar Nusselt numbers for the jet length (jet plate thickness) of 2.6 diameters and 4 diameters. By observing the streamwise variations for all plate thicknesses, there seems to be some disparity in the heat transfer when moving from left to right, or between upstream and downstream regions. For shorter jets, the downstream Nusselt numbers are higher than upstream. This difference is reduced with increasing thickness. Plate thickness of 4 diameters seems to have nearly symmetrical profiles.

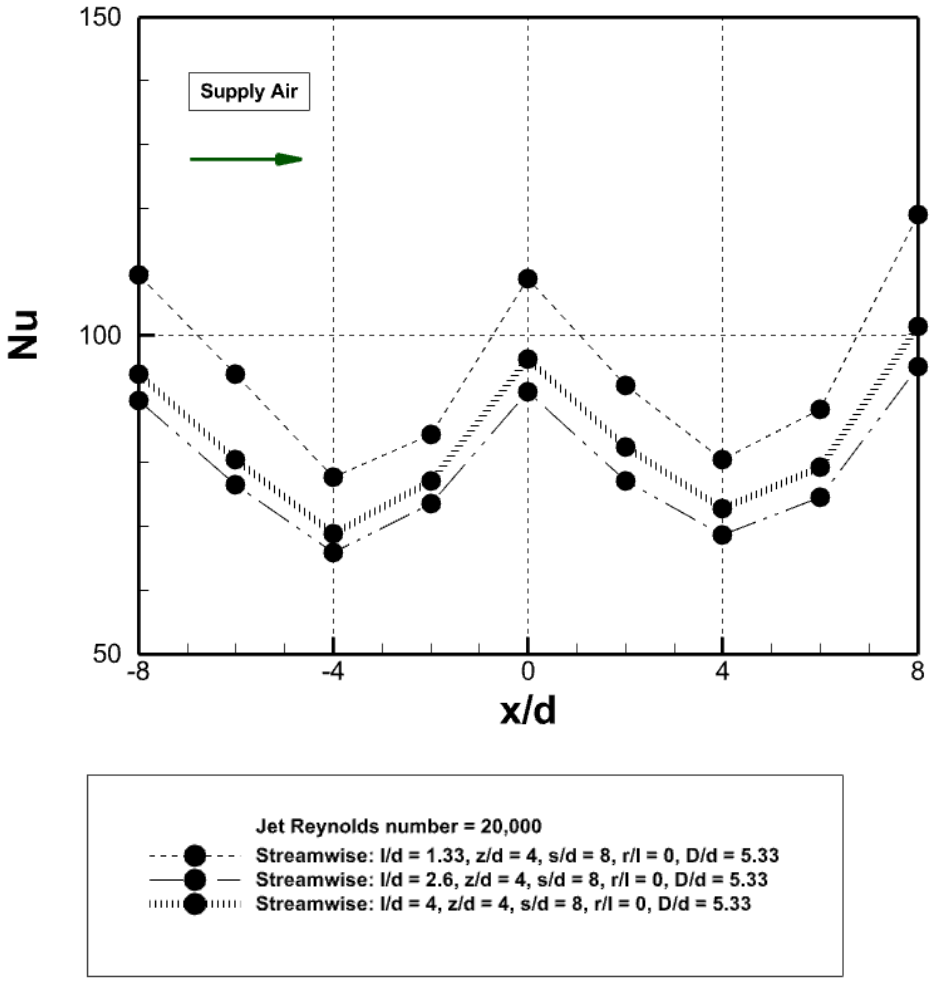

Figure 5.14: Stagnation Nusselt number variation with jet nozzle length (jet plate thickness) in streamwise direction

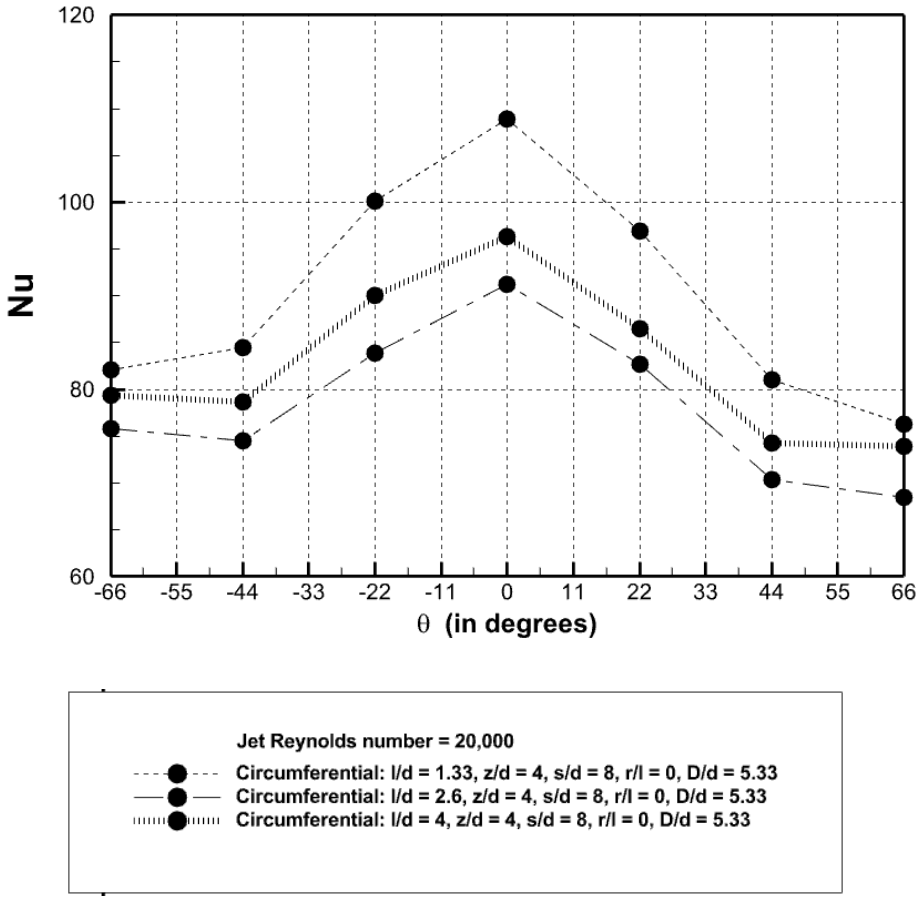

Figure 5.15: Nusselt number variation with jet nozzle length (jet plate thickness) in circumferential direction

From figure 5.16, the stagnation region average Nusselt number trends show minimal difference between jet nozzle lengths (jet plate thickness) of 2.6 and 4 diameters at high Reynolds numbers. At lower Reynolds numbers, the reattachment length could be longer due to lower turbulence and the nozzle length becomes important. However, at higher Reynolds numbers, boundary layers are thin, the reattachment length is short and the nozzle length does not affect the heat transfer. With this result, it seems that thicker plates do not affect the heat transfer and is a favorable condition for industrial blade designers. Thicker plates lead to more mass and might be counterproductive on a broader scale, if the structural integrity is met. Thus, thinner plates would

be a pleasant tradeoff with meeting the objectives of minimum weight without reducing heat transfer. However, it is important to understand that the current experiment does not involve crossflow effect. Studies of Harmon et al. [44, 45] have concluded that thicker plates allow the jets to reorient, due to the longer channels, and minimize the jet deflection. Hence, thicker plates are instrumental to minimize crossflow, whereas, they may produce no effect in heat transfer enhancement for direct impingement.

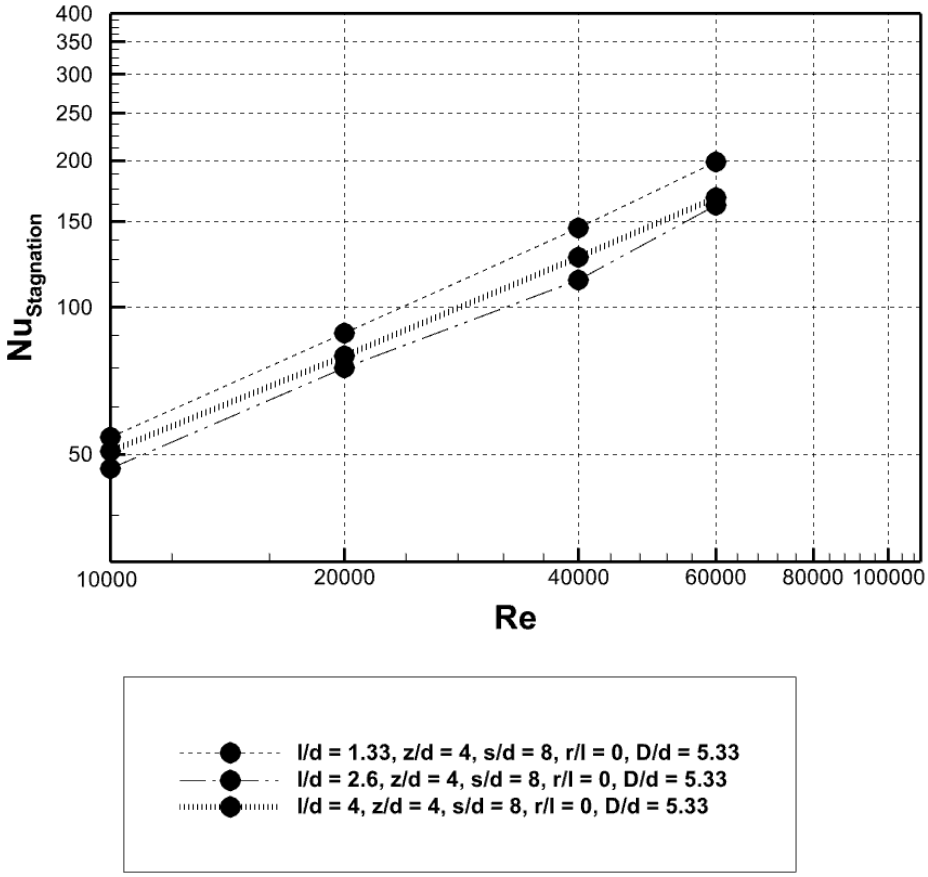

Figure 5.16: Stagnation Nusselt number variation with Reynolds number and jet nozzle length (jet plate thickness)

Effect of Jet Orifice Edge Condition

The edge condition of the orifice has been considered by other groups, and heat transfer is reduced heat transfer with the presence of fillets. Figure 5.17 presents the stagnation strip Nusselt number variation with edge fillet in the streamwise direction and figure 5.18 presents the Nusselt number variation with edge fillet in the circumferential direction. Results do show that the heat transfer is reduced with the presence of the fillets. Increasing the fillet radius does not necessarily reduce heat transfer significantly as the results for r/l = 0.18 and r/l = 0.5 seem to have negligible differences. This is also seen with the stagnation region average Nusselt number variation in figure 5.19. The addition of the fillet at the jet edge reduces the vena contracta effect at the upstream and does not have constrictions for the flow to accelerate. Devoid of this constriction, the jets are not accelerated and hence there is reduced heat transfer. While fillets are an artifact of manufacturing, they will also reduce pressure loss through the jet plate.

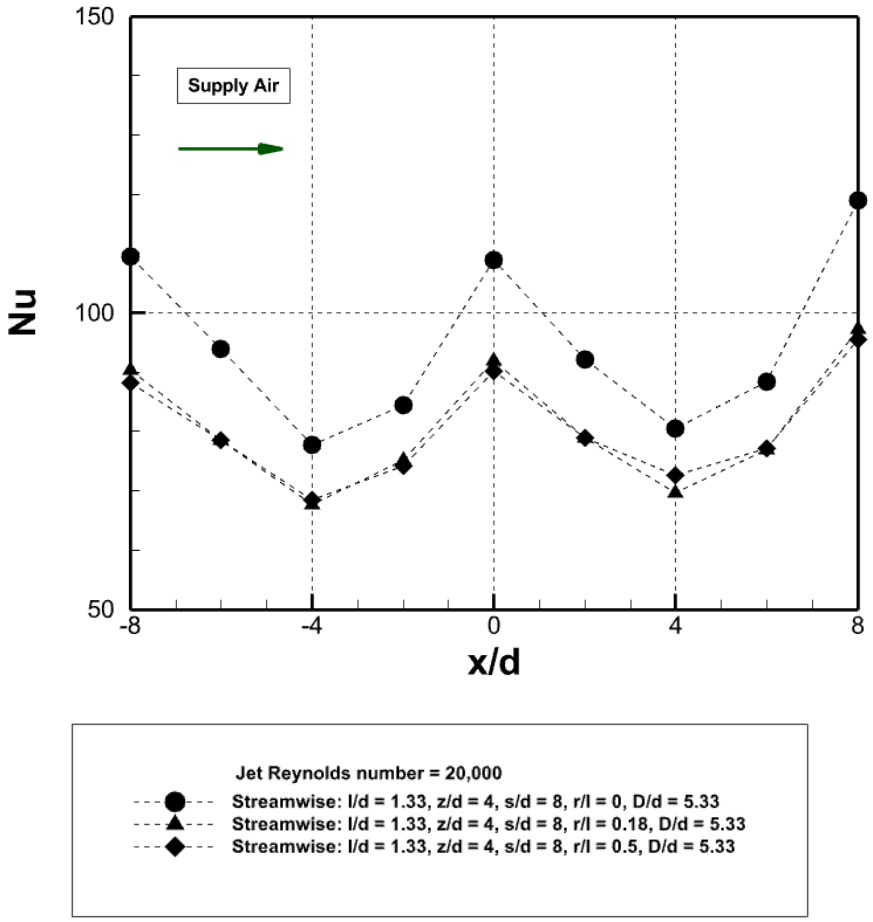

Figure 5.17: Stagnation Nusselt number variation with jet edge fillet radius in streamwise direction

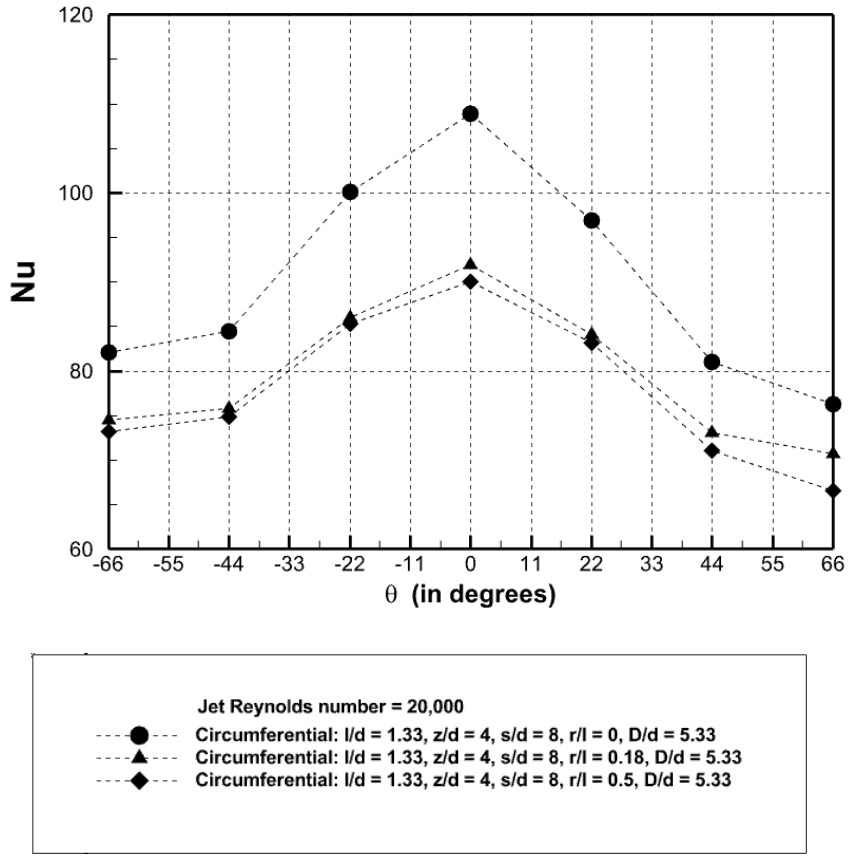

Figure 5.18: Nusselt number variation with jet edge fillet radius in circumferential direction

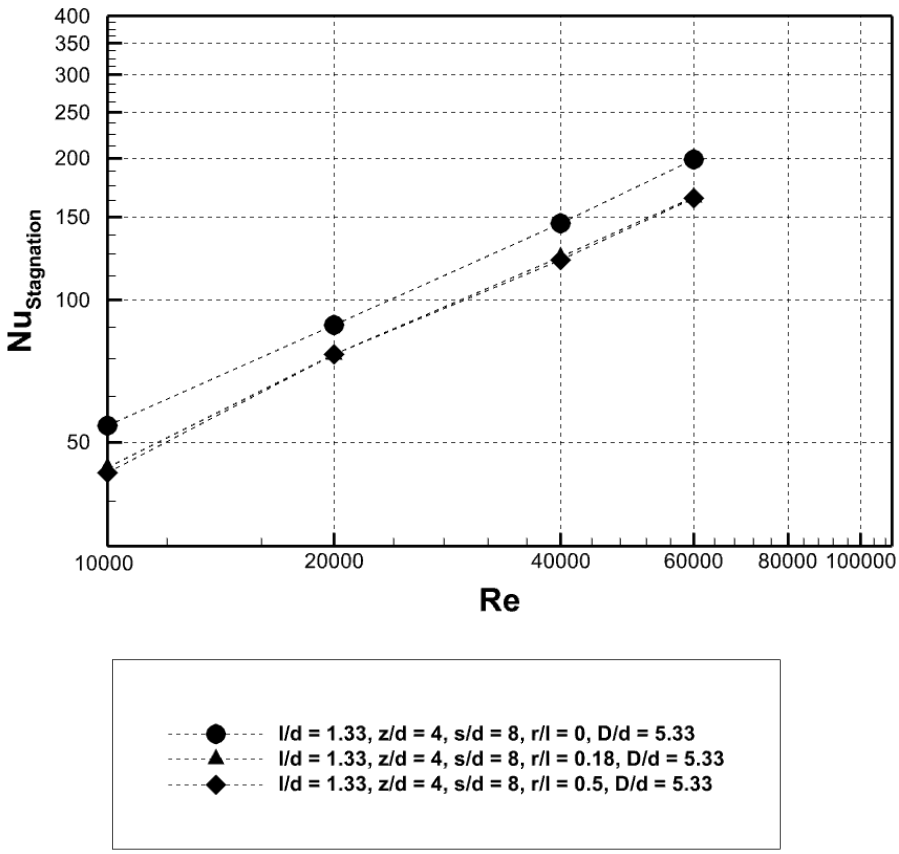

Figure 5.19: Stagnation Nusselt number variation with Reynolds number and jet edge filet radius

Pressure Losses

As heat transfer and fluid dynamics are intertwined, heat transfer studies are often accompanied with the flow details. Quantifying pressure losses incurred across the jet is essential to understanding the heat transfer trends and managing the performance of the cooling configuration. The losses are presented as direct pressure differences or as non-dimensional ratios of loss coefficients and discharge coefficients. A higher pressure difference implies higher pressure losses, higher loss coefficients and lower discharge coefficients. In this study, the pressure losses are presented as discharge coefficients. The following section discusses the parametric effects of flow and geometry on the discharge coefficients.

Effect of Jet-to-Jet Spacing

Figure 5.20 presents the discharge coefficient variation with Reynolds number and jet-to-jet spacing. From the plot, the discharge coefficients improve as the spacing increases. The discharge coefficients are more sensitive to jet-to-jet spacing at high Reynolds numbers. The larger spacings allow spent air to exit, and it does not interact with other jets. It also reduces the flow resistance and friction, leading to reduced losses.

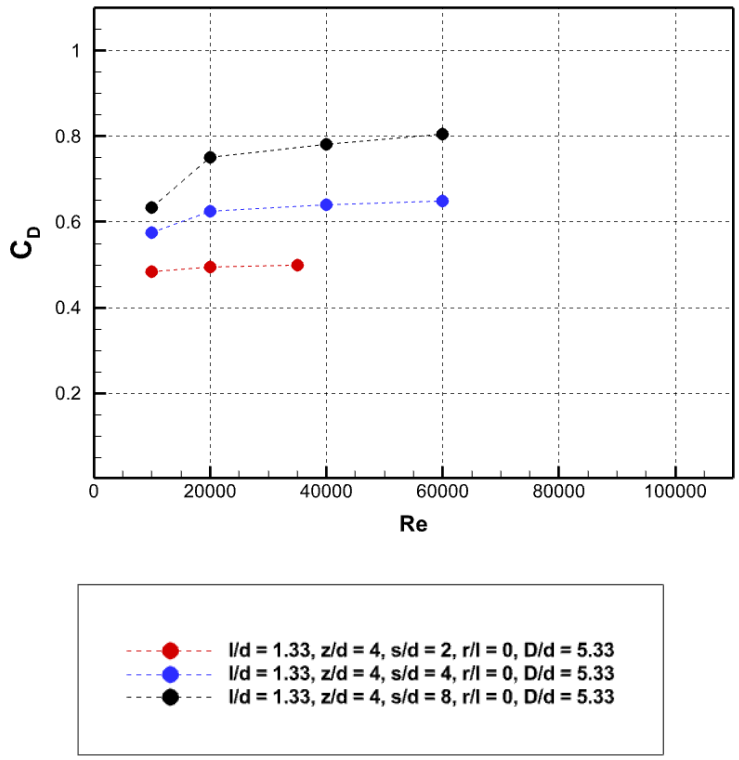

Figure 5.20: Discharge coefficient variation with Reynolds number and jet-to-jet spacing

Effect of Jet-to-Target Surface Spacing

The effect of jet-to-target surface spacing on the discharge coefficients has been shown to be inversely proportional. Figure 5.21 presents the discharge coefficient variation with Reynolds number and jet-to-target surface spacing. From the figure, the discharge coefficients increase marginally with Reynolds number. It seems that the pressure loss increases as the spacing decreases, which goes in accordance with pressure studies. This is attributed to direct transition of the impingement jets to wall jets. In addition, due to reduced volume, the wall jets face shear stresses from the impingement and target surface, thus increasing the losses. It is important to remember that there is also a reduction in the curvature from 5.33 to 2.665 jet diameters. Perhaps the smaller curvature provides less space for the spent air to exit, thereby affecting other jets and

increasing the internal resistance. A coupled effect of smaller jet-to-target surface spacing and smaller curvature decreases the discharge coefficients significantly by 50%. Despite the great intensity of mixing leading to increased heat transfer, the pressure losses need to be taken into account.

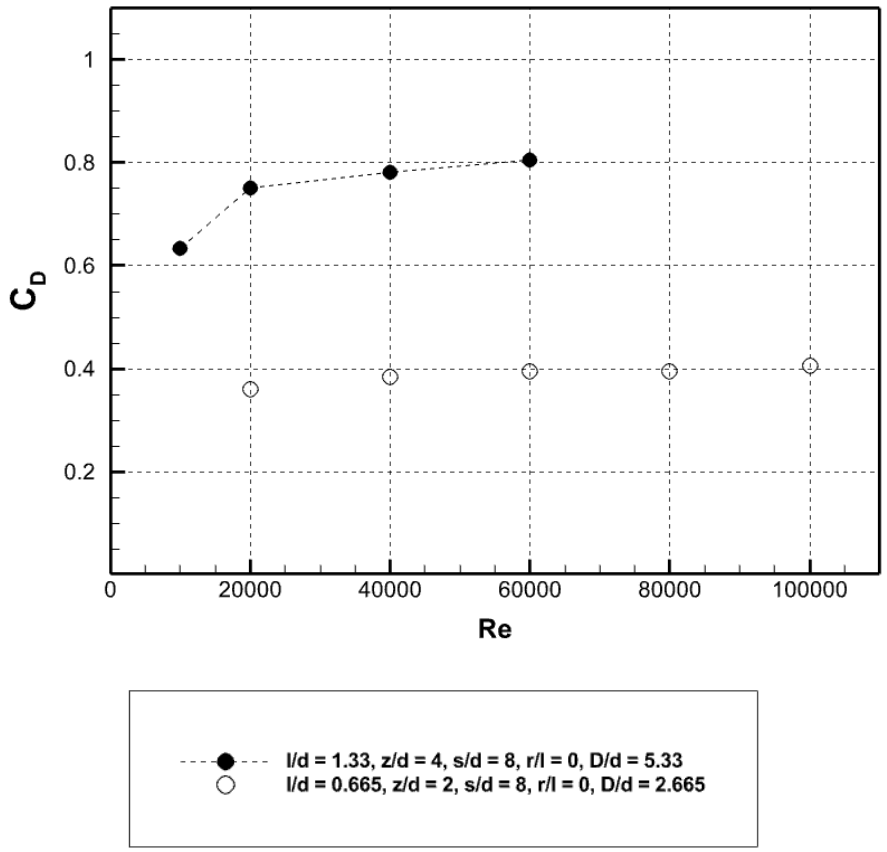

Figure 5.21: Discharge coefficient variation with Reynolds number and jet-to-target surface spacing

Effect of Jet Nozzle Length (Jet Plate Thickness)

The jet nozzle length (jet plate thickness) plays a pivotal role in reducing the pressure losses. As discussed from pressure investigation, the jet nozzle length (jet plate thickness) alters the flow development and structure at the orifice outlet. Figure 5.22 presents the discharge coefficient variation with Reynolds number and jet nozzle length (jet plate thickness). The coefficients increase with Reynolds number. The trends seem interesting as extreme jet nozzle lengths (1.33 diameters and 4 diameters) have the lowest discharge coefficients, while the intermediate length has a greater value. The smaller value for the jet nozzle length (jet plate thickness) of 1.33 diameters is due to the flow separation and increased jet velocity from the narrow constriction, which increases the pressure drop across the jet length. Thus, the increased turbulence is at the cost of increased pressure loss. However, the larger value for the jet nozzle length (jet plate thickness) of 4 diameters is analogous to the pressure drop across a pipe. The nozzle length of 4 diameters is shorter than the developed length of 10 diameters in pipe flow. Thus, the flow is still developing across the nozzle and has more instabilities, thereby incurring higher pressure drop across the length. Coupled with heat transfer results, the thinner jet plate provided the highest heat transfer while others had a negligible difference amongst them. The tradeoff between the configurations lies between meeting the objectives of improved heat transfer and discharge coefficients. This is met for the jet nozzle length (jet plate thickness) of 2.6 diameters and further supports the previous conclusion of an optimized length to minimize system mass.

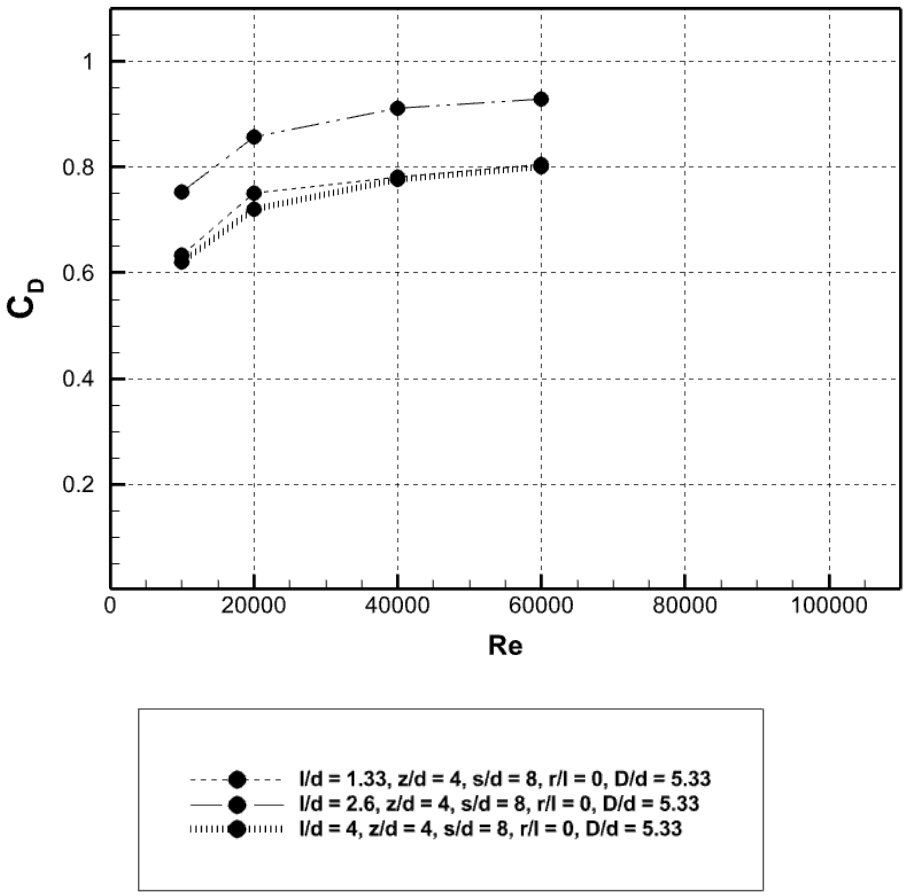

Figure 5.22: Discharge coefficient variation with Reynolds number and jet nozzle length (jet plate thickness)

Effect of Jet Orifice Edge Condition

Stemming from the discrepancies in the conventional experiment setup versus real scenarios in engines, understanding the contribution of inlet and outlet radii on the objectives is essential. Figure 5.23 presents discharge coefficient variation with Reynolds number and fillet radius ratio. The increase of coefficients with Reynolds number is evident. The addition of fillets helps to improve the discharge coefficients by 15%, while the degree of filleting does not provide significant differences. At lower Reynolds numbers, the differences between the fillet radius matters but the effect is reduced as the Reynolds number increases. The increase in discharge coefficients with filleting is due to the reduced flow separation, leading to negligible constriction and thereby lower pressure losses.

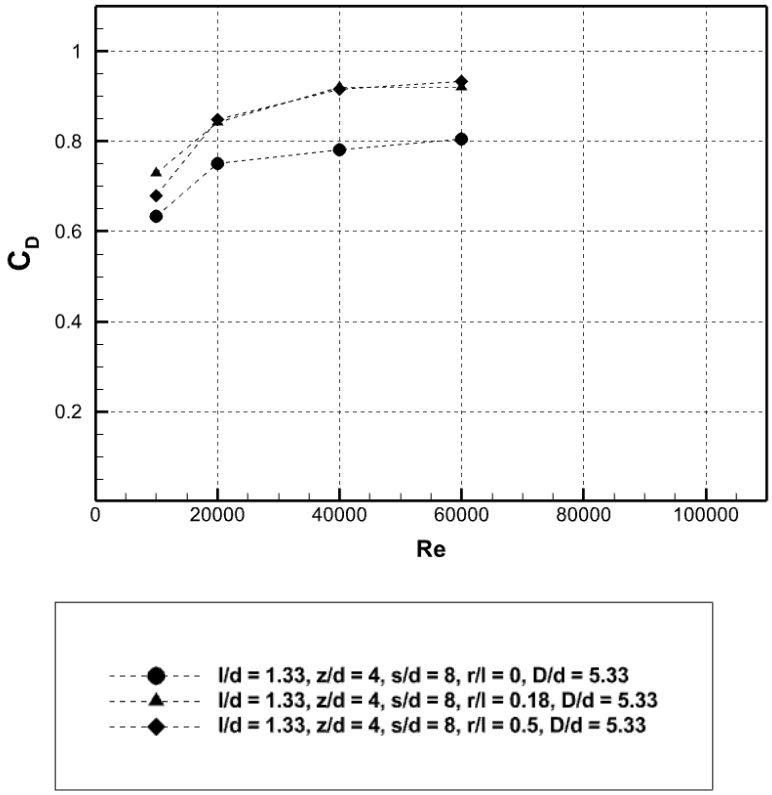

Figure 5.23: Discharge coefficient variation with Reynolds number and fillet radius ratio

Summary

A summary of the Nusselt number and discharge coefficients for 95 experiments are presented in figure 5.24. From the figure, it is seen that the Nusselt number and discharge coefficients do not only depend on Reynolds number. The geometric configuration is essential to estimate the surface Nusselt number. In these experiments, the jet-to-jet spacing (s/d) is 2, 4, 8, jet-to-target surface spacing (z/d) is 2, 4, jet nozzle length (jet plate thickness) (l/d) is 1.33, 2.6, 4, surface curvature-to-jet size (D/d) is 2.665, 5.33 and fillet radius ratio (r/l) is 0, 0.16, 0.18, 0.26 and 0.5. Due to significant effects of geometric parameters, the next step in the present study is to capture the trends quantitatively. The industrial designers benefit from correlations for heat transfer and pressure losses, which provide close estimates in the design stage of industrial projects. The correlations would be able to accurately predict the objectives for a wider range of parameters. The development of these correlations is discussed in detail in the next chapter.

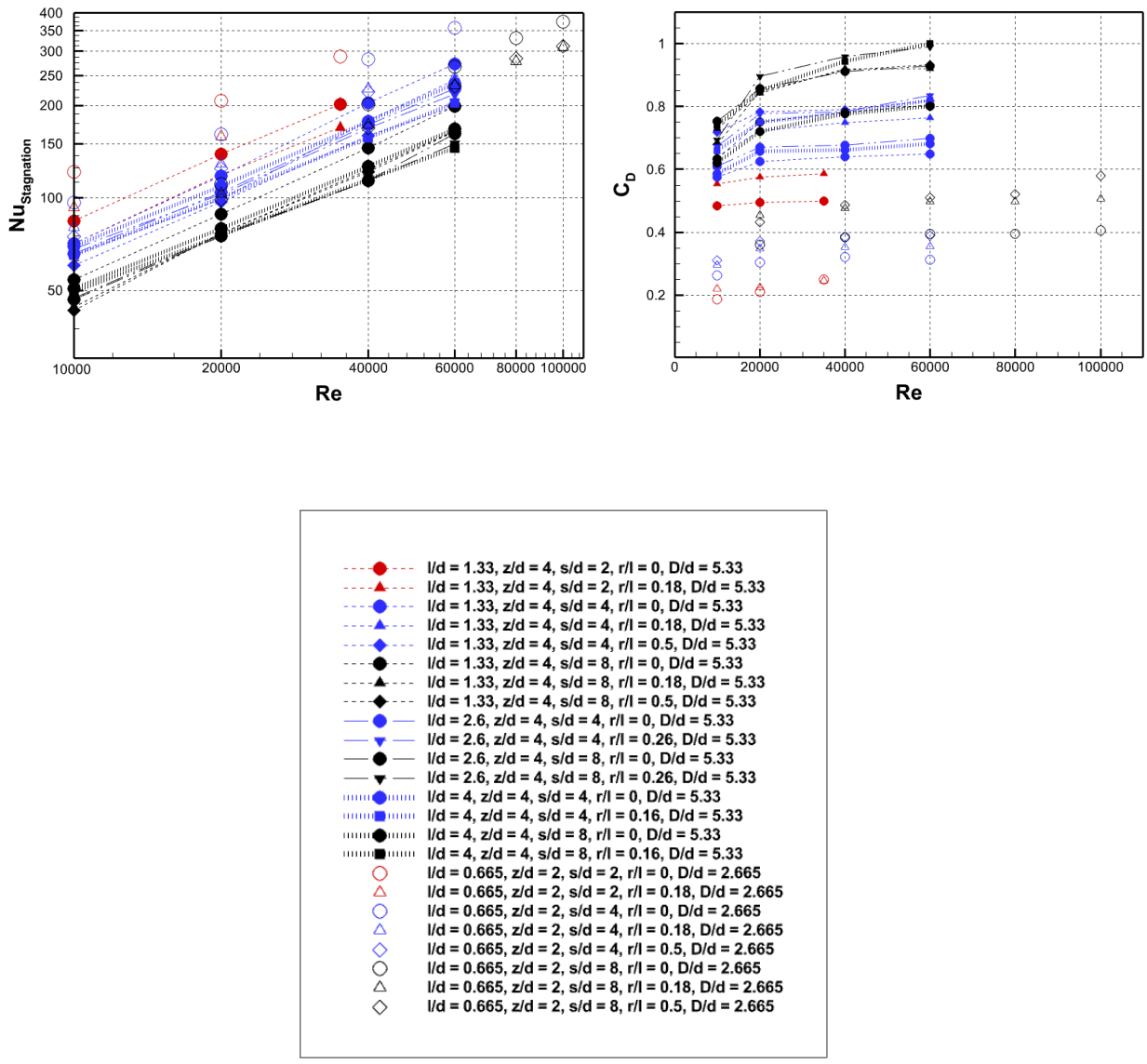

Figure 5.24: (top) Nusselt number variation with Reynolds number and

(bottom) Discharge coefficient variation with Reynolds number for all experimental conditions

CHAPTER VI

CORRELATION OF EXPERIMENTAL RESULTS

This chapter discusses the development of correlations for the average stagnation region Nusselt number and discharge coefficients. The correlations are meant to provide heat transfer estimates for industrial blade designers. In addition, the correlations can also be deployed to identify the potential heat transfer optimums for various combinations of geometric designs.

Motivation and need

Heat transfer models of gas turbine blade designs are used to estimate the blade temperatures. For carrying out the calculations, estimating the heat flux is essential and the temperatures are calculated using the equation 6.1:

$$h = \frac{q''_w}{T_w - T_{reference}} \quad \textbf{(6.1)}$$

Where h is the heat transfer coefficient, q_w" is the heat flux to the surface, T_w is the wall temperature and $T_{reference}$ is the reference temperature, either being outer gas temperature (T_g) or coolant temperature (T_c). From the Nusselt number and geometric properties, the heat transfer coefficient is obtained and the blade temperatures are computed. These Nusselt numbers are obtained from the correlations, which are dependent on many factors. From Chupp et al. [23], the Nusselt number for round holes is dependent on the factors presented in equation 6.2:

$$Nu = f\left(Re, \frac{s}{d}, \frac{z}{d}, \frac{D}{d}\right) \quad \textbf{(6.2)}$$

The correlation for the stagnation Nusselt number is presented in equation 2.1 and represented in equation in 6.3. The correlation is widely used in industry to estimate heat transfer.

$$Nu_{stagnation} = 0.44 \cdot Re^{0.7} \cdot \left(\frac{d}{s}\right)^{0.8} \cdot \exp\left[-0.85 \cdot \left(\frac{z}{d}\right) \cdot \left(\frac{d}{s}\right) \cdot \left(\frac{d}{D}\right)^{0.4}\right] \quad \textbf{(6.3)}$$

From the studies of Harmon et al. [44, 45], Jordan et al. [25-27] and the experimental investigation of this study, it is becoming clear that the current correlation needs revision to match current flow and geometry constraints. The addition of fillets at the jet edge and jet length (jet plate thickness) factors contribute significantly to the leading edge heat transfer and need to be taken into account. The study of pressure losses provide comprehensive understanding for the heat transfer trends, and it is also necessary to quantify them. The pressure losses depend on the geometric configuration and a similar correlation is necessary. There are very few studies that focus on the measuring the loss trends, and this study provides pressure loss correlations amongst the 95 experimental conditions.

The correlation needs to be checked for the accuracy based on the experiment results in this study. Figure 6.1 presents a plot where the experimental results are compared with the correlation estimations from Chupp et al. [23]. For the correlations to be precise, the points need to lie on or close to the line y = x. This nature of this plot is useful for testing correlations. Significant deviations from this line indicates the absence of parameters in the equation or the correlation does not accurately represent the data. From figure 6.1, it is observed that there are significant deviations from the theory, which indicates the correlation ([23]) is missing some parameters. The detailed deviation analysis is carried out in table 6.1.

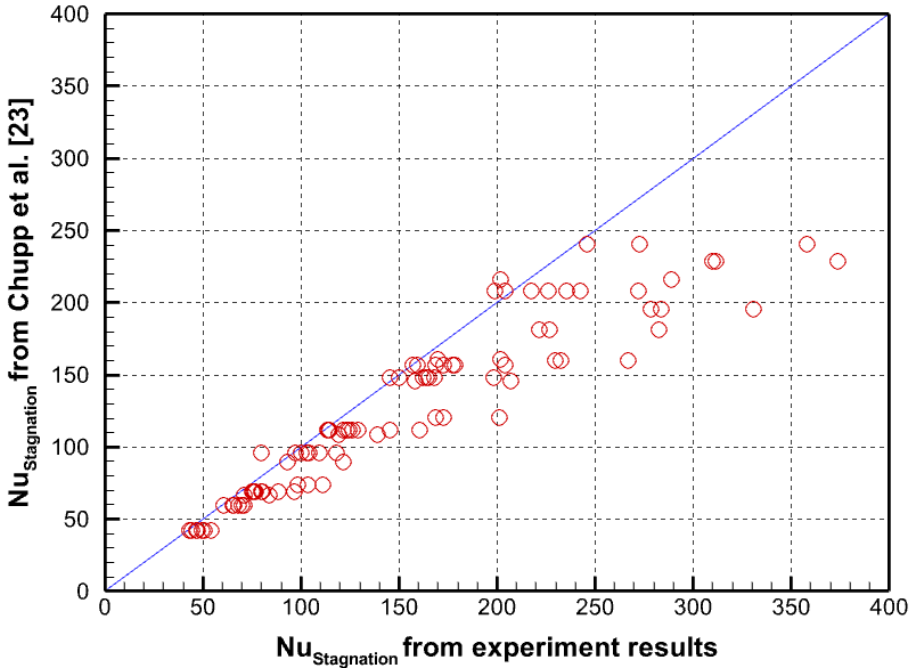

Figure 6.1: Comparison of stagnation Nusselt number between the current experimental results and the correlation predictions [23]

Table 6.1: Deviation analysis of the Chupp et al. [23] correlation

Correlation Equation	Total number of test cases	Test cases with deviation within 0-10%	Test cases with deviation within 11-20%	Test cases with deviation within 21-30%	Test cases with deviation beyond 30%	Maximum deviation (in %)
6.4	95	66	18	1	10	41

The correlation presented by Chupp et al. [23] captured the heat transfer variation with Reynolds number for leading edge jet impingement with round holes and presented it mathematically by:

$$Nu_{stagnation} = A \cdot Re_{jet}^{m} \quad \textbf{(6.4)}$$

Where A and m are the leading coefficient and exponent, respectively. The values of A and m depend on the geometry of the jet. Comparing equation 6.5 with 6.4, the leading coefficient equals:

$$A = 0.44 \cdot \left(\frac{d}{s}\right)^{0.8} \cdot \exp\left[-0.85 \cdot \left(\frac{z}{d}\right) \cdot \left(\frac{d}{s}\right) \cdot \left(\frac{d}{D}\right)^{0.4}\right] \quad \textbf{(6.5)}$$

and the exponent being m = 0.7.

The current study aims to expand the set by developing new correlations for the heat transfer and discharge coefficients for racetrack shaped jets. The correlations would be comprised of the following parameters: jet-to-jet spacing (s/d), jet-to-target surface spacing (z/d), surface curvature-to-jet size (D/d), jet nozzle length (jet plate thickness) (l/d) and fillet radius to jet plate thickness ratio (r/l). From figure 6.2, apart from Nusselt number varying exponentially with Reynolds number, the spread of data is attributed to the varying geometric configurations. The base correlation is expected to be similar to equation 6.4 and will include additional parameters, to eventually have a correlation that would be applicable to modern blade designs.

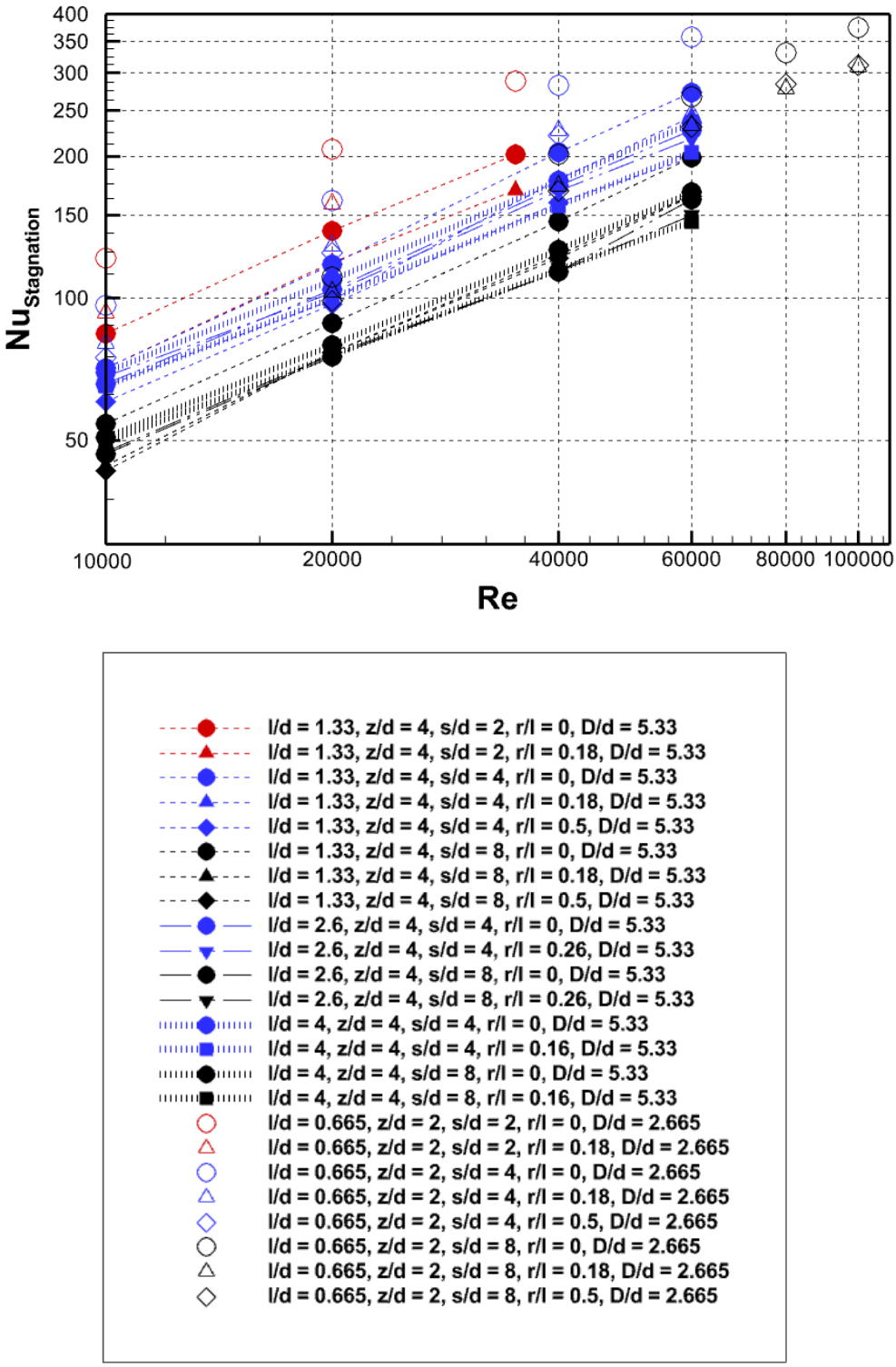

Figure 6.2: Average stagnation region Nusselt number variation with Reynolds number

Development of the Correlations

Heat Transfer

In this section, the development of the correlation will be carried out for both heat transfer and discharge coefficients, and these terms will be referred to as objectives. The objectives are seen to be dependent on geometrical parameter ands flow conditions. This necessitates the need for capturing the trends for every parameter individually. For example, for the parameter of jet-to-jet spacing (s/d), figure 6.3 presents three trend equations for s/d = 2, 4 and 8. The leading coefficients and exponents for these equations are further plotted to obtain a parametric equation, containing the term of s/d.

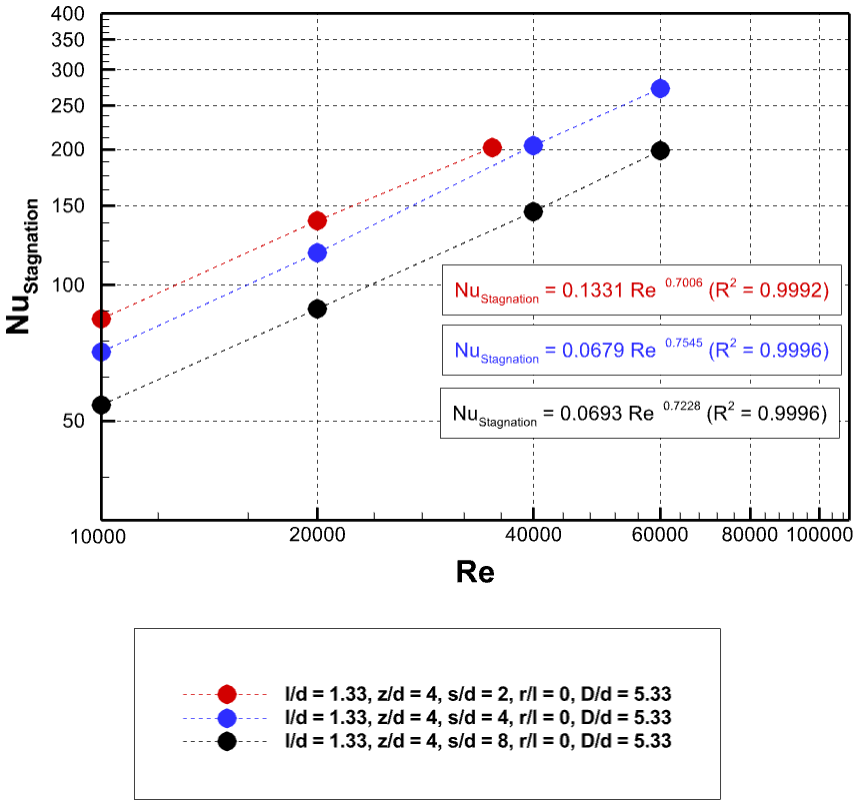

Figure 6.3: Trend equations for stagnation Nusselt number with jet-to-jet spacing and Reynolds number

Equation 6.6 presents the parametric equation for s/d. The data used to obtain equation 6.7 is with a fixed jet configuration of fillet radius of 0, jet nozzle length (jet plate thickness) of 1.33 diameters, jet-to-target surface spacing of 4 diameters and curvature of 5.33 diameters.

$$Nu = 0.1643 * \left(\frac{S}{d}\right)^{-0.471} * Re^{0.7033*\left(\frac{S}{d}\right)^{0.0225}} \quad \textbf{(6.6)}$$

Different sets of parameters would provide different values of the constants. The important takeaway from this discussion is not the values of the constants, rather the nature of equations for the parameter. If compared to equation 6.5, the leading coefficient and exponent are:

$$A = 0.1643 * \left(\frac{s}{d}\right)^{-0.471} \quad \textbf{(6.7)}$$

$$m = 0.7033 * \left(\frac{s}{d}\right)^{0.0225} \quad \textbf{(6.8)}$$

From equations 6.7 and 6.8, it is evident that the leading coefficient and exponent are dependent on the jet-to-jet spacing. Similar individual trend equations are developed for every parameter and a skeleton of the final equation is established (equation 6.9), with all a_i where i = 0 to 12 are the constants.

$$Nu = a_1 \left(\frac{s}{d}\right)^{a_2} \left(\frac{l}{d}\right)^{a_3} \left(\frac{z}{d}\right)^{a_4} \left(\frac{D}{d}\right)^{a_5} \left(e^{a_6 * \frac{r}{l}}\right) Re^{\left[a_7 \left(\frac{s}{d}\right)^{a_8} \left(\frac{l}{d}\right)^{a_9} \left(\frac{z}{d}\right)^{a_{10}} \left(\frac{D}{d}\right)^{a_{11}} \left(e^{a_{12} * \frac{r}{l}}\right)\right]} \quad \textbf{(6.9)}$$

Nonlinear regression is carried out over equation 6.9 to obtain the values of the constants. Before moving to the final correlation, there is a need to discuss the final development of the correlation. As shown in the previous sections, the effects of curvature-to-jet size (D/d) is coupled with the effect of changing jet diameter. This also makes the parametric levels binary – with two values of D/d due to two values of diameters. As in the test cases, the configuration with d = 0.953 cm also has D/d = 5.33, while the configuration of d = 1.906 cm, has D/d = 2.665. Due to the binary effect, the continuous correlation seems to have significant deviations from the experiment results. Moreover, from the results, it is evident that both heat transfer and pressure loss depend on the presence of the fillet and are less sensitive to the degree of filleting. Hence, the correlations are developed as two separate entities, one for square edged jet orifice (r/l = 0) and another for presence of fillets (r/l = 0.16-0.5). The correlations for heat transfer are presented in equations 6.10 and 6.11. Due to the coupled effect for D/d due to two diameters, the term D/d naturally does not appear in the equation.

$$Nu = 0.0483 \cdot \left(\frac{s}{d}\right)^{0.0536} \cdot \left(\frac{l}{d}\right)^{-0.9893} \cdot \left(\frac{z}{d}\right)^{0.7422} \cdot Re^{\left[0.8945 \cdot \left(\frac{s}{d}\right)^{-0.0558} \cdot \left(\frac{l}{d}\right)^{0.1116} \cdot \left(\frac{z}{d}\right)^{-0.1411}\right]} \quad \textbf{(6.10)}$$

$for\ 10{,}000 \leq Re \leq 100{,}000, \quad 2 \leq \frac{z}{d} \leq 4, \quad 2 \leq \frac{s}{d} \leq 8, \quad 0.665 \leq \frac{l}{d} \leq 4, \quad \frac{r}{l} = 0, \quad \frac{D}{d} = 2.665 - 5.33$

$$Nu = 3.124 \cdot \left(\frac{s}{d}\right)^{-0.035} \cdot \left(\frac{l}{d}\right)^{1.2294} \cdot \left(\frac{z}{d}\right)^{-3.4152} \cdot Re^{\left[0.4876 \cdot \left(\frac{s}{d}\right)^{-0.0306} \cdot \left(\frac{l}{d}\right)^{-0.173} \cdot \left(\frac{z}{d}\right)^{0.4158}\right]} \quad \textbf{(6.11)}$$

$for\ 10{,}000 \leq Re \leq 100{,}000, \quad 2 \leq \frac{z}{d} \leq 4, \quad 2 \leq \frac{s}{d} \leq 8, \quad 0.665 \leq \frac{l}{d} \leq 4, \quad \frac{r}{l} = 0.16 - 0.5, \quad \frac{D}{d} = 2.665 - 5.33$

The accuracy of the correlation is presented in figure 6.4, a similar plot to figure 6.1. From the plots, the majority of the data seem to lie closer the line y = x. This demonstrates the accuracy of the correlations in predicting the heat transfer in the specific domains. Table 6.2 provides an analysis of the deviations observed in both plots. For equation 6.11, the correlation is able to account for 90% of the test cases within 0-10% deviation and 10% test cases in 11-20% deviation. For equation 6.10, the correlation is able to account 86% of the test cases within 0-10% deviation and 14% test cases in 11-20% deviation.

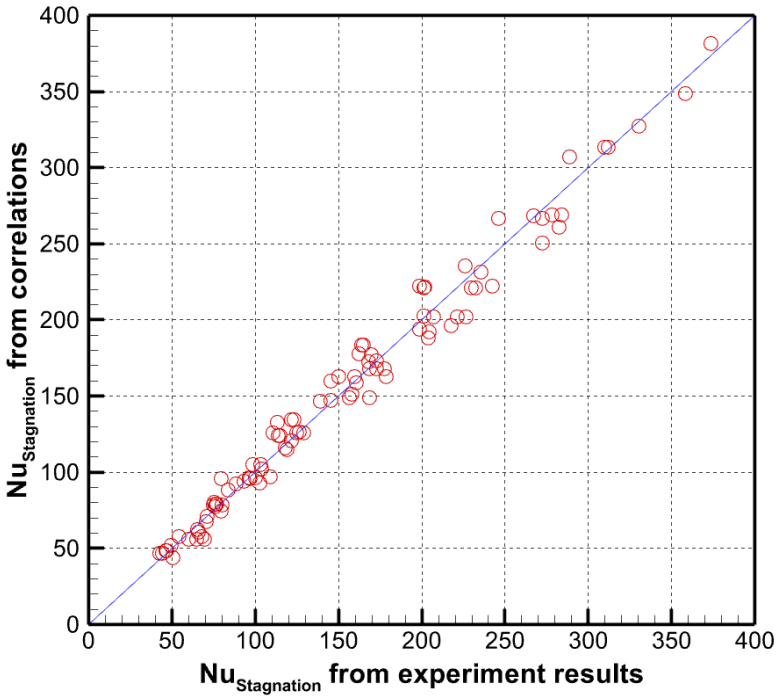

Figure 6.4: Comparison between the experimental data and predictions from the two correlations (equations 6.10 and 6.11)

Table 6.2: Deviation analysis of the heat transfer correlations (equations 6.10 and 6.11)

Correlation Equation	Total number of test cases	Test cases with deviation within 0-10%	Test cases with deviation within 11-20%	Test cases with deviation within 21-30%	Maximum deviation (in %)
6.10	39	35	4	0	19.8
6.11	56	48	8	0	18.7

From the correlation and the constants, it is essential to derive the behavior for every parameter. All the geometric parameters appear in both the leading coefficient and exponent. The jet-to-jet spacing has a negative exponent for the heat transfer, which presents an inversely proportional trend. The nozzle length has a dominating negative exponent in Reynolds number, conveying a decreasing heat transfer trend. The jet-to-target surface spacing has a positive

exponent, leading to increased heat transfer. Comparing the squared-edged and filleted jets, it is interesting to observe the heat transfer variation with jet plate thickness. For the square-edged jets, the Nusselt number is relatively insensitive to the jet plate thickness. However, for the filleted jets, the Nusselt number is highest for thickest plate. Increasing the thickness counteracts the fillet and straightens the jet so it effectively strikes the target surface.

An equation has also been developed which comprises of all the parameters except for D/d. However, the deviation is as high as 26.3% with 77% cases within 0-10% deviation range, 15% cases in the 11-20% deviation and 8% cases in 21-30% deviation. The correlation is presented in equation 6.12. The spread is presented in figure 6.5 and table 6.3.

$$Nu = 0.2866 \cdot \left(\frac{s}{d}\right)^{-0.0975} \cdot \left(\frac{l}{d}\right)^{-0.6701} \cdot \left(\frac{z}{d}\right)^{-0.0366} \cdot \left(e^{-5.1701*\frac{r}{l}}\right) \cdot Re^{\left[0.6962 \cdot \left(\frac{s}{d}\right)^{-0.03} \cdot \left(\frac{l}{d}\right)^{0.077} \cdot \left(\frac{z}{d}\right)^{-0.0381} \cdot \left(e^{0.5982*\frac{r}{l}}\right)\right]} \quad \textbf{(6.12)}$$

$$for\ 10{,}000 \leq Re \leq 100{,}000, \quad 2 \leq \frac{z}{d} \leq 4, \quad 2 \leq \frac{s}{d} \leq 8, \quad 0.665 \leq \frac{l}{d} \leq 4, \quad \frac{r}{l} = 0 - 0.5, \quad \frac{D}{d} = 2.665 - 5.33$$

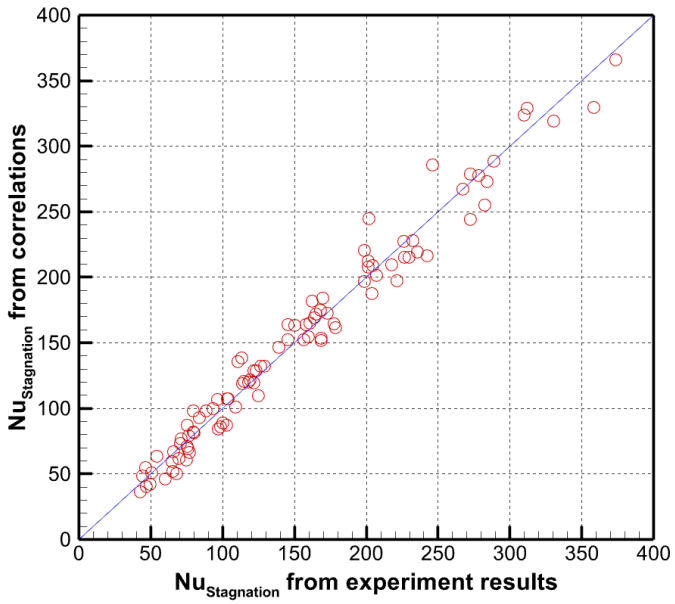

Figure 6.5: Comparison between the experimental data and predictions from the correlation (equation 6.12)

Table 6.3: Deviation analysis of the heat transfer correlation (equation 6.12)

Correlation Equation	Total number of test cases	Test cases with deviation within 0-10%	Test cases with deviation within 11-20%	Test cases with deviation within 21-30%	Maximum deviation (in %)
6.10	95	74	15	6	26.3

Pressure Loss

A similar strategy is employed to obtain the correlations for the discharge coefficients. The variation of discharge coefficients with Reynolds number is increasing and both logarithm and power form were ideal fits to describe this trend. However, as the Reynolds number approached zero, the discharge coefficients would too be closer to zero and hence the power form was chosen. The power form is similar to equation 6.5. Individual parametric trends were obtained and the skeletal version of the final equation was obtained, as in equation 6.13, with all a_i where i = 0 to 12 are the constants]

$$C_D = a_1 \left(\frac{s}{d}\right)^{a_2} \left(\frac{l}{d}\right)^{a_3} \left(\frac{z}{d}\right)^{a_4} \left(\frac{D}{d}\right)^{a_5} \left(e^{a_6 * \frac{r}{l}}\right) Re^{\left[a_7 \left(\frac{s}{d}\right)^{a_8} \left(\frac{l}{d}\right)^{a_9} \left(\frac{z}{d}\right)^{a_{10}} \left(\frac{D}{d}\right)^{a_{11}} \left(e^{a_{12} * \frac{r}{l}}\right)\right]} \quad \textbf{(6.13)}$$

The experimental data was curve fitted to obtain the value of the coefficients. Similar to the development of the heat transfer correlations, the equations were developed separately for the sets – squared edged jet orifice (r/l = 0) and with fillets (r/l = 0.16-0.5). The correlations are presented in the equations 6.14 and 6.15:

$$C_D = 0.0392 \cdot \left(\frac{S}{d}\right)^{0.1165} \cdot \left(\frac{l}{d}\right)^{0.0607} \cdot \left(\frac{z}{d}\right)^{1.165} \cdot Re^{\left[0.0844 \cdot \left(\frac{s}{d}\right)^{0.1737} \cdot \left(\frac{l}{d}\right)^{-0.0338} \cdot \left(\frac{z}{d}\right)^{-0.0757}\right]} \quad \textbf{(6.14)}$$

$$for\ 10{,}000 \le Re \le 100{,}000, \quad 2 \le \frac{z}{d} \le 4, \quad 2 \le \frac{s}{d} \le 8, \quad 0.665 \le \frac{l}{d} \le 4, \quad \frac{r}{l} = 0, \quad \frac{D}{d} = 2.665 - 5.33$$

$$C_D = 0.0785 \cdot \left(\frac{S}{d}\right)^{0.6639} \cdot \left(\frac{l}{d}\right)^{-0.0397} \cdot \left(\frac{z}{d}\right)^{-0.1668} \cdot Re^{\left[0.0432 \cdot \left(\frac{s}{d}\right)^{-0.2889} \cdot \left(\frac{l}{d}\right)^{0.0559} \cdot \left(\frac{z}{d}\right)^{1.1772}\right]} \quad \textbf{(6.15)}$$

$$for\ 10{,}000 \le Re \le 100{,}000, \quad 2 \le \frac{z}{d} \le 4, \quad 2 \le \frac{s}{d} \le 8, \quad 0.665 \le \frac{l}{d} \le 4, \quad \frac{r}{l} = 0.16 - 0.5, \quad \frac{D}{d} = 2.665 - 5.33$$

The accuracy of the correlation is presented in figure 6.6. From the plots, it can be seen that the majority of data lie closer the line y = x. This demonstrates the accuracy of the correlations in predicting the heat transfer in the specific domains. Table 6.4 provides an analysis of the deviations observed in both plots. For equation 6.14, the correlation is able to account for 93% of the test cases in the 0-10% deviation and 7% of the test cases in 11-20%. For equation 6.15, the correlation is able to account for 93% of the test cases in the 0-10% deviation and 7% of the test cases within 11-20%.

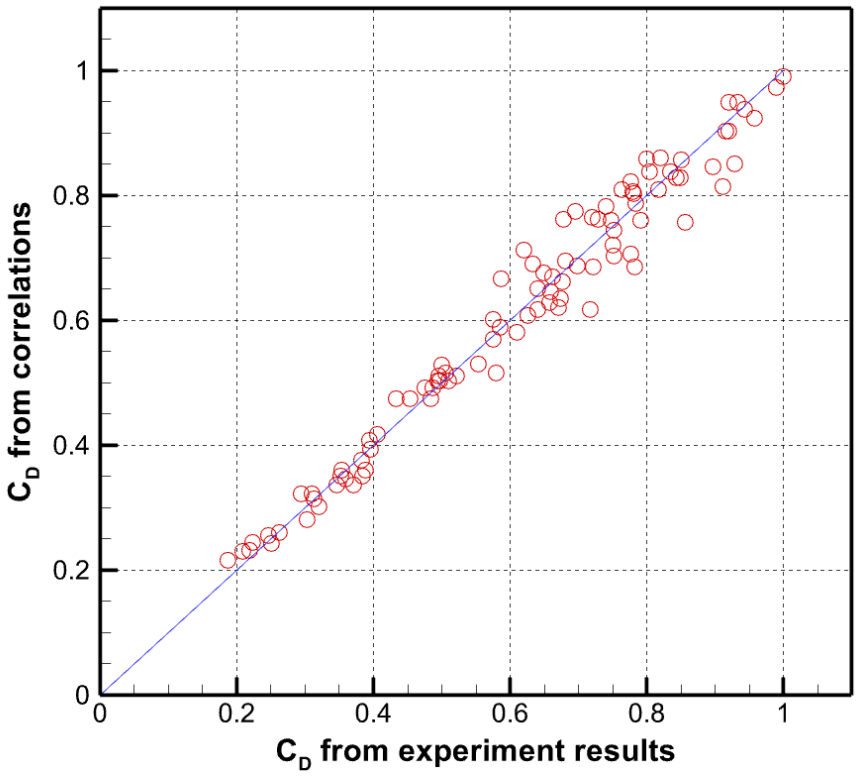

Figure 6.6: Comparison plots between the experimental data and estimations from the two correlations (equations 6.14 and 6.15)

Table 6.4: Deviation analysis of the pressure loss correlations (equations 6.14 and 6.15)

Correlation Equation	Total number of test cases	Test cases with deviation within 0-10%	Test cases with deviation within 11-20%	Test cases with deviation within 21-30%	Maximum deviation (in %)
6.14	39	36	3	0	15.9
6.15	56	52	4	0	13.9

From the correlation and the constants, it is essential to derive the behavior for every parameter. All the geometric parameters appear in both the leading coefficient and exponent. The effect of jet-to-jet spacing depends on the jet-to-target surface spacing, as for smaller spacing, the discharge coefficient increases with the jet-to-jet spacing and the opposite is true for larger

spacings. For smaller z/d, the losses decrease with increasing s/d due to less interactions and reduced resistance. The effect of jet nozzle length (jet plate thickness) is a positive trend for smaller spacings, with the pressure losses reducing with the length. This is due to the jet development and reduced effect of the vena contracta. However, for higher jet-to-target spacings, the increased length decreases the discharge coefficients, which goes in accordance with the experimental results. As discussed in the previous section, this is due to the length adding more pressure loss.

An equation has also been developed which comprises of all the parameters except for D/d. However, the deviation is as high as 19.4% with 84% cases in 0-10% deviation range and 16% cases in the 11-20% deviation. The correlation is presented in equation 6.16, spread presented in figure 6.7 and deviation analysis is reported in table 6.5.

$$C_D = 0.0342 \cdot \left(\frac{s}{d}\right)^{-0.0632} \cdot \left(\frac{l}{d}\right)^{0.1314} \cdot \left(\frac{z}{d}\right)^{1.3251} \cdot \left(e^{0.6099*\frac{r}{l}}\right) \cdot Re^{\left[0.1094 \cdot \left(\frac{s}{d}\right)^{0.2695} \cdot \left(\frac{l}{d}\right)^{-0.0552} \cdot \left(\frac{z}{d}\right)^{-0.2494} \cdot \left(e^{-0.1827*\frac{r}{l}}\right)\right]} \quad \textbf{(6.16)}$$

$$for\ 10{,}000 \leq Re \leq 100{,}000, \quad 2 \leq \frac{z}{d} \leq 4, \quad 2 \leq \frac{s}{d} \leq 8, \quad 0.665 \leq \frac{l}{d} \leq 4, \quad \frac{r}{l} = 0 - 0.5, \quad \frac{D}{d} = 2.665 - 5.33$$

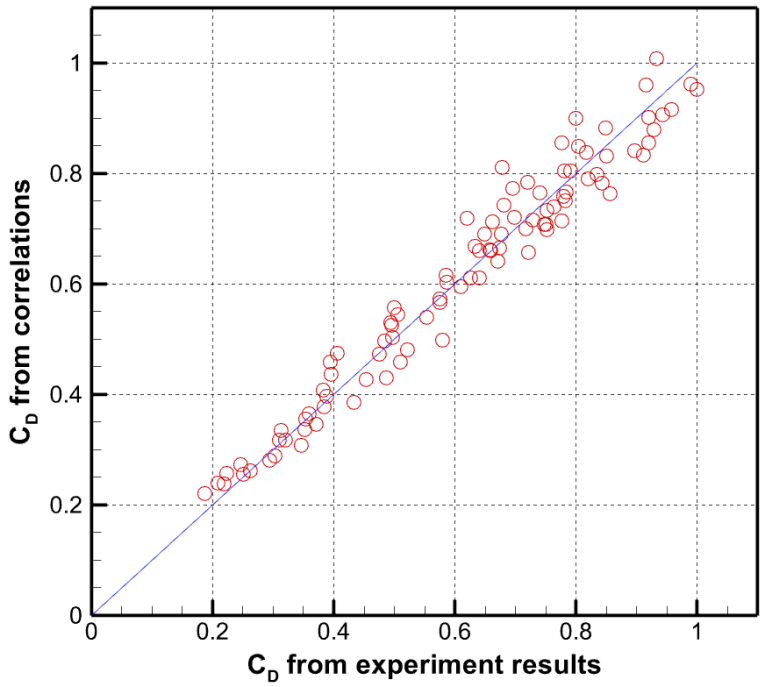

Figure 6.7: Comparison plots between the experimental data and estimations from the correlation (equation 6.16)

Table 6.5: Deviation analysis of the heat transfer correlation (equation 6.16)

Correlation Equation	**Total number of test cases**	**Test cases with deviation within 0-10%**	**Test cases with deviation within 11-20%**	**Test cases with deviation within 21-30%**	**Maximum deviation (in %)**
6.10	95	80	15	0	19.4

Advantages

The correlations empower the industrial blade designers by providing accurate heat transfer and discharge coefficient estimates for a wide range of parametric values. However, the correlations are not limited to estimation only. They can be used to understand the effect of individual parameters by inducing some perturbation and observing the effects. For example, by keeping all the parameters constant and varying only the jet-to-jet spacing or jet-to-target surface spacing to observe the effects on objectives. Such analyses help to understand the general trend of the parameters and also identify the regions where behaviors seem to be novel and interesting. Due to the correlations being more mathematical, designers prefer to have data visualized to allow quick and concise analysis. Four dimensional, contour plots are often used to present data of this nature, where color bars are used to indicate heat transfer values. Figure 6.8 presents the correlation estimations for the stagnation Nusselt number for variations in three parameters: jet-to-jet spacing (s/d), jet-to-target surface spacing (z/d) and jet nozzle length (jet plate thickness) (l/d). The lower range of heat transfer is marked by blue color, the higher ranges are marked by red color and various shades are present for intermediate values. Another advantage of the correlation is the ability to provide multiple jet configurations for a desired stagnation Nusselt number, presented in figure 6.8. This provides the designers options to choose from amongst various parametric combinations for obtaining the same heat transfer values.

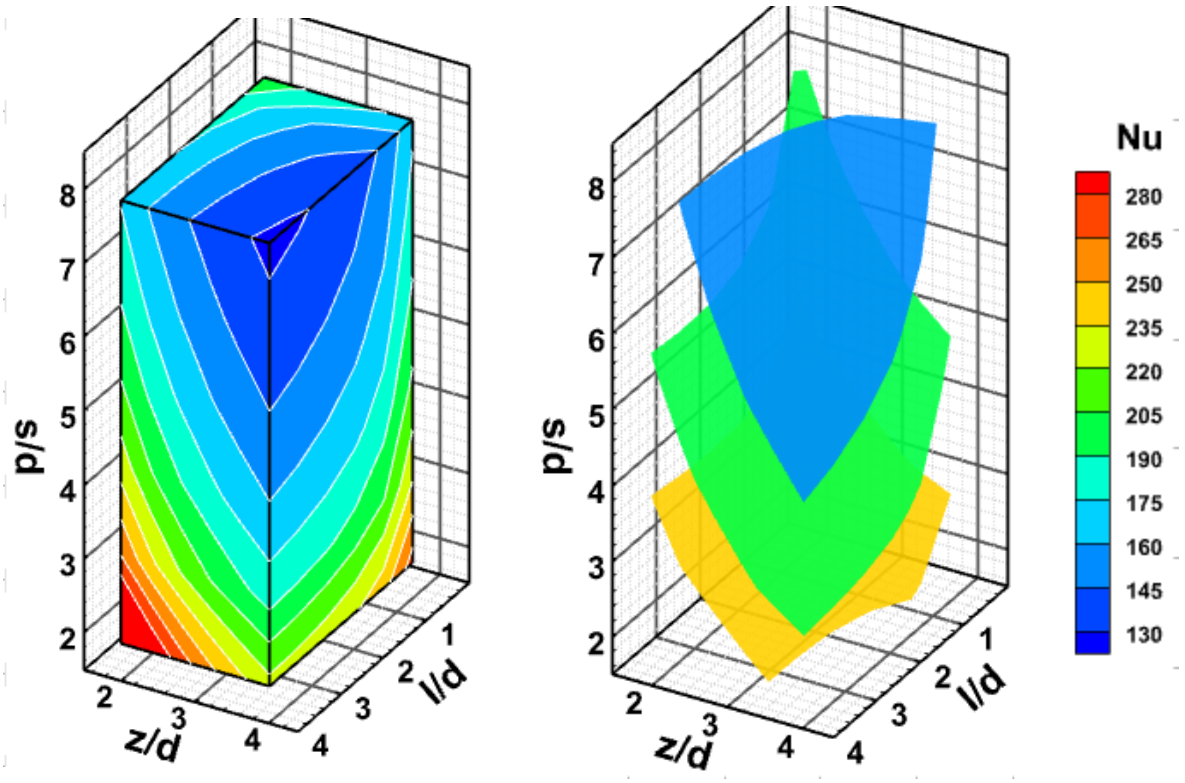

Figure 6.8: (left) 4D Contour plot for stagnation Nusselt number based on equation 6.10 (r/l = 0) (b) Iso-surfaces for stagnation Nusselt numbers of 160 (sky blue), 200 (bright green) and 240 (orange) for Reynolds number of 40,000

In order to visualize the data more accurately with minimum parameters, slices of constant parametric values are presented. Figure 6.9 presents the contour slices for constant jet-to-jet spacings of 2, 4, 6 and 8. In these plots, variations between two parameters: jet-to-target surface spacing and jet nozzle length (jet plate thickness) are present and help to understand their trends. For example, heat transfer is seen to decrease with increasing jet-to-jet spacing as the colors transition from yellow to blue. Also, relatively higher regions of heat transfer are found for small z/d = 2 and shorter jet nozzle length (jet plate thickness) (l/d = 0.665). For a fixed z/d, the effect of l/d is minimal as the contours appear as approximately vertical.

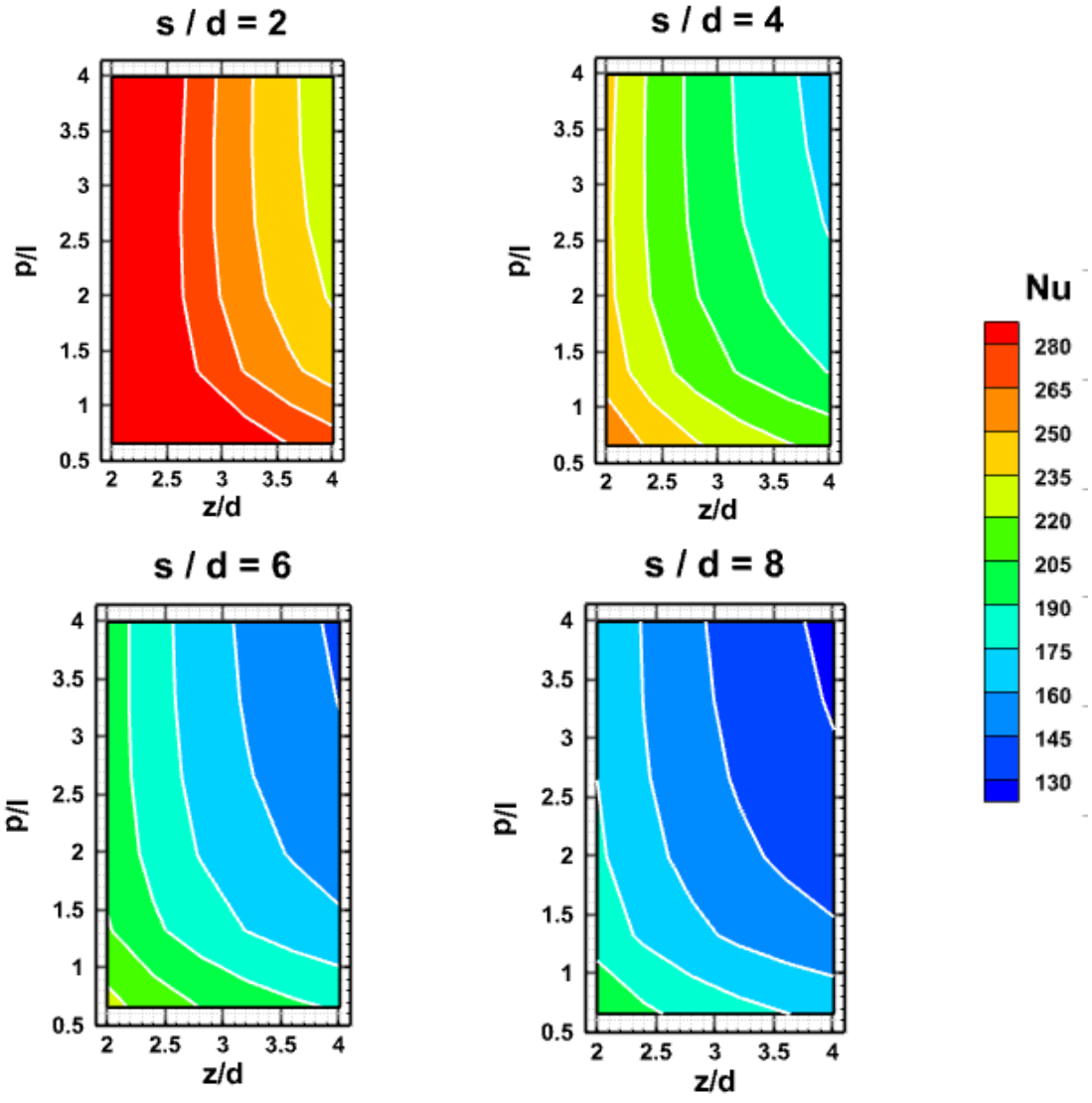

Figure 6.9: 2D contour plots for stagnation Nusselt number based on equation 6.10 (r/l = 0) for constant jet-to-jet spacing and Reynolds number of 40,000

With very few studies providing pressure loss data and no information about correlations, the newly developed correlations help to fill the existing void. In addition, there is a great interest amongst the community to learn about the parametric trends in discharge coefficients. As fluid dynamics and heat transfer are intertwined, information about the discharge coefficients

helps the designers to evaluate the parametric combinations. Figure 6.10 presents the four-dimensional contour plots for discharge coefficients with varying jet-to-jet spacing, jet-to-target surface spacing and jet nozzle length (jet plate thickness). The color differentials help to identify the regions of coefficient extremities. In addition, figure 6.10 also presents iso-surfaces for desired discharge coefficients. Designers can obtain the various combinations and would help to pick the design with optimum values of heat transfer and discharge coefficients.

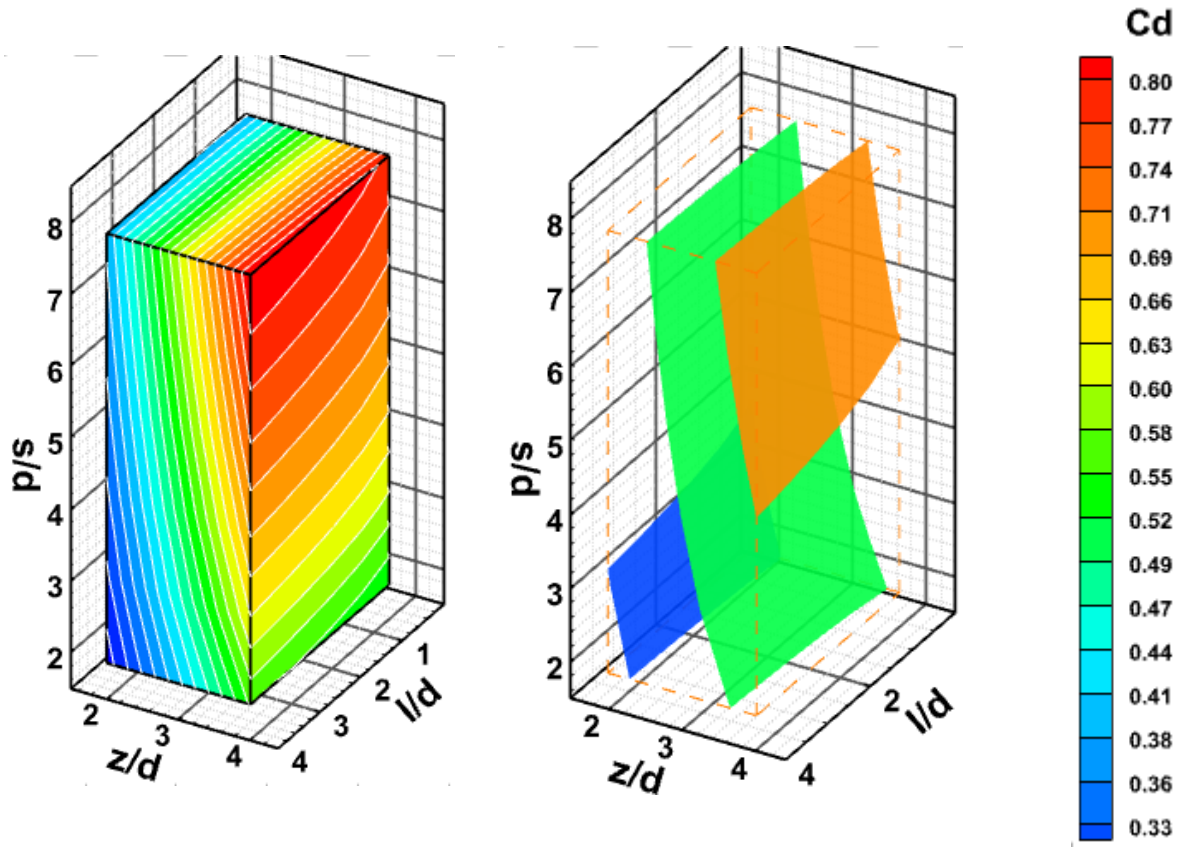

Figure 6.10: (left) 4D Contour plot for discharge coefficients based on equation 6.14 (r/l = 0) (b) Iso-surfaces for discharge coefficients of 0.3 (blue), 0.5 (green) and 0.7 (orange) for Reynolds number of 40,000

To further understand the parametric effects, slices of constant parametric values can be performed. Figure 6.11 present similar plots for constant jet-to-jet spacing of 2, 4, 6 and 8, with varying jet-to-target surface spacing and jet nozzle length (jet plate thickness). Conforming with the results, discharge coefficients improve with increasing jet-to-jet spacing and increasing jet-to-target surface spacing. For the square edged jets there are more vertical contours than horizontal, indicating the dominating effect of z/d over l/d.

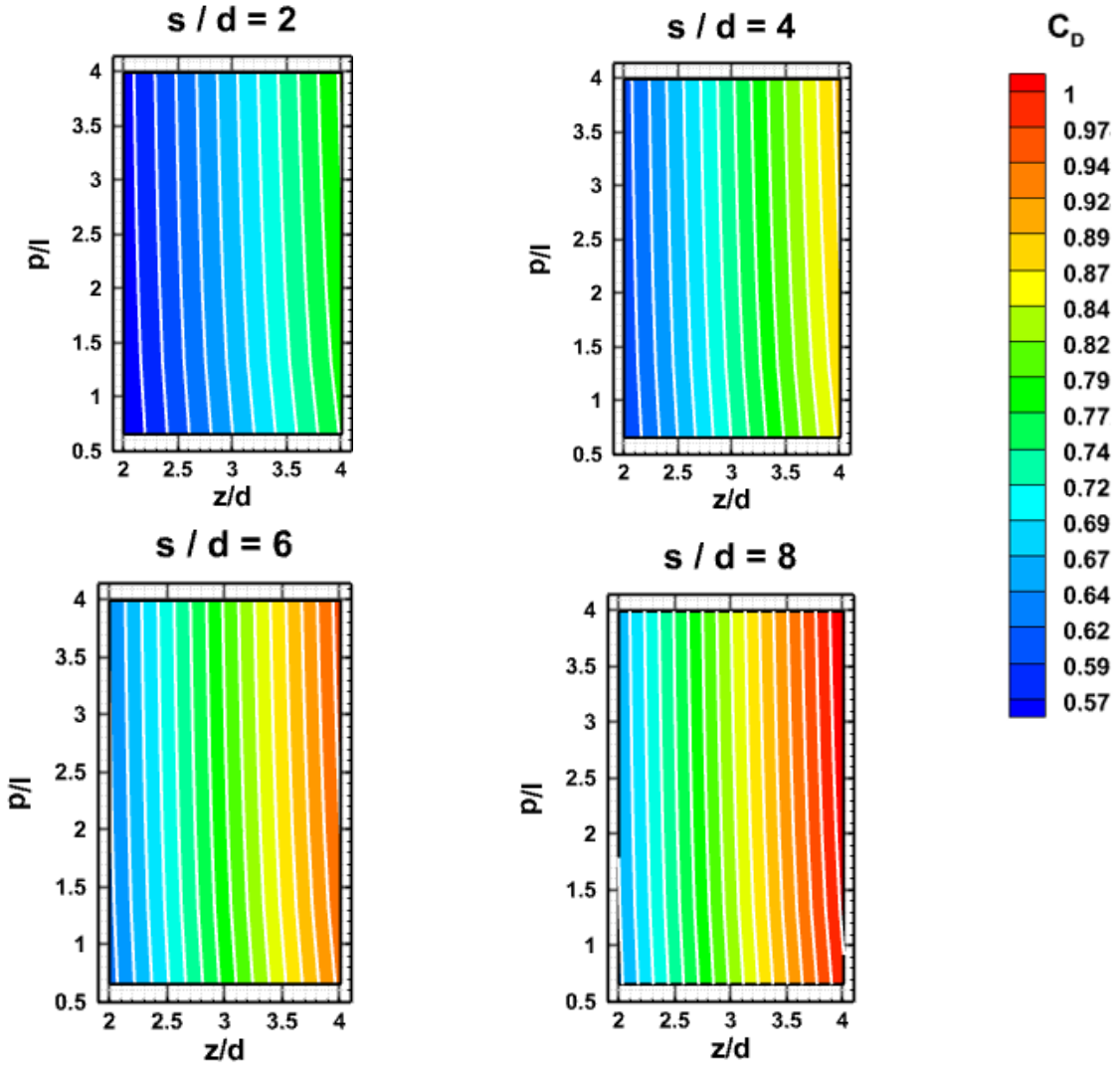

Figure 6.11: 2D contour plots for discharge coefficients based on equation 6.14 (r/l = 0) for constant jet-to-jet spacing and Reynolds number of 40,000

Validation

The correlations discussed from the previous sections have been developed from experiments over specific ranges of parameters. As the correlation projects a decent accuracy with the experimental data, it is essential to check the same with the published data. This makes the correlations more robust and provides opportunities to analyze the areas of high deviations. However, published investigations have different test setups, diverse flow conditions and various jet geometries, that makes the comparison difficult. For a fair comparison, literature pertaining to curved surface jet impingement with racetrack shaped jets are chosen. Figure 6.12 presents the comparison of the published data with the correlation estimates. The computational heat transfer results from Taslim et al. [70] had a considerable presence of crossflow, which reduced the stagnation Nusselt numbers. This might have led to the increased deviation from the correlations, with the deviation being less than 10% in the lower jet Reynolds number. In addition, the jet nozzle length (jet plate thickness) was smaller than the lower limit of the correlation domain, leading to extrapolation. From the experimental results of Harmon et al. [45] and Jordan et al. [26], the data seem to be closer to the correlation estimates as the parametric values fall within the correlation domain.

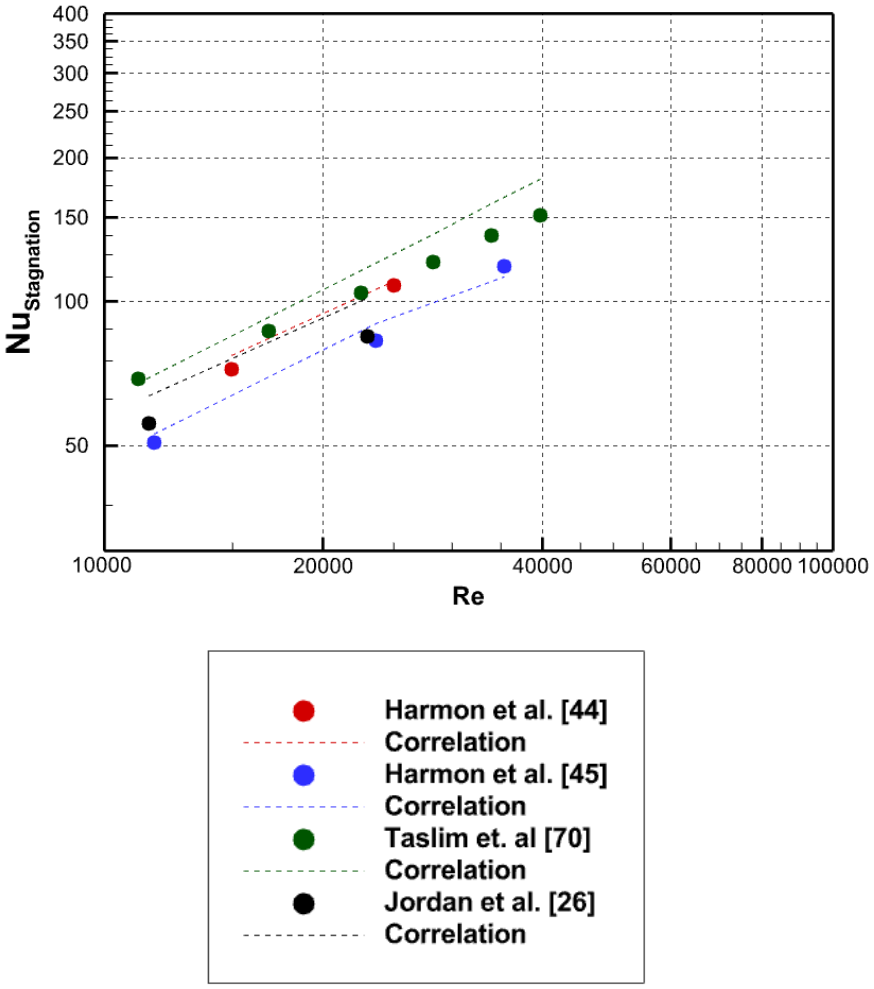

Figure 6.12: Comparison of heat transfer correlation estimates with published data

Similar comparisons are made for the discharge coefficient correlations. Due to very few studies of discharge coefficients, the study of Jordan et al. [26] was used for comparisons. Figure 6.13 presents the heat transfer results and correlations estimates for square edged, r/l = 0.18 and r/l = 0.5, racetrack jets. The correlation is able to predict with 5% deviation.

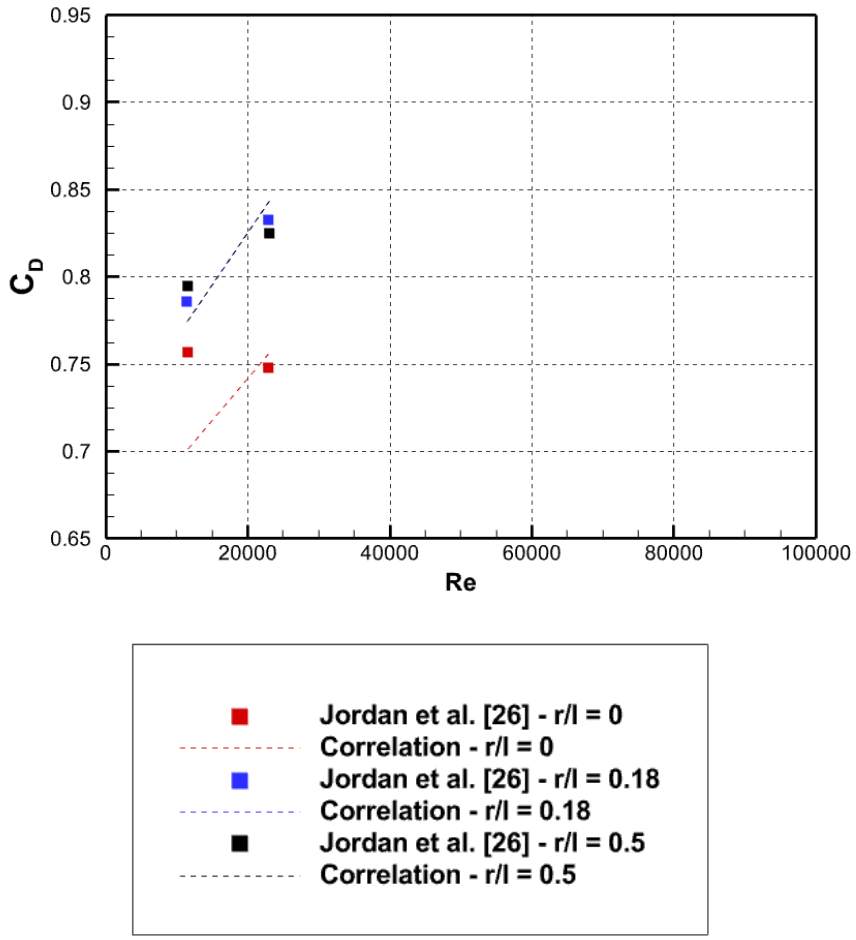

Figure 6.13: Comparison of correlation discharge coefficient estimates with Jordan et al. [26]

Summary

There were 95 experiments conducted to investigate the heat transfer and discharge coefficient trends. The characterization took place over the parameters: Reynolds number (Re), jet-to-jet spacing (s/d), jet-to-target surface spacing (z/d), jet nozzle length (jet plate thickness) (l/d), curvature-to-jet size (D/d) and fillet radius at the jet orifice (r/l). The results obtained agree with the previous literature and the correlation from Chupp et al. [23]. Confirming to the trend of [23], the Nusselt number is seen to be increasing with Reynolds number. The new correlations are able to predict with varying jet-to-jet spacing, jet nozzle length (jet plate thickness) and fillet radius ratio for different sets of jet-to-target surface spacing and curvature-to-jet size. Very few studies have developed correlations for pressure losses and the new correlations provide estimation capacity to predict the pressure losses for a given jet configuration. However, the pressure loss correlations are amongst the first impingement correlation to account the effect of jet configurations. The current heat transfer correlations are 90% confident to provide upto 10% deviation and pressure loss correlations are 93% confident to provide upto 10% deviation.

CHAPTER VII

CONCLUSIONS AND RECOMMENDATIONS

Conclusions

The investigation presented the heat transfer and discharge coefficient trends for leading edge jet impingement with racetrack shaped jets, for various jet configurations: shape, jet-to-jet spacing, jet-to-target surface spacing, jet nozzle length (jet plate thickness), curvature-to-jet size and flow conditions. For the heat transfer, a steady state technique was used to obtain regional Nusselt numbers. The current gas turbine cooling techniques employ various parameters to improve heat transfer performance and it is necessary to incorporate the parameters in the present model. The baseline case for this study, has been the square edged jet orifice, with jet nozzle length (jet plate thickness) of 1.33 diameters, jet-to-jet spacing of 8 diameters, jet-to-target surface spacing of 4 diameters and surface curvature of 5.33 diameters. Similarly, the discharge coefficients were calculated by measuring the pressure upstream and downstream of the jets for each of the 95 experiments.

As a general trend, it is established that racetrack jets outperform the round jets in terms of heat transfer. For the heat transfer, the increasing jet-to-jet spacing is seen to decrease the heat transfer, due to reduced mixing between the jets. It is also due to this reason, the discharge coefficients seem to improve with increasing jet-to-jet spacing. Lesser interactions would mean lesser flow resistance and fewer pressure losses. The effect of jet-to-target surface spacing is an interesting trend, with a inversely proportional nature with heat transfer. This came at the cost of severe penalties on the discharge coefficients. It is due to the quick transition of the impingement

jet to wall jet and closer spacing ensures their contact with the target plate and impingement surface, which further increases shear stress and flow resistance. Moreover, as larger diameter jets jets are used in the jet-to-target surface spacing of 2 diameters, more areas with peak Nusselt numbers can be seen and little variation in the circumferential direction. This was also at the cost of higher mass flow rates. For jet nozzle length (jet plate thickness), it seems that shorter jets have better heat transfer performance over the rest, but it also has the highest pressure drop. This is due to the vena contracta and jet constriction, which causes the pressure drop and increases jet turbulence. This problem of high-pressure loss is alleviated by increasing the jet nozzle length (jet plate thickness), however leading to a drop in Nusselt numbers and higher pressure losses at greater lengths. From the investigation, an intermediate length of 2.6 diameters is a tradeoff for better heat transfer and higher discharge coefficients. Finally the addition of fillets at the jet edge has always favored discharge coefficients and lowered the heat transfers.

Recommendations

The current research extended the research contributions of Jordan et al. [25-27] and Harmon et al. [44, 45] for heat transfer and discharge coefficients, by including the jet filleting, decreased jet-to-target surface spacing and jet nozzle length (jet plate thickness) in the correlations. One interesting idea is to have a rough target surface with pin-fins or rib turbulators. From the literature, they promise to provide enhanced heat transfer. In addition, there might be a possible upgrade from racetrack shaped jets to four lobed jets, by extending the areas of peak Nusselt numbers in the spanwise direction. This would help to improve area averaged Nusselt numbers. An experimental study for smaller ranges of Reynolds number would help shed some light on understanding heat transfer trends.

REFERENCES

1. Popiel, C.O. and O. Trass, *Visualization of a free and impinging round jet.* Experimental Thermal and Fluid Science, 1991. **4**(3): p. 253-264.

2. Han, B. and R.J. Goldstein, *Jet-Impingement Heat Transfer in Gas Turbine Systems.* Annals of the New York Academy of Sciences, 2006. **934**(1): p. 147-161.

3. Beltaos, N.R., *Impinging Circular Turbulent Jets.* Journal of the Hydraulics Division, 1974. **100**(10): p. 1313-1328.

4. Beltaos, S. and N. Rajaratnam, *IMPINGEMENT OF AXISYMMETRIC DEVELOPING JETS.* Journal of Hydraulic Research, 1977. **15**(4): p. 311-326.

5. Goldstein, R.J., A.S. Fleischer, and C. Cornaro, *A Visualization Study of Jet Impingement on Cylindrical Surfaces*, in *Applied Optical Measurements*. 1999, Springer Berlin Heidelberg. p. 307-317.

6. Geers, L.F.G., *Multiple impinging jet arrays. An experimental study on flow and heat transfer.* TU Delft, 2004.

7. Beitelmal, A.H., A.J. Shah, and M.A. Saad, *Analysis of an Impinging Two-Dimensional Jet.* Journal of Heat Transfer, 2005. **128**(3): p. 307-310.

8. Martin, H., *Heat and Mass Transfer between Impinging Gas Jets and Solid Surfaces*, in *Advances in Heat Transfer*, J.P. Hartnett and T.F. Irvine, Editors. 1977, Elsevier. p. 1-60.

9. Barata, J.M.M., *Ground Vortex Formation with Twin Impinging Jets.* SAE Transactions, 1996. **105**: p. 1221-1230.

10. Meier, N., *Civil Turbojet/Turbofan Specifications.* 2005.

11. Han, J.-C., *Gas Turbine Heat Transfer and Cooling Technology.* 2013: p. 887.

12. Perepezko, J.H., *The Hotter the Engine, the Better.* Science, 2009. **326**(5956): p. 1068-1069.

13. Han, J.-C. and A.P. Rallabandi, *TURBINE BLADE FILM COOLING USING PSP TECHNIQUE.* Frontiers in Heat and Mass Transfer, 2010. **1**(1).

14. Han, J.-C., *Recent Studies in Turbine Blade Cooling.* International Journal of Rotating Machinery, 2004. **10**(6): p. 443-457.

15. Ekkad, S.V. and P. Singh, *A Modern Review on Jet Impingement Heat Transfer Methods.* Journal of Heat Transfer, 2021. **143**(6).

16. Florschuetz, L.W., D.E. Metzger, and C.C. Su, *Heat Transfer Characteristics for Jet Array Impingement With Initial Crossflow.* Journal of Heat Transfer, 1984. **106**(1): p. 34-41.

17. Incropera, F.P., & DeWitt, D. P., *Fundamentals of heat and mass transfer*. 2002, New York: J. Wiley.

18. Brevet, P., et al., *Heat transfer to a row of impinging jets in consideration of optimization.* International Journal of Heat and Mass Transfer, 2002. **45**(20): p. 4191-4200.

19. Han, J.-C., S. Dutta, and S. Ekkad, *Gas Turbine Heat Transfer and Cooling Technology.* 2012.

20. Huang, Y., S.V. Ekkad, and J.-C. Han, *Detailed Heat Transfer Distributions Under an Array of Orthogonal Impinging Jets.* Journal of Thermophysics and Heat Transfer, 1998. **12**(1): p. 73-79.

21. Huang, L. and M.S. El-Genk, *Heat transfer of an impinging jet on a flat surface.* International Journal of Heat and Mass Transfer, 1994. **37**(13): p. 1915-1923.

22. Han, J.C.a.W., L. M., *Enhanced Internal Cooling of Turbine Blades and Vanes.* The Gas Turbine Handbook, DOE, Office of Fossil Energy, National Energy Technology Laboratory., 2006.

23. Chupp, R.E., et al., *Evaluation of internal heat-transfer coefficients for impingement-cooled turbine airfoils.* Journal of Aircraft, 1969. **6**(3): p. 203-208.

24. Metzger, D.E., T. Yamashita, and C.W. Jenkins, *Impingement Cooling of Concave Surfaces With Lines of Circular Air Jets.* Journal of Engineering for Power, 1969. **91**(3): p. 149-155.

25. Jordan, C.N., *Experimental investigation of leading edge jet impingement with varying jet geometries and inlet supply conditions for turbine cooling applications*, in *Mechanical Engineering*. 2012, Baylor University: 2012-08-08. p. 163.

26. Jordan, C.N., et al. *Leading Edge Impingement With Racetrack Shaped Jets and Varying Inlet Supply Conditions*. in *Volume 3A: Heat Transfer*. 2013. American Society of Mechanical Engineers.

27. Neil Jordan, C., L.M. Wright, and D.C. Crites, *Impingement Heat Transfer on a Cylindrical, Concave Surface With Varying Jet Geometries.* Journal of Heat Transfer, 2016. **138**(12): p. 122202.

28. Lee, D.H., Y.S. Chung, and D.S. Kim, *Turbulent flow and heat transfer measurements on a curved surface with a fully developed round impinging jet.* International Journal of Heat and Fluid Flow, 1997. **18**(1): p. 160-169.

29. Gori, F. and L. Bossi, *Optimal slot height in the jet cooling of a circular cylinder.* Applied Thermal Engineering, 2003. **23**(7): p. 859-870.

30. Bond, T., Wright, William B., *An Evaluation of Jet Impingement Heat Transfer Correlations for Piccolo Tube Application.* NASA, 2004.

31. Yu, J., et al., *Experimental investigation and correlation development of jet impingement heat transfer with two rows of aligned jet holes on an internal surface of a wing leading edge.* Chinese Journal of Aeronautics, 2018. **31**(10): p. 1962-1972.

32. Bu, X., et al., *Jet impingement heat transfer on a concave surface in a wing leading edge: Experimental study and correlation development.* Experimental Thermal and Fluid Science, 2016. **78**: p. 199-207.

33. Kanokjaruvijit, K. and R.F. Martinez-Botas, *Heat transfer correlations of perpendicularly impinging jets on a hemispherical-dimpled surface.* International Journal of Heat and Mass Transfer, 2010. **53**(15): p. 3045-3056.

34. Hrycak, P., *Heat transfer from a row of impinging jets to concave cylindrical surfaces.* International Journal of Heat and Mass Transfer, 1981. **24**(3): p. 407-419.

35. Chang, H., J. Zhang, and T. Huang. *Experimental Investigation on Impingement Heat Transfer From Rib Roughened Surface Within Arrays of Circular Jets: Correlation*. in *Volume 3: Heat Transfer; Electric Power; Industrial and Cogeneration*. 2000. American Society of Mechanical Engineers.

36. Fénot, M., J.-J. Vullierme, and E. Dorignac, *A heat transfer measurement of jet impingement with high injection temperature.* Comptes Rendus Mécanique, 2005. **333**(10): p. 778-782.

37. Forster, M. and B. Weigand, *Experimental and numerical investigation of jet impingement cooling onto a concave leading edge of a generic gas turbine blade.* International Journal of Thermal Sciences, 2021. **164**: p. 106862.

38. Tabakoff, W. and W. Clevenger, *Gas Turbine Blade Heat Transfer Augmentation by Impingement of Air Jets Having Various Configurations.* Journal of Engineering for Power, 1972. **94**(1): p. 51-58.

39. Martin, E.L., L.M. Wright, and D.C. Crites, *Impingement Heat Transfer Enhancement on a Cylindrical, Leading Edge Model With Varying Jet Temperatures.* Journal of Turbomachinery, 2013. **135**(3).

40. Facchini, B., et al. *Experimental Investigation on the Heat Transfer of a Leading Edge Cooling System: Effects of Jet-to-Jet Spacing and Showerhead Extraction*. in *Volume 3A: Heat Transfer*. 2013. American Society of Mechanical Engineers.

41. Bunker, R.S. and D.E. Metzger, *Local Heat Transfer in Internally Cooled Turbine Airfoil Leading Edge Regions: Part I—Impingement Cooling Without Film Coolant Extraction.* Journal of Turbomachinery, 1990. **112**(3): p. 451-458.

42. Martin, E.L., L.M. Wright, and D.C. Crites. *Computational Investigation of Jet Impingement on Turbine Blade Leading Edge Cooling With Engine-Like Temperatures*. in *Volume 4: Heat Transfer, Parts A and B*. 2012. American Society of Mechanical Engineers.

43. Patil, V.S. and R.P. Vedula, *Local heat transfer for jet impingement onto a concave surface including injection nozzle length to diameter and curvature ratio effects.* Experimental Thermal and Fluid Science, 2018. **92**: p. 375-389.

44. Harmon, W.V., C.A. Elston, and L.M. Wright. *Experimental Investigation of Leading Edge Impingement Under High Rotation Numbers With Racetrack Shaped Jets*. in *Volume 5A: Heat Transfer*. 2014. American Society of Mechanical Engineers.

45. Harmon, W.V., et al. *Combined Effects of Jet Plate Thickness and Fillet Radius on Leading Edge Jet Impingement With Round and Racetrack Shaped Jets*. in *Volume 5A: Heat Transfer*. 2015. American Society of Mechanical Engineers.

46. Gau, C. and C.M. Chung, *Surface Curvature Effect on Slot-Air-Jet Impingement Cooling Flow and Heat Transfer Process.* Journal of Heat Transfer, 1991. **113**(4): p. 858-864.

47. Yang, G., M. Choi, and J.S. Lee, *An experimental study of slot jet impingement cooling on concave surface: effects of nozzle configuration and curvature.* International Journal of Heat and Mass Transfer, 1999. **42**(12): p. 2199-2209.

48. Choi, M., et al., *Measurements of impinging jet flow and heat transfer on a semi-circular concave surface.* International Journal of Heat and Mass Transfer, 2000. **43**(10): p. 1811-1822.

49. Colucci, D.W. and R. Viskanta, *Effect of nozzle geometry on local convective heat transfer to a confined impinging air jet.* Experimental Thermal and Fluid Science, 1996. **13**(1): p. 71-80.

50. Guan, T., J.-z. Zhang, and Y. Shan, *Convective heat transfer by a row of tab-excited impinging jets on a wedge-shaped concave surface.* International Journal of Thermal Sciences, 2016. **100**: p. 37-53.

51. Guan, T., et al., *Conjugate heat transfer on leading edge of a conical wall subjected to external cold flow and internal hot jet impingement from chevron nozzle – Part 1: Experimental analysis.* International Journal of Heat and Mass Transfer, 2017. **106**: p. 329-338.

52. Lee, J. and S.-J. Lee, *The effect of nozzle aspect ratio on stagnation region heat transfer characteristics of elliptic impinging jet.* International Journal of Heat and Mass Transfer, 2000. **43**(4): p. 555-575.

53. Singh, P. and S. Ekkad. *Effects of Rotation on Heat Transfer due to Jet Impingement on Cylindrical Dimpled Target Surface*. in *Volume 5B: Heat Transfer*. 2016. American Society of Mechanical Engineers.

54. Taslim, M.E. and D. Bethka, *Experimental and Numerical Impingement Heat Transfer in an Airfoil Leading-Edge Cooling Channel With Cross-Flow.* Journal of Turbomachinery, 2009. **131**(1): p. 011021.

55. Taslim, M.E., Y. Pan, and K. Bakhtari. *Experimental Racetrack Shaped Jet Impingement on a Roughened Leading-Edge Wall With Film Holes*. in *Volume 3: Turbo Expo 2002, Parts A and B*. 2002. ASMEDC.

56. Taslim, M.E. and L. Setayeshgar. *Experimental Leading-Edge Impingement Cooling Through Racetrack Crossover Holes*. in *Volume 3: Heat Transfer; Electric Power; Industrial and Cogeneration*. 2001. American Society of Mechanical Engineers.

57. Jungho Lee, S.-J.L., *The effect of nozzle configuration on stagnation region heat transfer enhancement of axisymmetric jet impingement.* International Journal of Heat and Mass Transfer, 1999. **43**.

58. Brignoni, L.A. and S.V. Garimella, *Effects of nozzle-inlet chamfering on pressure drop and heat transfer in confined air jet impingement.* International Journal of Heat and Mass Transfer, 2000. **43**(7): p. 1133-1139.

59. Hay, N. and A. Spencer, *Discharge Coefficients of Cooling Holes With Radiused and Chamfered Inlets.* Journal of Turbomachinery, 1992. **114**(4): p. 701-706.

60. Dittmann, M., K. Dullenkopf , and S. Wittig, *Discharge Coefficients of Rotating Short Orifices With Radiused and Chamfered Inlets.* Journal of Engineering for Gas Turbines and Power, 2004. **126**(4): p. 803-808.

61. Florschuetz, L.W., D.E. Metzger, and C.R. Truman, *Jet array impingement with crossflow-correlation of streamwise resolved flow and heat transfer distributions*. 1981.

62. Callaghan, E.E.B., Dean T., *Investigation of Flow Coefficient of Circular, Square, and Elliptical Orifices at High Pressure Ratios*. September 1949.

63. Taslim, M.E. and N. Rosso. *Experimental/Numerical Study of Multiple Rows of Confined Jet Impingement Normal to a Surface at Close Distances*. in *ASME Turbo Expo 2012: Turbine Technical Conference and Exposition*. 2012.

64. Lee, J., et al., *Effects of Jet-To-Target Plate Distance and Reynolds Number on Jet Array Impingement Heat Transfer.* Journal of Turbomachinery, 2014. **136**(5): p. 051013.

65. Chen, L., et al., *Detailed heat transfer investigation of an impingement jet array with large jet-to-jet distance.* International Journal of Thermal Sciences, 2019. **146**.

66. Leary, W.A., Tsai, D.H.,, *Metering of Gases by Means of the ASME Square-Edged Orifice With Flange Taps.* Sloan Laboratory for the Automotive and Aircraft Engines, Massachusetts Institute of Technology, 1951.

67. Han, J.-C. and L.M. Wright, *Experimental Methods in Heat Transfer and Fluid Mechanics.* 2020.

68. Chowdhury, N.H.K., H. Zirakzadeh, and J.-C. Han, *A Predictive Model for Preliminary Gas Turbine Blade Cooling Analysis.* Journal of Turbomachinery, 2017. **139**(9).

69. S.J.Kline, F.A.M., *Describing Uncertainties in Single-Sample Experiments.* 1953. **75**.

70. Taslim, M.E., K. Bakhtari, and H. Liu, *Experimental and Numerical Investigation of Impingement on a Rib-Roughened Leading-Edge Wall.* Journal of Turbomachinery, 2003. **125**(4): p. 682-691.

APPENDIX A

CORRELATION DEVELOPMENT PROCESS

This section discusses the development of correlations for stagnation Nusselt number and discharge coefficients. The progression for heat transfer correlation would be discussed in detail and similar strategy is applied for obtaining discharge coefficients. From the previous sections, it is clear that the Nusselt number varies with a power equation of Reynolds number, as in equation A1.1:

$$Nu_{stagnation} = A \cdot Re_{jet}^{m} \quad \textbf{(A1.1)}$$

While the general form of heat transfer equation is true, accurate results are obtained based on the leading coefficient (A) and exponent (m). Different combinations of A and m provide different trendlines. From the comprehensive plot in figure 5.22, there is a huge spread in Nusselt numbers due to various geometric configurations. Different set of parametric values provide different equations, very similar to varying values of A and m. This implies that A and m are linked to the geometric parameters and incorporating them would help improve heat transfer estimations. Hence, it is essential to explore the dependence of A and m on each of the geometrical parameters: - jet-to-jet spacing (s/d), jet-to-target surface spacing (z/d), surface curvature (D/d), jet nozzle length (jet plate thickness) (l/d) and fillet radius (r/l). The approach is to obtain the nature of trend equations for every parameter. It is important to note that the coefficients of individual trends are not important as they would be based on a smaller set of data. Each of these trends indicate proportional relationship with stagnation Nusselt number. Putting all the trend equations, we obtain a skeleton correlation with unknown coefficients. These coefficients are calculated by

carrying out nonlinear regression fit. The following provides a step-by-step approach to obtain trend equations of A and m for jet-to-jet spacing, which can be further extended to other parameters as well:

1. Take a baseline case for heat transfer data. For example, the configuration with jet-to-jet spacing of 8, jet-to-target surface spacing of 4, jet nozzle length (jet plate thickness) of 1.33 diameters, fillet radius of 0 and surface curvature of 5.33 diameters.
2. Vary only the jet-to-jet spacing by keeping all other values constant. For this example, the s/d values are 2,4 and 8 and all other parametric values constant (z/d = 4, l/d = 1.33, r/l = 0 and D/d = 5.33)
3. Obtain the curve fit equations for the three sets of data, that is, for s/d = 2, 4 and 8. The equations would be similar to equation A1.1, with different values of A and m. Figure A1.1 illustrates the curve fit equations for the three sets. These values are different due to varying s/d only. Thus, the derivation of trend equation would only present dependence on s/d.

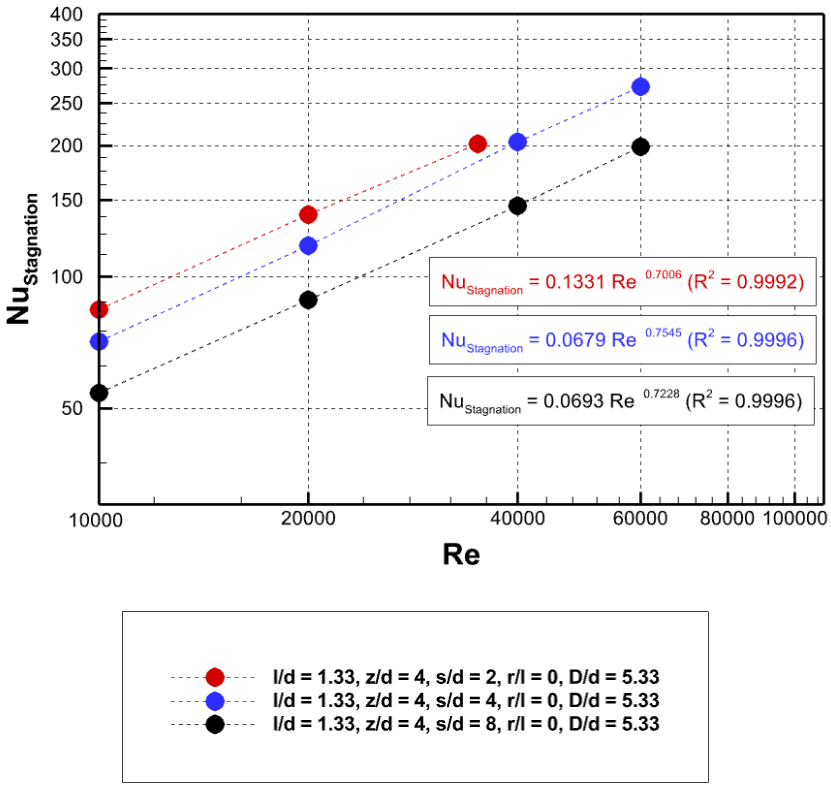

Figure A1.1: Curve fit equations for stagnation Nusselt number with varying jet-to-jet spacing

$$A = f\left(\frac{s}{d}\right) \; and \; m = f\left(\frac{s}{d}\right) \qquad \textbf{(A1.2)}$$

4. Plot A vs s/d and m vs s/d and obtain curve fit equations. These equations indicate the variation in leading coefficient and exponent with s/d. Figure A1.2 and A1.3 illustrate these equations for A and m respectively. Let these equations be A1.2 and A1.3.

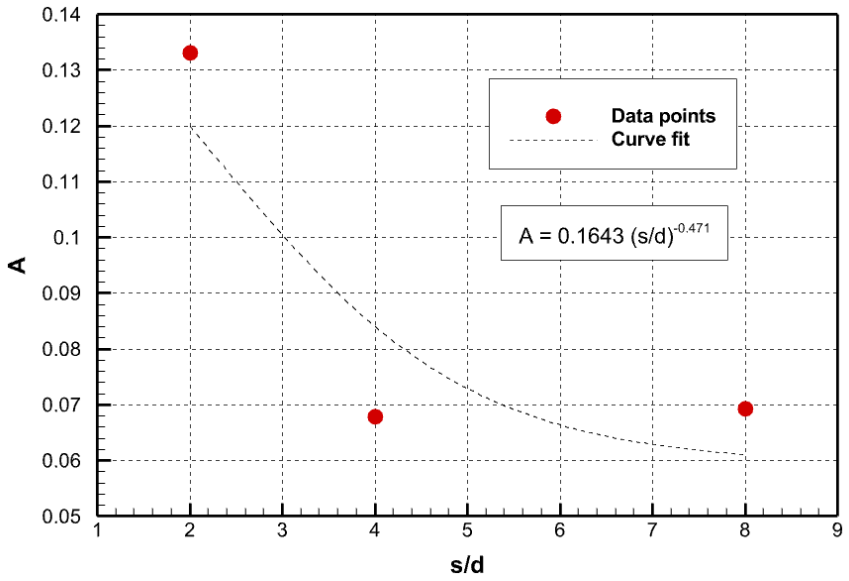

Figure A1.2: Variation plot of A with s/d

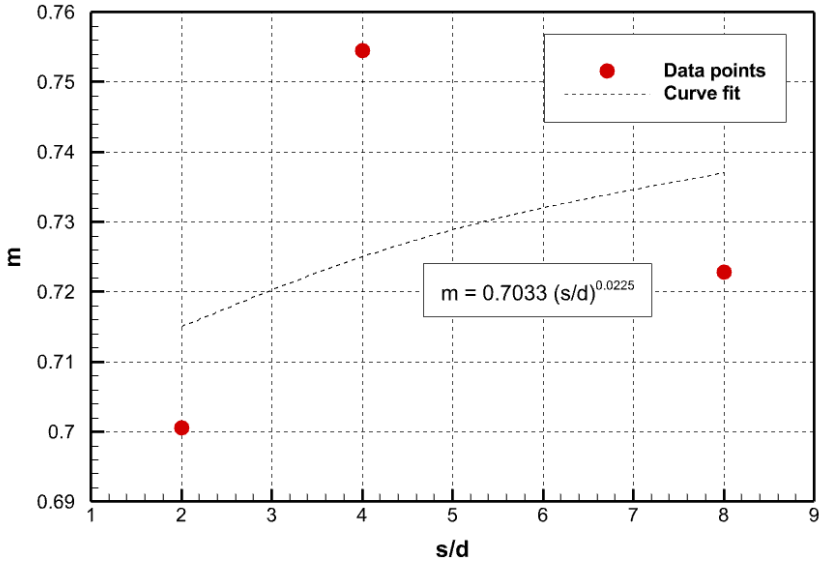

Figure A1.3: Variation plot of m with s/d

$$A = 0.1643 * \left(\frac{s}{d}\right)^{-0.471} \quad \textbf{(A1.2)}$$

$$m = 0.7033 * \left(\frac{s}{d}\right)^{0.0225} \quad \textbf{(A1.3)}$$

5. Put the equations A1.2 and A1.3 in A1.1 to obtain the trend equations for varying s/d, equation A1.4. This equation can now estimate the heat transfer values for varying s/d within 2 to 8, keeping all other parameters constant, that is, z/d = 4, l/d = 1.33, r/l = 0 and D/d = 5.33. As mentioned, the takeaway of this method is the nature of trend equations. This trend equation is tested to check the accuracy of the results and they provide maximum of 8% deviation. Figure A1.4 provides the spread of results.

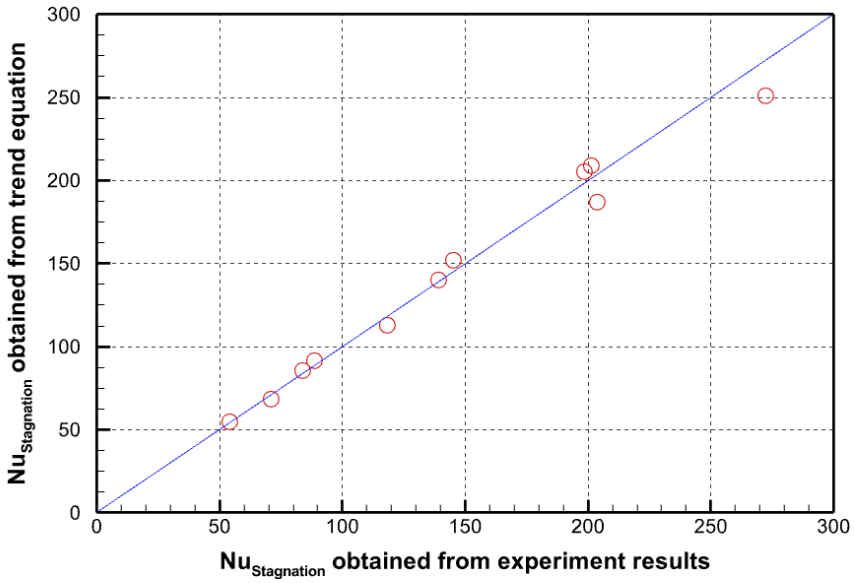

Figure A1.4: Comparison plot between trend equation estimation and experiment results

$$Nu = 0.1643 * \left(\frac{S}{d}\right)^{-0.471} * Re^{0.7033*\left(\frac{S}{d}\right)^{0.0225}} \quad \textbf{(A1.4)}$$

Similar process is carried out to obtain the trend equations of other parameters. These equations are presented as equations A1.4a, A1.5, A1.6, A1.7 and A1.8.

$$Nu = a_1 * \left(\frac{S}{d}\right)^{a_2} * Re^{a_3*\left(\frac{S}{d}\right)^{a_4}} \quad \textbf{(A1.4a)}$$

$$Nu = a_5 * \left(\frac{z}{d}\right)^{a_6} * Re^{a_7 * \left(\frac{z}{d}\right)^{a_8}} \quad \textbf{(A1.5)}$$

$$Nu = a_9 * \left(\frac{D}{d}\right)^{a_{10}} * Re^{a_{11} * \left(\frac{D}{d}\right)^{a_{12}}} \quad \textbf{(A1.6)}$$

$$Nu = a_{13} * \left(\frac{l}{d}\right)^{a_{14}} * Re^{a_{15} * \left(\frac{l}{d}\right)^{a_{16}}} \quad \textbf{(A1.7)}$$

$$Nu = a_{17} * e^{(a_{18} * \frac{r}{l})} * Re^{a_{19} * e^{(a_{20} * \frac{r}{l})}} \quad \textbf{(A1.8)}$$

It is becoming clear that the leading coefficient and exponent are dependent on geometric parameters as:

$$A = f\left(\frac{s}{d}, \frac{z}{d}, \frac{l}{d}, \frac{r}{l}, \frac{D}{d}\right) \text{ and } m = f\left(\frac{s}{d}, \frac{z}{d}, \frac{l}{d}, \frac{r}{l}, \frac{D}{d}\right) \quad \textbf{(A1.9)}$$

Each of the trend demonstrates the proportional relationship of trend equations with Nusselt number. Combining all the trend equations, the skeleton of heat transfer correlation is obtained as the coefficients are yet unknown, as in equation A1.10. Nonlinear regression fit is carried out over the 95 experimental data to obtain the coefficients. A MATLAB Code is presented at the end of this section which illustrates the process. From these steps, the final correlations are obtained for stagnation Nusselt number.

$$Nu = a_1 \left(\frac{s}{d}\right)^{a_2} \left(\frac{l}{d}\right)^{a_3} \left(\frac{z}{d}\right)^{a_4} \left(\frac{D}{d}\right)^{a_5} \left(e^{a_6 * \frac{r}{l}}\right) Re^{\left[a_7 \left(\frac{s}{d}\right)^{a_8} \left(\frac{l}{d}\right)^{a_9} \left(\frac{z}{d}\right)^{a_{10}} \left(\frac{D}{d}\right)^{a_{11}} \left(e^{a_{12} * \frac{r}{l}}\right)\right]} \quad \textbf{(A1.10)}$$

Similar process is performed for obtaining discharge coefficients. Parametric trend equations are obtained and combined to provide a skeleton structure as in equation A1.11.

Nonlinear regression fit is carried out to obtain the coefficient values and obtain the final correlations for discharge coefficients.

$$C_D = a_1 \left(\frac{S}{d}\right)^{a_2} \left(\frac{l}{d}\right)^{a_3} \left(\frac{Z}{d}\right)^{a_4} \left(\frac{D}{d}\right)^{a_5} \left(e^{a_6 * \frac{r}{l}}\right) Re^{\left[a_7 \left(\frac{S}{d}\right)^{a_8} \left(\frac{l}{d}\right)^{a_9} \left(\frac{Z}{d}\right)^{a_{10}} \left(\frac{D}{d}\right)^{a_{11}} \left(e^{a_{12} * \frac{r}{l}}\right)\right]} \quad \textbf{(A1.11)}$$

Following is the MATLAB code used for carrying out the nonlinear regression fit.

```
%%%%%%%%%%%%%%%%%%%%%%%%%%%%%%%%%%%%%%%%%%%%%%%%%%%%%%%%%%%%%%%%%%%%%%%%%%%%%%%%
%
%  Nonlinear regression fit to estimate correlation coefficients
%
%  By: Ritwik Kulkarni
%
%  Description: This code carries out nonlinear regression using nlinfit
%               function. An xls file (Excel 97-2003 worksheet is uploaded
%               that contains parametric columns in the order:
%               Reynolds number, s/d, l/d, r/l, z/d, D/d, Nu and Cd.
%               Based on the nature of skeleton equation, the total number
%               of coefficients are provided as random inputs. The function
%               outputs the coefficients.
%
%   Warning: Running this code can sometimes result in errors like "NaN" or
%            "Inf input values". This is due to randomness in coefficients.
%            It is advisable to re-run the code a few more times to obtain
%            the right results.
%
%%%%%%%%%%%%%%%%%%%%%%%%%%%%%%%%%%%%%%%%%%%%%%%%%%%%%%%%%%%%%%%%%%%%%%%%%%%%%%%%

clear all
clc

% Extracting the input table from xls file

T = readtable('zd4_fixed.xls');

% Conversion of table elements to arrays

Re = table2array(T(:,1)); sd = table2array(T(:,2));
ld = table2array(T(:,3)); rl = table2array(T(:,4));
zd = table2array(T(:,5)); Dd = table2array(T(:,6));
Nu = table2array(T(:,7)); Cd = table2array(T(:,8));
rl = rl;
y  = Nu;                          % Dependent variable vector
xm = [sd(:) ld(:) rl(:) Re(:)];       % Independent variable vector

% Skeleton Correlation Equation
% Here x(:,1) refers to elements of s/d, x(:,2) refers to elements of l/d
% and is further extended to variables in variable xm.
% Coefficients are stored as array, that is, variable "b".

yfcn = @(b,x)
b(1).*(x(:,1).^(b(2))).*(x(:,2).^(b(3))).*(exp(b(4).*x(:,3))).*(x(:,4)).^(b(5).*(x(:,1).^(b(6))).*(x(:,2).^(b(7))).*(exp(b(8).*x(:,3))))

% Assigning random values to coefficients

b0 = rand(8,1);

% Running the nlinfit function

beta = nlinfit(xm,y(:),yfcn,b0)

% beta provides the final set of coefficients after regression.
```

APPENDIX B

LABVIEW FILES FOR DATA ACQUISTION

1. ImpingingJets.vi: This file is used for obtaining temperatures across 128 thermocouples. However, this file served the purpose of collecting the data once steady state was reached. For instantaneous storage, the next file called “SteadyState.vi” was used.

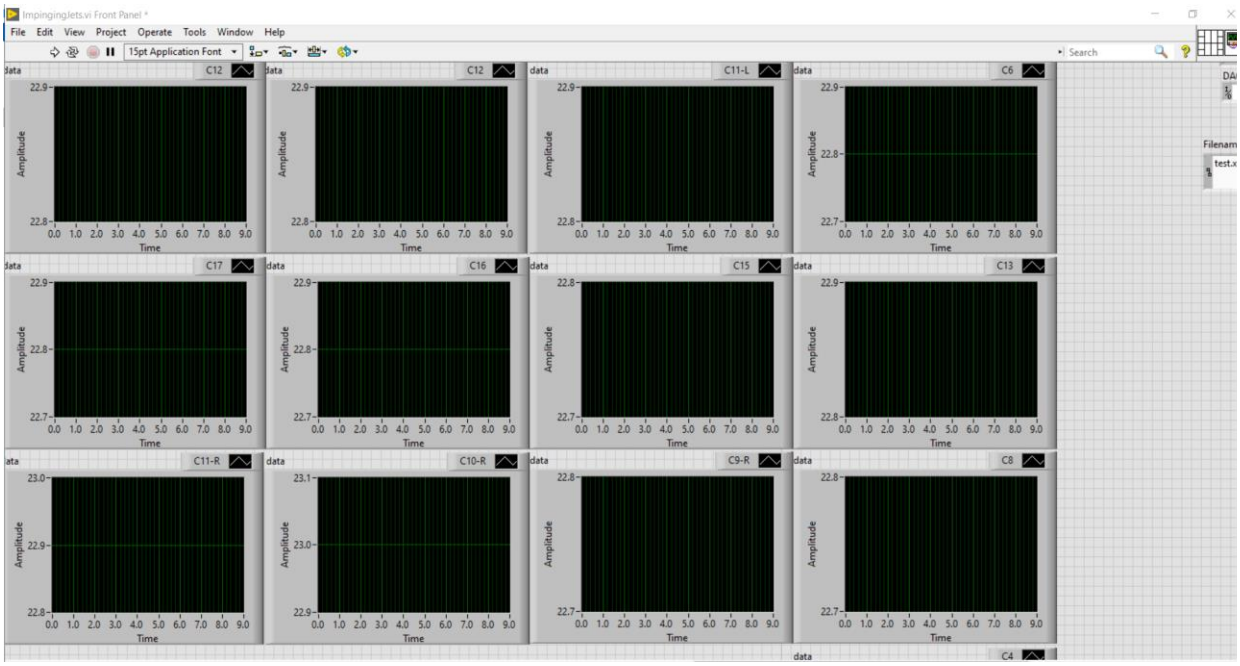

Figure A2.1: View of ImpingingJets.vi file

2. SteadyState.vi: This file was used to obtain temperatures across __ thermocouples, positioned at stagnation line and extremities every 5 seconds. Compilation of all these files provided temperature-time variation plots and checked for steady state condition.

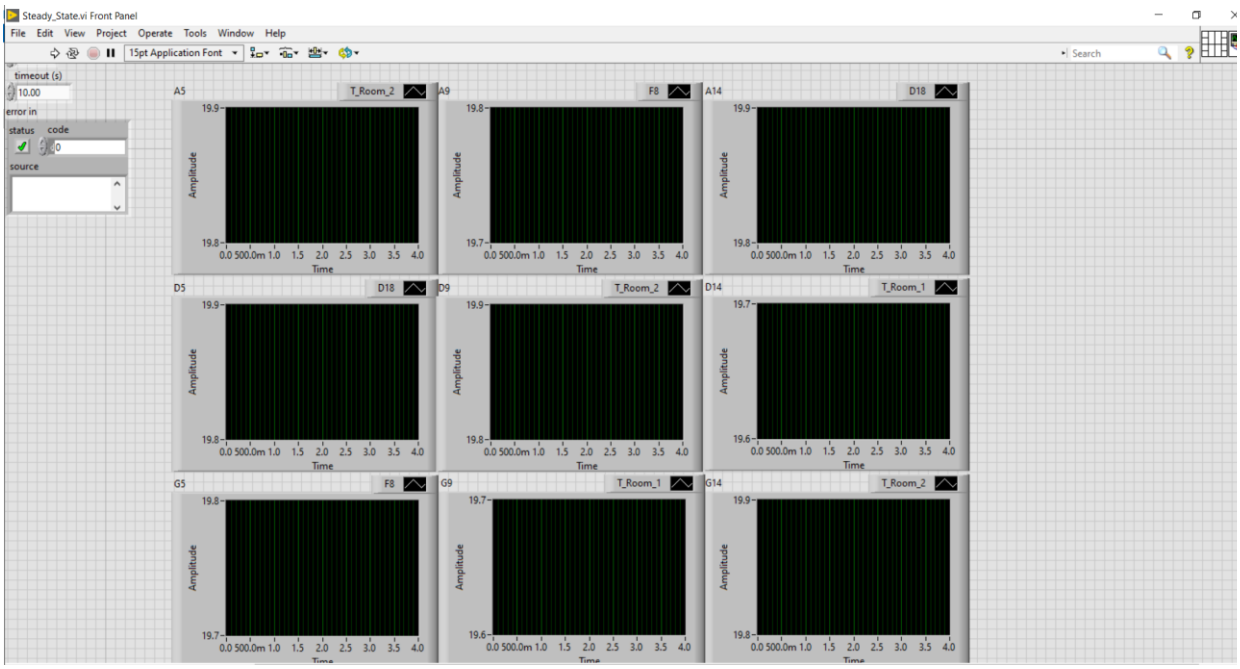

Figure A2.2: View of SteadyState.vi file